Planar Rayleigh Scattering Measurements of Shock Enhanced Mixing

Thesis by

John M. Budzinski

In Partial Fulfillment of the Requirements
for the Degree of

Doctor of Philosophy

California Institute of Technology
Pasadena, California
1992

(Defended May 8, 1992)

ACKNOWLEDGMENTS

I would like to thank my advisor Professor Edward Zukoski for his support, encouragement, and advice. I am grateful for all the help and many contributions in the first few years of the project of Dr. Jeff Jacobs. I would like to thank my committee: Professors Hans Hornung, Frank Marble, Anatol Roshko, and Bradford Sturtevant.

I would like to express my gratitude to my friends and fellow students especially Derek Lisoski. I would like to thank Dorthy Eckerman, and the Aero shop especially George Lundgren and Phil Wood.

I am very grateful for all the support and encouragement I have received from my fiancée Teresa, my parents, my sisters Nancy and Barbara, and my brother Michael.

This work was supported by the URI AFOSR-90-0188.

ABSTRACT

This investigation was concerned with the mixing which occurs after the unsteady interaction of a shock wave with a laminar jet of helium. The jet of helium was injected normal to the direction of the propagation of the shock. The vorticity created at the boundaries of the jet during the shock interaction generates a stream of air which divides the initial circular cross section of the jet into two lobes. Each lobe is further divided into a tail region and a vortex core. The vortex cores from each lobe form a vortex pair that pulls ahead of the tail regions. In the present investigation the primary diagnostic, planar Rayleigh scattering, had sufficient spatial and temporal resolution to resolve the smallest diffusion scales present and allowed helium mole fractions to be measured in two-dimensional planes normal to the original jet flow direction. The amount of molecular mixing was evaluated with a mass distribution function at increasing times after the shock interaction. The total masses of helium contained in regions where the molar concentration of helium was at least 30% and 50% were also calculated. The shock Mach number was varied, and the effect of a reflected shock was studied. The velocity and spacing of the vortex pairs was measured. It was found that shock interactions can significantly increase the mixing between the air and helium. As the Mach number increases, better mixing occurs as the stream of air divides the jet. However, less mixing occurs at the later times when the vortex pairs are moving ahead of the tails. A rough collapse of the mixing data occurs when time is normalized with the change in velocity of the air behind the shock. The measured velocities and estimated values of the circulation agree very well with previous computational results. An increase in the enhancement of mixing occurred after the interaction with the reflected shock.

TABLE OF CONTENTS

NOMENCLATURE

$()_0$	pertaining to the initial conditions, before the shock interaction
$()_1$	pertaining to the conditions before the shock interaction
$()_2$	pertaining to the conditions after the shock interaction
$()_{air}$	pertaining to pure air
$()_{cmf}$	pertaining to the center of mass fraction
$()_{He}$	pertaining to pure helium
$()_l$	pertaining to the light gas
$()_v$	pertaining to the vortex pair
α	molecular scattering cross section.
a	the speed of sound
A	area
χ	mole fraction
d	diameter of the jet cross section based on the region of 50% jet fluid
D	jet exit diameter
$\mathscr{D}$	diffusion coefficient
ε	strain rate
f	mass fraction
γ	specific heat ratio
Γ	circulation
h	height above the jet exit
m	mass distribution function
M	shock Mach number
M_{tot}	total mass of helium
n	number density of molecules
p	pressure
ρ	density

r_0	initial jet cross section radius based on the region of 50% jet fluid
t	time
τ	characteristic time scale
u	velocity of the air behind the shock
U_v	velocity of the vortex pair relative to the surrounding air
U_{cmf}	velocity of the centers of mass fraction relative to the surrounding air
ω	vorticity
x	x coordinate
y	y coordinate
y_v	vertical spacing based on the centers of the vortex cores
y_{cmf}	vertical spacing based on the centers of mass fraction

CHAPTER 1

INTRODUCTION

1.1. Motivation

It is generally understood that a vehicle using an air breathing engine while traveling at hypersonic speeds will require the air passing through the engine to remain supersonic relative to the airframe, while mixing and combustion occur with the fuel. The time available for mixing between the air and hydrogen fuel is greatly reduced compared to a more conventional subsonic engine. For example, a typical vehicle traveling at Mach 15, may have the air in the combuster at Mach 5 with a velocity of 4000 m/s. Given the fact that the combustion chamber can only be a few meters long, the air will only be in the engine for 1-2 milliseconds. A sample calculation is given in Appendix A.

Additional concern over the mixing is caused by the fact that the shear layers which form between the fuel and air will most likely be compressible, and compressible shear layers have growth rates much smaller than incompressible shear layers (Papamoschou and Roshko 1988, Hall 1991). The mixing due to the shear of the flow will be less than that for more conventional subsonic engines.

These realities facing the designers of supersonic combustion engines generate the need for mechanisms to augment the mixing process.

1.2. Background.

Such a mechanism, proposed by Marble, et al. (1987), uses weak shock waves inside the engine to enhance the mixing between the fuel and air. The concept is envisioned as a three-dimensional steady interaction between a jet of hydrogen and an

oblique shock wave. The enhancement in mixing is driven by the baroclinic term in the vorticity equation:

$$\rho \frac{d}{dt}\left(\frac{\omega}{\rho}\right) = \frac{1}{\rho^2}\nabla\rho \times \nabla p \quad .$$

The pressure gradient of the shock wave interacts with the density gradients between the air and hydrogen fuel to generate vorticity, which increases strain rates and enhances the rate of molecular scale mixing due to diffusion. This interaction is an example of the shock-induced Rayleigh-Taylor instability, or Richtmyer-Meshkov instability. Experimental and computational studies of injectors based on the shock-jet interaction were carried out by Waitz, et al. (1991, 1992), and computational studies including combustion were performed by Drummond, et al. (1991).

Analogies have been made between the three-dimensional steady shock-jet interaction and the two-dimensional unsteady interaction of a shock wave passing over a a cylindrical volume of lower density fluid (Marble et al. 1987, 1990, and Yang 1991). This analogy is shown in Figure 1-1; in a Lagrangian sense, the cross sections of the jet essentially undergo the same interaction in each case.

One of the earliest studies on the unsteady interaction of a shock with a cylindrical region of lower density fluid was performed by Rudinger and Somers (1960) in which the cylindrical volumes were created with jets of different density gases injected normal to the shock propagation direction. The purpose of this study was to illustrate that tracer bubbles of different density gases used for flow visualization or velocity measurements will not exactly move with the surrounding flow if they undergo accelerations.

Haas (1984) and Haas and Sturtevant (1987) studied the interaction of weak shocks with cylindrical volumes confined by microfilm membranes to model how finite-amplitude waves in random media generate turbulence. These experiments examined the wave patterns that developed and showed the deformation of the initial cylindrical

volume. It was the results of the experiments of Haas and Sturtevant that motivated Marble et al (1987) to suggest that shock waves be used to enhance the mixing in supersonic combustion engines. Computations modeling the experiments of Haas and Sturtevant were performed by Picone and Boris (1987) and by Marble, et al (1987).

At the beginning of the current experimental program, a study of shock interactions with laminar jets of helium was performed by Jacobs (1992), who viewed the jet after the shock interaction with the planar laser induced fluorescence of a tracer dye, biacetyl (2,3-Butanedione), which was premixed with the helium. Finally, the most comprehensive computations of the unsteady interaction were performed by Yang (1991).

These investigations have developed a fundamental understanding of the general flow characteristics and have shown that the vorticity generated at the boundaries of the cylindrical volume during the shock interaction causes a stream of air to divide the initial circular cross section into two lobes. Each lobe is further divided into a tail region and a vortex core. The vortex cores from each lobe form a vortex pair that pulls ahead of the tail regions. The effect of the overall flow development is to generate straining motions which increase the area of the air-helium interface and enhance the mixing.

Furthermore, the previous investigations have modeled how the circulation deposited by the shock scales with the shock strength and density ratio. By matching the kinetic energy and impulse for a vortex pair to the kinetic energy and impulse of an impulsively started lamina (which modeled the impulsively started helium), Rudinger and Somers (1960) derived for weak shock waves the expression:

$$\Gamma = 2ur_0 \left(\frac{1 - \frac{\rho_l}{\rho_h}}{1 + \frac{\rho_l}{\rho_h}} \right) .$$

Here Γ is the circulation, u is the change in velocity of the surrounding (heavy) gas across the shock found from the normal shock relations for a perfect gas, r_0 is the initial radius, and ρ_l/ρ_h is the ratio of light gas density to heavy gas density. Marble, et al. (1990) used a one-dimensional accoustic arguement to estimate for weak waves that the circulation should scale as:

$$\Gamma \sim 2ur_0M\frac{\sqrt{\frac{\gamma_h\rho_h}{\gamma_l\rho_l}}-1}{\sqrt{\frac{\gamma_h\rho_h}{\gamma_l\rho_l}}+1} \ .$$

Picone et al (1985) analytically integrated the vorticity equation for the case of a shock passing through a circular cross-section and found that:

$$\Gamma \approx 2u\left(1-\frac{u}{2a_1M}\right)r_0 \ln\left(\frac{\rho_h}{\rho_l}\right) \ .$$

This expression was the first to predict that as the shock Mach number increases the circulation, normalized by the change in velocity across the shock and the initial radius, decreases.

Furthermore, Hendricks and Marble (1990) used simple one-dimensional gasdynamic relations to developed a set of nonlinear, coupled equations which allowed the circulation to be found for various Mach numbers and density ratios. Also, Yang (1991) used a similarity argument based on the vorticity equation to predict for general Mach numbers (not just weak waves) that:

$$\Gamma = 4r_0u\frac{\rho_1}{\rho_2}\left(\frac{1-\frac{\rho_l}{\rho_h}}{1+\frac{\rho_l}{\rho_h}}\right) \ .$$

Here ρ_1 is the density of the surrounding gas before the shock interaction, and ρ_2 is the density of the surrounding gas after the shock interaction. The main difference in the scaling of the circulation for general Mach numbers developed by Yang, and that developed by Rudinger and Somers for the limit of weak waves is the extra term ρ_1/ρ_2 which takes into account the compression of the lateral scales by the shock wave.

Yang also performed computational experiments for various Mach numbers and density ratios and calculated the circulation generated. He compared the computed circulation to his circulation model and to the models of Rudinger and Somers (1960), Picone and Boris (1987), and Hendricks and Marble (1990). Figure 1-2 (reproduced from Yang 1991) compares the ratio of predicted to computed circulation for the various models as a function of shock Mach number for a density ratio of 0.138 (pure helium/pure air). Assuming the computations are correct, Yang's model is the most accurate in predicting the circulation as a function of Mach number. He also found that his model is better than the other models at predicting the circulation for a fixed Mach number and varying density ratio as shown in Figure 1-3.

More important than whether a models predicts the exact circulation is whether a model predicts how the circulation scales with the Mach number. Table 1-1 shows the ratio of circulation generated by a Mach 1.05 shock to the circulation generated by stronger shocks for the computations and for the different models.

Table 1-1.

	$\Gamma/\Gamma_{1.05}$	$\Gamma/\Gamma_{1.05}$ for the models			
Mach #	Computations	Yang	P&B	H&M	R&S
1.1	1.88	1.81	1.88	1.92	2.0
1.2	3.00	3.03	3.41	3.57	4.27
1.5	4.04	4.96	6.81	7.42	11.84
2.0	5.00	6.23	11.0	12.0	21.3

The table illustrates that the different models agree well with each other and with the computations for low shock Mach numbers. For the higher Mach numbers the scaling based on Yang's model is much better than the other models even though it still slightly over predicts the circulation.

Marble (1990) suggested that a characteristic scaling time for weak shock interactions was $\tau = (r_0)^2/\Gamma$. The relevance of this time scale is illustrated by the time required for the stream of air to divide the initial jet cross section into an upper and lower lobe. The velocity of the stream of air, V_{stream}, should scale with Γ/r_0. The time for the stream to move through the entire jet should scale with the distance it must travel divided by its velocity $\tau \sim r_0/V_{stream} \sim (r_0)^2/\Gamma$.

Yang (1991) suggested that a time scale for stronger shocks is $\tau = HW/\Gamma$ where H is a characteristic height which is represented by the initial radius r_0, and W is a characteristic width which is represented by $(\rho_1/\rho_2)r_0$ so that $\tau = (\rho_1/\rho_2)(r_0^2/\Gamma)$. The relevance of this time scale is also illustrated by the time required for the stream of air to divide the initial jet cross section into upper and lower lobes. Here the velocity of the stream still scales as $V_{stream} \sim \Gamma/r_0$. However compression of the shock reduces the distance the stream must travel by a factor of ρ_1/ρ_2 and the time scales with $\tau \sim (\rho_1/\rho_2)(r_0^2/\Gamma)$. Because there is a ρ_1/ρ_2 term in the circulation which cancels with the ρ_1/ρ_2 term in the characteristic width, the characteristic time based on $\tau = (\rho_1/\rho_2)(r_0^2/\Gamma)$ with the circulation model of Yang for stronger shocks scales the same way as a characteristic time for weak waves based on the circulation model of Rudinger and Somers and $\tau = d^2/\Gamma$. For each case:

$$\tau \propto \frac{r_0}{u}\left(\frac{1+\frac{\rho_l}{\rho_h}}{1-\frac{\rho_l}{\rho_h}}\right) = \frac{r_0}{a_1}\frac{(\gamma+1)}{2}\left(\frac{M}{M^2-1}\right)\left(\frac{1+\frac{\rho_l}{\rho_h}}{1-\frac{\rho_l}{\rho_h}}\right)$$

Therefore, when trying to scale the development of the flow, the non-dimensional time (t/τ) is useful. However, another non-dimensional time which has been used by Marble (1990), and Yang (1991) is $a_1 t/r_0$. This time is important because it easily allows the flow studied in an experiment to be compared to the real flow in an engine. For a real engine a typical value for the ambient speed of sound is about 800 m/sec and a typical jet radius about 1 cm. Since the fuel will only be in the engine for 1-2 ms, the mixing must by the time $a_1 t/r_0$ is in the range 80 to 160.

Although the overall flow development has been well characterized, the previous investigations have only been able to infer limited information on the degree of mixing which occurs. In general, the results from computations regarding molecular mixing for these types of flows are not considered to be reliable. In addition, the previous experiments have not been able to measure molar helium concentrations with sufficient temporal and spatial resolution to represent molecular mixing. Experiments by Haas and Sturtevant (1987) were limited to shadowgraph photography. The experiments of Jacobs (1992) could not measure helium concentrations because of the differential diffusion between the helium and biacetyl. Concentration measurements by Waitz (1991) for the three-dimensional steady interaction were not spatially or temporally resolved.

1.3. Present Experiments

The goal of the present study was to measure the molecular scale mixing that occurs after the interaction of a shock with a laminar jet of helium. The experiments of the present study are illustrated in Figure 1-4 where a shock wave travels from left to right down a shock tube and interacts with a laminar jet of helium flowing out of the page. The shock accelerates the helium jet to the right, the cross section of the jet deforms, and the shock continues down the tube. A vortex pair forms from the helium jet. The shock reflects off the tube's end wall, travels back from right to left and interacts with the vortex pair. Experiments were performed that viewed a cross section of the jet

with planar Rayleigh scattering, or imaged a side view of the jet with shadowgraph photography (the planar Rayleigh scattering was not done simultaneously with shadowgraph).

The Rayleigh scattering technique allowed a direct measure of the molar air concentration, χ_{air}, in a two-dimensional cross section and the helium concentration, χ_{He}, was found from $\chi_{He} = 1 - \chi_{air}$. The resolution of the measurements was sufficient to temporally and spatially resolve the smallest strained diffusion scales present in the laminar flow and allowed the amount of molecular mixing to be measured. The experiments covered a range of Mach numbers to understand the scaling of the mixing with increasing shock strength.

This investigation also measures the motion of the deforming helium jet after the shock interaction. The downstream position of the helium relative to the surrounding air is analogous to the ability of a jet to penetrate the air in the three-dimensional steady interaction (Yang 1991). The motion and spacing of the vortex pair also reflect the magnitude of total circulation generated by the shock.

In addition, shadowgraph experiments were performed using a discrete circular cross section interface created by a thin plastic membrane similar to Haas (1983, 1987). These experiments complemented the jet experiments by allowing the study of shock wave interactions with a much larger inhomogeneity diameter (5cm), and the study of the effect of a discrete interface. Microfilm experiments also visualize the dynamics of a Mach 2.0 shock interaction. Mixing measurements were not made for the microfilm experiments.

CHAPTER 2

EXPERIMENTAL APPARATUS

2.1. Shock Tube Facility

The present study was performed in the GALCIT 17 inch shock tube (Liepmann et al. 1962); a side view of the driven section is shown in Figure 2-1. The transition from the circular 17 inch diameter cross section of the main tube to the 10.5 inch square cross section of the test sections was aided by a "cookie cutter" that prevented the waves caused by the change in cross sectional area from interfering with the experiment. Two 2 ft long test sections could be attached in series to the cookie cutter; the first had a 6 inch diameter window on the bottom, while the second had two 6 inch diameter windows on its sides. A back end plate, also with a 6 inch diameter window, closed the tube. All of the windows were flush with the walls of the test sections or end plate.

The main shock tube and the test sections were each fitted with two model 112A21 PCB piezoelectric pressure transducers. The output of pressure transducers was recorded on an RC Electronics Model ISC-67 Computerscope board installed in an IBM model AT computer. The shock wave velocities were found by dividing the known distance between the transducers by the time for the shock to travel from one transducer to the next. The Mach number was calculated by dividing the velocity with the speed of sound for air at the measured temperature. Additional details of the Mach number measurement are in Appendix B. The transducers were also used to trigger a Stanford Research System model DG535 digital delay/pulse generator which controlled the timing of the data acquisition systems.

2.2. Imaging Systems

Planar Rayleigh scattering was the primary diagnostic used in the investigation. For a mixture of helium and air the relation for the scattering signal is:

$$\text{Signal} \sim n\,(\alpha_{air}(1-\chi_{He})+\alpha_{He}\chi_{He})$$

where n is the number density of molecules, χ_{He} is the mole fraction of helium, and α_{air} is the scattering cross section of air molecules and α_{He} is the scattering cross section of helium atoms. Since α_{air} is 66 times larger than α_{He}, pure air scatters 66 times more light than pure helium. The signal also depends on the pressure and temperature through the number density. As explained in section 5.1 the pressure variations after the shock interaction were negligible, and a first order correction could be made for the variation in temperature, so that molar helium concentrations could accurately be calculated.

To implement the scattering technique, cylindrical lenses were used to transform a pulsed laser beam into a thin sheet of light. The laser sheet intersected a cross section of the deforming helium jet, and the scattering off the molecules generated an image in the plane of the laser sheet that was captured by a cooled CCD camera. In the picture, the air was bright and the helium was dark. A calibration procedure outlined in Appendix C was used to account for the variations in light intensity not related to the concentration variations. Only one picture could be taken each time the shock tube was fired; a sequence was built by performing multiple experiments. To complement the scattering technique, additional experiments were performed in which a standard shadowgraph system imaged a side view of the jet.

The two imaging systems used in this study are shown in Figure 2-2. For a Rayleigh scattering experiment the jet was placed upstream of the window in test section 1 as shown in Figures 2-1 and 2-2. After being accelerated by the shock, the helium moved into view of the camera. At that time, a Candela SLL-1050M flashlamp pumped

dye laser generated a 700 nsec long 4 J laser pulse at 480nm using the dye Coumarin 480. A prism tuner, installed in the laser, narrowed the wavelength bandwidth and vertically polarized the beam. Since the scattering signal is maximized in a direction normal to the polarization, a half wave plate rotated the polarization 90 degrees into a horizontal orientation. Figure 2-2 shows the beam passing through sheet forming optics, the half wave plate, and into the test sections. The sheet was less than 1.5 mm thick as it cut through a cross section of the jet.

A Photometrics Star I cooled CCD camera system, which is shown in Figure 2-1 below the window in test section 1, was mounted on a horizontal translator. The camera had a minimum shutter exposure time of 0.1 seconds and used a Nikon lens that had an f-number of 2.8 with a 105 mm focal length. The CCD had an array of 576 by 384 square pixels each 20 microns on a side. The Star I system came with a camera controller with a 12 bit A/D converter which could read out and store one image at a time. The images were transferred from the camera controller to a Gateway 2000 386/33 AT compatible computer through an IEEE-488 GPIB board installed in the computer. For most of the experiments, the camera's axis of view was vertical, looking straight up through the window of the test section. For some early time pictures, because the jet started upstream of the window, the camera view axis had to be inclined 15 degrees from the vertical position to view the cross section. Corrections were made for the distortion of the image caused by this angle in the quantitative analysis. However, the pictures in Chapter 3 which show the qualitative development of the deformation of the jet cross section were not greatly affected by this angle and were not corrected.

The shadowgraph system shown in Figure 2-2 was based on a standard focused spark shadowgraph system using a Nanolamp spark light source, and either a 35 mm camera, or a General Electric TN2505 CID camera connected to a Poynting Products PC-170 frame grabber in an IBM/AT computer. The jet for a shadowgraph experiment was placed in one of the two locations in test section 2 shown in Figure 2-2. The position

in the center of the window was used for pictures taken shortly after the shock interaction. The location upstream of the windows in the second test section was used for viewing the jet at longer times after the shock interaction.

2.3. Reflected Shock Configurations

After the shock wave interacted with the helium jet, it continued down the shock tube and reflected off the end plate. With both test sections in place the distorted helium jet would translate past the window before an interaction with the reflected shock could occur. To view the reflected shock interaction, the second test section was removed and the end plate placed on the back of the first test section. The distance between the jet and the end wall was 11.75 inches which allowed the reflected shock interaction to occur within the view of the window for the Mach 1.07 and 1.14 shock waves. For the Mach 2 shock waves, the helium would still translate past the window before the interaction could occur. For this case a plate was offset 5 inches from the back end plate as shown in Figure 2-3. A 0.25 inch thick, 1.5 inch long slot was machined in the plate to allow the laser sheet to pass into the test section. Although this was not an ideal boundary condition since air moved through the slot, the experiments still serve to illustrate the main points of the reflected Mach 2 shock interaction.

2.4. Helium Jets

Two different methods of introducing a helium jet into the shock tube were employed. The first jet experiments performed (Mach number of 1.15, with the driven pressure at one atmosphere) used the same jet apparatus as Jacobs (1992), which is shown in Figure 2-4. Two copper tubes with 3/8" outside diameter, entered the test section through the side wall. One tube supplied helium which flowed out of a high pressure bottle through a pressure regulator, a rotameter, and a needle valve into the test section. As shown in Figure 2-4, this tube bends downward along the side wall, then towards the center of the tube along the bottom wall, before finally turning upwards and

ending at the jet exit. Also in Figure 2-4, the second tube, which was attached to an ejector type vacuum pump, ran along the top wall and came down above the jet to remove the helium and prevent contamination of the air inside the test section. The total frontal area of this apparatus was about 10% of the total test section cross sectional area.

Later experiments used the primary jet apparatus which only had one brass tube with an O.D. of 3/8", and an I.D. of 0.305 inches enter the test section through the bottom and extend upwards 2 inches into the test section. This single tube had a frontal area less than 1% of the test section cross sectional area and thus had much less flow blockage than the first apparatus. The shock waves which reflected off this apparatus were weaker, and presumably interfered less with the experiment. In addition, the helium traveled a straighter path just before exiting the jet nozzle.

The helium for this jet was also supplied by a high pressure bottle, passed through a pressure regulator, monitored by a pressure gauge, and passed through a rotameter with a needle valve on its exit, before entering the test section. A 9/16" diameter exit orifice, connected to a Welsh vacuum pump, was located above the helium jet, flush with the upper wall of the test section 1. For both jet configurations, the vacuum pump was typically on for less than thirty seconds before an experiment and had a volume flow rate of about 3 liters/min, which indicates that the pressure change in the 1000 liter volume of the shock tube's driven section was negligible.

During an experiment, a laminar helium jet was created using one of these two methods. When the shock tube was fired, the wave traveled down the tube, passed over and accelerated the helium. At a designated time set on the delay/pulse generator a picture was taken. Only one picture could be acquired per experiment. Time sequences were generated by repeatedly firing the tube and varying the delay on the pulse generator.

2.5. Cases Studied with a Helium Jet

The deformation of a jet of helium after an interaction with a shock wave was studied for four different shock Mach numbers: 1.07, 1.14, 1.50, and 2.0. In addition, the effect of the reflected shock interaction was studied for Mach numbers 1.07, 1.14, and 2.0. To keep the pressures in the test section after the reflected shock within the safe limits of the structure, the driven section of the shock tube was pumped down for the higher Mach number experiments. Since the scattering signal is proportional to the number density of molecules, the signal was lower for the higher Mach number cases. In addition, the 1.14 Mach number interactions were studied with the pressure in the test section before the shock at 1 atmosphere, and at 0.55 atmospheres. Table 2-1 summarizes the conditions studied.

Table 2-1.

Mach #	Waves	p_1 (atm)
1.07	initial & reflected	1.0
1.14	initial	1.0
1.14	initial & reflected	0.55
1.50	initial	0.23
2.0	initial & reflected	0.08

For the cases with the jet initially at one atmosphere, the jet had a helium volumetric flow of 60 cm^3/sec. This resulted in an average velocity of 130 cm/sec at the exit and a Reynolds number of 75 based on the average velocity, the jet diameter, and the kinematic viscosity of helium. For the cases where the initial pressure was below atmospheric in the test sections, the jet Reynolds number was kept at 75 by keeping the helium mass flow rate the same.

For Mach numbers 1.07, 1.50 and 2.0, the plane of the laser sheet intersected the helium jet 5.7 diameters above the jet exit. For the Mach 1.15, some experiments were performed with the laser sheet 4.9 diameters above the jet exit, and some with the laser sheet 5.7 diameters above the jet exit. At these distances air had diffused into the center of the jet. Table 2-2 summarizes, for the different cases studied, the height of the laser sheet plane above the jet exit, the center line molar helium concentration $\chi_{He}(r=0)$, and the radius of the jet cross section (based on the radius at which the concentration was 1/2 the center line concentration).

Table 2-2.

Case Mach#,p_1	h/D	$\chi_{He}(r=0)$	r_o (cm)	$r_o d\chi/dr$
1.07, 1 atm	5.7	0.89	0.46	0.66
1.14, 1 atm	4.9	0.92	0.45	0.70
1.14, 0.55 atm	4.9	0.94	0.55	0.66
1.14, 0.55 atm	5.7	0.92	0.55	0.66
1.50, 0.23 atm	5.7	0.92	0.62	0.57
2.0, 0.08 atm	5.7	0.92	0.63	0.55

2.6. Membrane Cylinder Experiments

Shadowgraph experiments were also performed on discrete density inhomogeneities similar to those used by Haas and Sturtevant (1987). For these experiments, the jet of helium was replaced by a cylindrical volume of helium contained in a thin plastic membrane. As shown in Figure 2-5 the membrane, which was of the type used in ultra light model airplanes, was stretched around a membrane holder generating a cylindrical interface which separated the helium from the air. The membrane holder consisted of two 5 cm diameter plexiglass disks supported by 1/8 "

O.D. brass tubes. The tubes also circulated helium into and out of the membrane enclosed cylinder. The membranes were typically about 0.1 micron thick and had a mass about 1/8 the mass of the helium contained within the membrane (when the helium and surrounding air were at 1 atm absolute pressure).

In the first few experiments, the holder was positioned in the center of the window of the test section in order to view the dynamics of the shock wave interaction with helium cylinder. In later experiments, the holder was positioned further and further upstream of the window center, so that the moving, distorted inhomogeneity would have translated into the center of the window when the picture was taken.

The membranes were created by placing several drops of a commercially available microfilm solution (IMS FAA standard B) on a pool of water. The microfilm solution, which is essentially nitrocellulose dissolved in a solvent, spread out uniformly in a thin layer over the water. After the solvents evaporated, the nitrocellulose membrane was picked up on a balsa wood frame.

The membranes were placed on the holder by first placing the membrane on the plate in Figure 2-6, applying double stick tape to the plexiglass disks, and then rolling the plexiglass disks and the rest of the holder on the plate. The membrane sticks to itself, and so completely enclosed and sealed the cylinder.

2.7. History of the Project.

The present work was a continuation of a project to experimentally study shock enhanced mixing in the GALCIT 17 inch shock tube. The project was initiated by Dr. Marble with a grant through the Air Force University Research Initiative in 1986, at which time the facility consisted of the basic shock tube (as described in Liepmann et al 1960), one 10.5 inch square test section, and a "cookie cutter" which was only suitable for very weak shock wave experiments.

The majority of the early work on the experimental project in the 17 inch shock tube was done by research fellow Dr. Jeff Jacobs (1992). With the advise of Zukoski and Marble, Jacobs developed the technique of using the PLIF of the tracer dye, biacetyl, to visualize the flow and purchased the Candela laser and an intensified video camera to be used with the technique. Jacobs also acquired a frame grabber board and an IBM/AT computer to digitize the video images, two delay/pulse generators to control the timing of the experiments, two piezoelectric transducers to measure the pressure, and a RC Electronics Computerscope board with a second IBM/AT computer to record the pressure traces. Jacobs was also primarily responsible for the design of a second test section, a stainless steel "cookie cutter", and the stands around the test sections used to support the imaging and laser systems.

The author of the present investigation and Joe Yang helped Jacobs to build the stands around the test sections, assemble the test sections and new "cookie cutter", construct the helium supply system, and set up the laser, intensified camera, and shadowgraph systems.

After the conclusion of the experiments of Jacobs (1992), the author of the present investigation was solely responsible for the switch to and the development of the planar Rayleigh scattering technique. To make this change the laser system was modified by changing the laser dye from LD423 to Coumarin 480, adding a prism tuner to the laser to polarize the beam, and inserting a 1/2 wave plate into the beam path to properly orient the polarization. Furthermore, the intensified video camera purchased by Jacobs was not suitable for quantitative measurements of molar air concentrations and a different imaging system (which included a Photometrics Star I camera system, an IEEE-488 GPIB board, and a Gateway 2000 386/33 AT compatible computer) was purchased. A new method for introducing the helium jet into the test section was developed that replaced the apparatus used by Jacobs, which filled 10% of the cross sectional area of the test section, with an apparatus which filled less than 1% of the area of the test section.

Two additional pressure transducers were purchased to allow the Mach number to be measured in the main shock tube as well as in the test sections.

CHAPTER 3

FLOW VISUALIZATION

3.1. Rayleigh Scattering

3.1.1. Introduction

This chapter qualitatively describes the deformation and motion which occurs after the interaction of a shock wave and a cylindrical volume of helium. The first experiments described are those in which the cylindrical volumes were created with a laminar jet of helium and the cross sections were observed with planar Rayleigh scattering. Next, a description is given of experiments which used shadowgraph photography to image the side view of the shock-jet interaction. Finally, experiments are described which used shadowgraph photography to view shock interactions with a cylindrical volume of helium contained within a microfilm membrane.

The conventions which are used to describe the vortex pair structures which form after the shock interaction are shown in Figure 3-1. In all the pictures that are shown, the shock wave has moved from left to right, and hence the flow in the laboratory reference frame is from left to right. The vertical axis is defined as the 'y' axis, and $y = 0$ is the symmetry line of the structure which corresponds to the 'x' axis. The upper vortex is in regions where $y > 0$ and has counter-clockwise circulation. The lower vortex is in regions where $y < 0$ and has clockwise circulation.

3.1.2. Mach 1.07 Shock Wave

Figure 3-2 is a sequence of false-color planar Rayleigh scattering pictures showing the deformation of a cross section of a jet of helium (5.7 diameters above the jet exit) after the passage of a Mach 1.07 shock wave. The different colors in the picture, as

indicated by the color bar above the sequence, represent different mole fractions of helium; in the color bar pure helium is black, pure air is yellow-gray. The last picture in the sequence is $a_1t/r_0 = 250$ which is 2 or three times longer than the fuel residence time (a_1t/r_0 = 80 to 160) estimated in Chapter 1. Figure 3-2a and b were taken with the camera inclined 15 degrees, while the rest of the sequence was taken with the camera normal to the window. Figure 3-2a shows the jet cross section after the diaphragm of the shock tube broke but 0.2 ms before the shock wave reaches the jet. As the incident shock wave passes over the helium jet from left to right, vorticity is generated where the density gradients of the jet are not parallel to the pressure gradients of the shock wave. Counter clockwise vorticity is produced on the top of the cross section and clockwise vorticity on the bottom. As shown in Figures 3-2a through c, this vorticity first causes a stream of air to move through the center of the initially circular helium distribution, dividing the inhomogeneity into an upper lobe and a lower lobe connected by a thin strand of fluid. Each half is further divided into a back lobe or tail region, and a front lobe where computations (Picone and Boris 1988, Yang 1991) show most of the vorticity is concentrated. In Figure 3-2d the front lobes form a vortex pair which starts to pull ahead of the tail regions. As time progresses in Figures 3-2e through 3-2h, the vortex pair pulls further ahead of the tails, the tails are strained and grow thinner and longer. The induced motion from the vortex pair moves the tail regions closer to the symmetry line, and the tails are slowly wrapped around the vortex cores, which causes the width of the region of high air concentrations (represented by the yellow/gray region in the picture) between the upper and lower vortex pairs to decrease.

The propagation of the light in the laser sheet is from right to left in the pictures. As the sheet passes through the helium, the index of refraction gradients that are associated with the density gradients slightly refract the light in the same way that light is refracted to produce shadowgraph pictures. This effect is visible as horizontal streaks in some of the pictures to the left of the helium.

In Figure 3-2c the highest concentrations of helium are associated with the black-green color in the tail and core region. As the sequence progresses in Figures 3-2 d, e, f, g, and h, the black color in the cores completely disappears, and the area of green continually decreases. These color changes show that air is diffusing into the center of the cores. A greater difference is observed in the colors in the tail regions. In Figures 3-2c,d,e,f,g, and h, the color in the center of the tails changes from green-black to green to blue and finally to red. The greater change in colors indicates more mixing is occurring in the tails than in the cores as the vortex pair moves ahead of and strains the tail regions.

Figures 3-2i through 3-2*l* show what happens when the reflected shock wave passes over the vortex pair at time $a_1t/r_0 = 110$ (just after 3-2d). Once again vorticity is baroclinically generated where the pressure and density gradients are not parallel. To allow a qualitative sense of where the additional vorticity will be generated, an enlarged picture of Figure 3-2d is shown in Figure 3-3. Above the picture is a plot of molar helium concentrations for varying x along the line $y/r_0 = 0.80$, which is shown in the picture as a horizontal line through the center of the upper vortex. To the left of the picture is a plot of molar helium concentrations for varying y along the line $x/r_0 = 3.21$, which is shown in the picture as a vertical line through the center of the upper vortex. The circulation in the upper vortex just before the reflected shock is counter-clockwise. The plot to the left of the picture in Figure 3-3, shows that the density gradient at the top of the upper vortex (around $y/r_0 = 2.54$) is negative, while the density gradient at the bottom of the upper vortex (around $y/r_0 = 0.3$) is positive. These density gradients combine with the pressure gradient of the reflected shock to generate clockwise vorticity (which is opposite in sign to the circulation just before the reflected shock) at the top of the upper vortex (around $y/r_0 = 2.54$), and counter-clockwise vorticity (which is the same sign as the circulation just before the reflected shock) at the bottom of the upper vortex (around $y/r_0 = 0.3$).

As explained in (Yang 1991), the reflected shock transforms the upper vortex into two regions of opposite sign vorticity. Because there was vorticity in the core before the reflected shock, the magnitude of the total circulation in the two regions is not equal. The region closer to the symmetry line, where the vorticity generated by the reflected shock added to the vorticity present after the initial shock, has a stronger total circulation than the region of opposite vorticity further from the symmetry line, where part of the vorticity generated was negated by the vorticity present after the initial shock.

Above the symmetry line, the stronger vortex induces a motion which rotates the weaker vortex clockwise, and tears away part of the helium that before the reflected shock was in the upper vortex core. In Figure 3-2i, two 'tail regions' are observed; the first one from the left developed from the tail region in Figure 3-2d, while the second one from the left, represents the helium which was torn away from the core region in Figure 3-2d and contains clockwise vorticity.

In Figure 3-2j, the region of strong counter-clockwise vorticity above the symmetry line and the region of strong clockwise vorticity below the symmetry line form a main vortex pair which moves away from the tail regions as seen in Figures 3-2k and *l*. The distance between the cores of this main vortex pair in Figures 3-2j,k, and *l* is less than the distance between the vortex cores in Figure 3-2e,f,g,and h without the reflected shock. This decrease in the distance occurs because above the symmetry line the reflected shock interaction removed the counter-clockwise vorticity furthest from the x-axis, and added counter-clockwise vorticity closer to the symmetry line. Likewise, the vorticity in the main clockwise vortex below the symmetry line is shifted up towards the x-axis. Furthermore, the weak clockwise vortex above the symmetry line and the weak counterclockwise vortex below the symmetry line, which were left behind in the tails, induce velocities on the main vortex pair that would tend to move them closer together.

The reflected shock interaction also generates vorticity in the tail regions of Figure 3-3. Before the reflected shock, the tails contained little vorticity, and the vorticity

generated by the reflected shock interaction forms vortex pairs that are seen in Figure 3-2k. The clockwise vorticity that was generated on the outside edges of the original upper vortex core in Figure 3-3, becomes a visible clockwise vortex in Figure 3-2*l*.

If only one shock interaction occurs (Figures 3-2e through h), the tail regions move closer to the centerline, the width of the region of high air concentrations (the yellow band) between the cores decreases, and part of the tails are wrapped around the cores. Likewise, after the reflected shock in Figures 3-2i to *l*, the main vortex pair strains the tails, decreases the width of the region of high air concentrations between the cores, and wraps part of the tails around the main cores. Because the vortex cores are closer after the reflected shock, the width of the region of high air concentrations between the cores quickly becomes thinner compared to the case without the reflected shock as the tails are wrapped around the cores.

3.1.3. Mach 1.15 Shock Wave

Figure 3-4 shows the interaction of a 1.15 shock wave with a helium jet where the initial pressure was one atmosphere. For frames a,b,c, and d in the sequence, the camera was inclined at a 15 degree angle. The jet is shown in Figure 3-4a before the shock tube was fired. This sequence shows the shock moving through the jet cross section. In Figures 3-4d and e, the shock wave runs through the helium faster than through the air, resulting in a curved shock. Haas found in his work with discrete inhomogeneities that the incident wave generated refracted and reflected waves at the air-helium interface, which in turn generated progressively weaker waves ad infinitum. However, these waves do not show up here, partly because the interface is diffuse, and partly because additional waves are too weak to be seen with the scattering technique. The rest of the sequence develops very similarly to the Mach 1.07 case.

A sequence after the passage of a Mach 1.14 shock with the pressure in the test section initially 0.55 atmospheres is shown Figure 3-5. Since the pressure is lower, the number density of molecules is lower, which causes the signal to noise ratio to be lower and the pictures to be more grainy. Figures 3-5a,b, and c were taken at an angle of 15 degrees while the rest of the sequence was taken with the camera vertical. Figure 3-5a shows the jet after the diaphragm broke but 0.2 ms before the shock hits the jet. The progression is similar to Figure 3-5 until a reflected shock wave passes through the vortex pair at $a_1 t/r_0 = 82$, which is just after the time of Figure 3-5f. The overall development after the second wave parallels the reflected shock interaction of Figure 3-5. Since the tail region was originally smaller, the vortex pairs formed after the reflected shock are less obvious.

3.1.4. Mach 1.5 Shock Wave

Figure 3-6 shows a Mach 1.5 shock interaction. A different false color scheme is used for this sequence. The pressure was further decreased for this case, which results in higher noise and more grainy pictures. All of the pictures in this sequence were taken with the camera vertical. The shock wave after passing through the jet is seen at the right of Figure 3-6a. The white and black area in the shock is a large particle. The tails in this sequence are even smaller and thinner than the Mach 1.15 cases, continuing the trend.

3.1.5. Mach 2.0 Shock Wave.

Figures 3-7a through g show a Mach 2.0 shock interaction and Figures 3-7 h to k show the interaction of the vortex pair with the shock that rebounds off the end wall. As indicated in section 2.3, the end wall for the reflected shock experiments had a small slit machined through it to allow the laser sheet to pass into the test section, and hence allowed gas behind the reflected shock to leak through. In Figure 3-7i, the distance

between the vortex pair and the end wall just after the reflected shock interaction is about twice the vortex core spacing, and hence the presence of the end wall and slit may have affected the motion. However, the flow visualization is still valuable. All of the pictures in Figure 3-7 were taken with the camera in a normal orientation. The initial shock is still visible as a transition from yellow to purple in Figures 3-7a and b. The development of the vortex pair including the tail regions is almost identical to the Mach 1.5 case.

The reflected shock as shown in Figure 3-7h becomes curved as it travels through the vortex centers. This curved shock is the result of two effects; first the induced velocity of the vorticies greatly impedes the progression of the shock wave between the cores, while increasing the wave speed above and below the vortices. Second, the higher speed of sound of helium allows the shock wave to move faster through the cores than outside of them. The curved surfaces lead to the formation of sharp corners and the development of two triple-point intersections. The intersections can be seen in Figure 3-7i, where the strongest shock is represented by a transition from purple to yellow and weaker shocks can be seen as a transition from yellow to black. The triple-point intersections generate vortex sheets that can be seen in Figures 3-7i,j and k.

In Figures 3-7i,j and k, two thin strands can be seen to the left of the vortex cores. The left most strand is what is left of the tail region before the shock interaction, while the right strand is fluid torn from the cores by the reflected shock.

The development of the vorticity produced in the tail regions due to the reflected shock is substantially different than what occurred in the lower Mach number cases. When the reflected shock hits, the tails have almost formed a 90 degree arc, being nearly vertical in Figure 3-7g near their left tip and horizontal as they are entrained into the vortex cores. As the shock passes through the tails, little vorticity is produced at the left vertical tip, with most of the vorticity being produced as the tail turns horizontal and the density gradients become perpendicular to the pressure gradient. Once again vorticity of both signs is generated. The main difference from the lower Mach number case is that

the vorticity in the tail regions can not escape the main vortex pair and becomes entrained into their cores. The vorticity in the tail regions first shows up as minor bumps on the front part of the tail strand being swept around the right edge of the vortex cores in Figure 3-7i. Regions of vorticity of opposite sign to that in the main cores can be seen in Figure 3-7j just to the right of the main cores. These regions are strained around the cores in Figures 3-7k.

3.1.6. Comparison with Computational Results

The qualitative development of the deformation of the cross section agrees well with the jet experiments of Jacobs (1992), and the computations of Yang (1991), and Picone and Boris (1988).

The Yang computations assumed a less diffuse initial interface than that studied in the experiments. Overall the computations look very similar to the experiments. The main differences appear in the tails of the structures especially after the reflected shocks. Since the interface is more diffuse in the experiments, there is more helium further away from where the vortex cores form. Hence, more helium trails after the vortex cores and adds to the tail regions. Since the tails are larger, more vorticity is deposited there when the reflected shock passes, resulting in the more prominent tail vortex pairs in the 1.07 Mach number case, and the regions of opposite vorticity in the Mach 2.0 case.

3.2. Shadowgraph

The main purpose of the side view shadowgraph images was to check for variations in the flow normal to the plane of the laser sheet. If the flow was not predominately two-dimensional, straining perpendicular to the plane of the laser sheet could create mass loss or gain in the cross section, and cause uncertainty in the mixing measurements. In addition, the laser sheet must be thin enough to prevent the variations in this third dimension from affecting the concentration measurements. Large changes over the sheet

thickness will inaccurately represent the variation in concentration through the sheet thickness as a single average concentration.

Figure 3-8 is a shadowgraph sequence showing a jet after the passage of a 1.07 shock wave. In the first picture which shows the jet just before the interaction with the first shock wave (which can be seen to the left), a small disturbance is visible about 5 cm above the jet exit. Since the fluid in the region of the disturbance was emerging from the nozzle at the time the diaphragm broke, the perturbation was most probably caused by the recoil of the shock tube. Figures 3-8b and c show the motion of the jet after the passage of the shock wave. Figure 3-8d shows the jet just before the interaction with the reflected shock (which is to the right of the jet). The variations in the deforming jet, which are perpendicular to the plane of the laser sheet and visible in the shadowgraph pictures, occur on a scale of many jet diameters. This scale of the variations indicates that the laser sheet thickness of about 1/10th the diameter of the jet is thin enough to prevent these variations from affecting the measurement of helium concentrations.

Figure 3-9, Figure 3-10, and Figure 3-11, show respectively a sequence for a Mach number 1.15 shock with $p_1 = 0.55$ atm , a single picture for a Mach 1.15 shock with $p_1 = 1$ atm, and a single picture for a Mach 1.5 shock. Virtually no three-dimensional disturbances can be seen in Figure 3-9. In the Mach 1.5 case, and to a lesser degree in Figure 3-10, some variations due to the amplification of the shock tube recoil disturbance are visible. However, the cross sections (shown by dashed lines) where the laser sheet cuts the jet are free from three-dimensional disturbances, indicating that helium concentrations will accurately be represented. The main concern is whether the visible disturbances create straining motions that increase or decrease the amount of helium in the cross section of the laser sheet. Since the shadowgraph picture is only qualitative, a definite statement can not be made. However, the disturbances appear to be small compared to the jet diameter, and may have little effect on the cross section of the laser sheet.

In Figures 3-9, and 3-10, the jet becomes slanted with the bottom part of the jet further ahead of the top part. The scaling laws for the circulation given in Chapter 1 indicate that greater circulation will be generated for lower ratios of ρ_ℓ/ρ_h. Since air diffuses into the jet cross section, ρ_ℓ/ρ_h increases as the distance above the jet exit increases. Greater circulation is generated nearer the jet exit, and this part of the jet moves faster, which results in the visible slant.

3.3. Microfilm Cylinders

3.3.1. Mach 1.1 Shock Interaction

As mentioned in the introduction, microfilm cylinders are useful in looking at the dynamics of the shock wave interaction with a single circular density inhomogeneity. Haas and Sturtevant (1987) thoroughly studied weak wave interactions with helium microfilm cylinders and found that when a shock interacts with a helium cylinder, waves are refracted and reflected from the interface between the air and the helium. The refracted wave itself interacts with the interface, and generates a transmitted wave, and an internally reflected wave. All of the internally reflected waves interact with the air-helium interface producing ad infinitum other waves which grow progressively weaker.

Figure 3-12 shows the deformation of a cylindrical volume of helium which follows the wave interactions discussed above for a Mach 1.1 shock wave. The mass of the microfilm was about 1/8 the mass of helium in the cylinder. This Mach 1.1 interaction is very similar to the Mach 1.085 case studied by Haas (1983). The major differences were that the test section height in Haas' experiment was 1.78 cylinder diameter, while it is 5.25 in the present study, and that the present study was carried out for longer times, and viewed the interaction with a reflected shock wave. In Figure 3-12i a reflected shock is seen approaching from the right. Figure 3-12j was taken just after the interaction, and some residual waves can still be seen. Figure 3-12*l* indicates that part

of the vortex centers have torn away by the reflected wave. Despite the discrete interface and the larger diameter, this picture is very similar to Figure 3-2k.

3.3.2. Mach 2.0 Shock Interaction

Figure 3-13 shows the interaction of a Mach 2.0 shock wave with a helium cylinder (the shock wave and cylinder move from left to right). To generate these pictures the shock tube had to be evacuated to a tenth of an atmosphere, which means the mass of the microfilm membrane is now about equal to the mass of helium in the cylinder. Despite these limitations the sequence of pictures can be used as an aid in reviewing the dynamics of a shock wave interaction with a cylindrical volume of helium, and shed some light on how the interaction changes as the shock Mach number increases well beyond what could be considered a weak wave.

Many of the characteristics of the weak wave interaction are found to be similar to this stronger wave interaction. In Figure 3-13a, at a time of 15 μsec (time zero is when the shock first touched the cylinder's left edge), the transmitted wave can be seen running ahead inside the cylinder, with a reflected shock in the air to the left of the helium. The air-helium interface is already greatly deformed, moving much faster than in the weak waves studied by Haas.

A simple analogy to this early time is the interaction of a shock and a plane interface between helium and air. A Mach 2.0 incident wave at a plane interface causes a Mach 1.5 shock to enter the helium and an expansion wave to reflect back into the air. This implies an expansion wave should have reflected of the left edge of the cylinder. However, at an interface between regions with different densities, the shadowgraph imaging places a white line on the higher density side and a dark line on the lower density side, indicating that the reflected wave is a shock. The fact that a shock is reflected is an effect of the microfilm membrane. In order for the mass of the membrane

to be accelerated there must be a pressure difference across it. This is provided partly by the reflected shock, and partly by a weakened transmitted wave.

At 37 μsec a shear layer has formed at the top of the deforming cylinder, representing the interface between the air that has just had one shock wave travel over it, and air that has had both the incident and reflected shock waves travel over it. Presumably, since a shock is reflected instead of an expansion, the shear layer has vorticity opposite to the vorticity which would be generated without the membrane. It also becomes apparent that the refracted shock inside the cylinder does not travel as far in front of the incident shock as was the case for the weak wave interactions studied by Haas. This is partly explained by the membrane weakening the wave. However, at the air-helium interfaces in general, as mentioned above for the plane interface case, the transmitted wave has a lower Mach number (1.5 in helium compared to 2.0 in air) than the incident wave. For a weak wave interaction, this weakening is less apparent since both the incident and transmitted wave Mach numbers are close 1.0. Thirdly, the wave bows out as it travels through the cylinder, indicating its total arc length is increasing, and hence its strength is decreasing.

Another interesting observation is that the reflected shock remains in the same position relative to the shock tube window as time increases. This should not be surprising, however, since in the laboratory reference frame, the Mach number of the air behind a Mach 2.0 shock wave is 0.96, indicating that weak waves should travel upstream very slowly. Also seen is a disturbance which appears to be generated at the point where the brass tubes enter the plexiglass disks.

At 55 μsec, the primary refracted wave has been transmitted through the right edge of the cylinder, and intersects the incident wave just above the inhomogeneity. Although internally reflected waves can be seen just about to pass through each other, the secondary transmitted waves which Haas saw connected to the internally reflected waves

are hard to distinguish from the primary transmitted wave. The originally circular helium inhomogeneity has been greatly compressed.

At 0.138 ms, the first reflected wave still has not moved very far, and the internally reflected wave has been transmitted through the left end of the inhomogeneity. The entropy layer can still be seen attached to the top of the inhomogeneity. The transmitted shock has already almost flattened. 3-16e, and 3-16f, show the continuing development of the inhomogeneity at 0.3, and 0.44 ms. Unfortunately, all that can be seen is the microfilm shredding, and the pictures can not be considered to accurately reflect the motion of a flow without a membrane

CHAPTER 4

THE MOTION OF THE VORTEX PAIRS

4.1. Introduction

The position of the helium center of mass fraction after the passage of the shock is important because it can be related to the distance between the hydrogen and the wall of a combustor in the three-dimensional steady interaction (Yang 1991). The position of the helium center of mass fraction is defined in Appendix D.

Furthermore, the motion and spacing of the vortex pair reflect the magnitude of the total circulation generated by the shock. For a point vortex pair, the magnitude of the circulation about each vortex is related to the velocity, U_v, of the vortex pair relative to the surrounding air, and the distance, y_v, between the vortex centers through the relation $\Gamma = 2\pi U_v y_v$. Since the vortex pair formed in the experiments has a finite core, the point vortex pair relation will not hold exactly, but the product $U_v y_v$ may at least scale with the circulation.

Computations (Picone 1987, and Yang 1991) show that most of the vorticity generated by the shock coalesces in the front lobes to form the vortex pair, and very little of the vorticity generated is in the tail regions. This indicates that the velocity and spacing of the vortex pair represent the total circulation deposited by the shock better than the motion of the center of helium mass which depends on the position of the tail regions. From Chapter 3 it was found that the tail regions mix faster than the vortex core regions, and very quickly the vortex cores appear to become coincident with the regions of highest helium concentrations. The motion of the vortex pair is modeled by studying the motion of the regions where the highest concentrations of helium exist. Definitions

of the position and spacing of the vortex pairs based on the regions of highest helium concentrations are given in Appendix C.

Another reason for calculating the position and spacing of the vortex pairs is that they are easily defined quantities which lend themselves to comparison with the results of previous computational investigations. The most similar computational investigation to the present experiments was performed by Yang (1991) who studied the position of the center of mass fraction of helium.

For an experiment, the position is first measured in the laboratory reference frame and the downstream displacement relative to the air behind the shock is $x_r = x_l - ut$, where x_l is the position in the laboratory, x_r is the position relative to the surrounding air based either on the highest helium concentrations or on the center of mass fraction, t is the time (t = 0 occurs when the shock is in the center of the jet), and u is the velocity of the air calculated using the normal shock relations for a perfect gas:

$$u = \frac{2a}{\gamma+1}\left(M - \frac{1}{M}\right) .$$

It should be noted that the measurement of the helium position relative to the air behind the shock is very sensitive to small errors in the Mach number. For example, for a Mach number close to one, the jump in velocity across the shock is proportional to (M-1). In addition it is found that the velocity of the vortex pair is on the order of 10% of the jump in velocity across the shock. For a Mach 1.1 shock this implies that a 1.0% error in the Mach number would generate a 10% error in the calculated velocity behind the shock, and would cause a 100% error in the relative velocity of the vortex pairs. The Mach numbers are estimated in Appendix B to be known within about 0.1%.

4.2. Downstream Displacement of the Helium Relative to the Surrounding Air.

Figure 4-1 shows the downstream displacement of the deforming helium jet vs. $a_1 t/r_0$ (a_1 is the sound speed, t the time, r_0 the radius) for Mach number 1.066, with the

cross section being viewed taken at 5.7 diameters from the jet exit. Figure 4-1 shows both the position of the vortex centers based on the highest concentrations of helium and the center of mass fraction. After a well developed vortex pair forms, a straight line is fit to the positions of the highest helium concentrations; the slope of the line is taken to be the velocity of the vortex cores. The velocity appears to be constant to within the scatter of the data.

In Figure 4-1, the position measurement based on the regions of highest helium concentrations is further downstream than that based on the helium center of mass, and the difference increases slightly with time. This is consistent with the discussion of Chapter 3 where it was found that the vortex centers pull ahead of the tail regions. Hence, the centers of mass fraction which are based on the mass of helium in the tails as well as the cores are not as far downstream as the vortex core centers.

Figures 4-2, 4-3 and 4-4 show respectively, the downstream displacements for the cases where M = 1.142 with p_1 = 0.55, M = 1.50, and M = 2.00. Straight lines which are fit to the regions of highest helium concentrations are also shown. Once again the velocities appear to be constant, and the centers of highest helium concentration are further downstream than the centers of mass fraction.

Figure 4-5 shows the position measurements for the Mach 1.146 case with p_1 = 1 atm. The curve has an anomalous 'S' shape indicating that the velocity was not constant. The case in Figure 4-5 was the only case to use the jet apparatus developed by Jacobs which had a frontal area that was 10% of the test section cross sectional area, while the other experiments where the velocity was found to be relatively constant used the primary jet apparatus, that had a frontal cross sectional area less than 1% of the test section area. The computations by Yang (1991) also showed constant velocities after the formation of the vortex pairs. The flow behind the shock is incompressible which indicates that a blockage of 10% can create velocity variations in the downstream direction on the order of 10% of velocity behind the shock. This could cause errors in

the calculated velocity of the deforming helium jet relative to the surrounding air. These errors could be on the same order as the velocity of the vortex pairs relative to the surrounding air. The top of the 'S' indicates a deceleration which is consistent with the flow moving further away from the blockage of the jet apparatus.

4.3. Vortex Spacing.

Figure 4-6 shows the vortex spacing, based on the regions of highest helium concentrations and on the centers of mass fraction for M = 1.066. The center of mass spacing initially rises as the stream of air divides the helium jet into top and bottom halves. Figure 3-1 shows that the tail regions initially form further apart than the core regions do. The cores induce a motion on the tails which bring them closer together. Thus the mass fraction spacing is higher just after the tail regions form, and then decreases slightly eventually reaching a steady-state value. The computations performed by Yang (1991) showed a similar behavior in the mass fraction spacing.

The spacing between the regions of highest helium concentrations has a slightly different character. Even after the formation of well developed core regions, the spacing still appears to increase slowly. This could be an indication that the vortex cores are moving further apart. Another possibility is that the location of the maximum helium concentration is different from the center of vorticity. If the centers of the vortices were further from the center line than the regions of maximum helium concentration, the highest helium concentrations would be strained by the vorticity and mix faster than the helium in the centers of the vortices. Hence, the spacing between the regions of highest helium concentration would increase until the highest helium concentrations would be in the vortex cores.

Figures 4-7 through 4-9 show the vortex spacing for Mach numbers 1.142 at 0.55 atm, 1.5, 2.0. As the Mach number increases the spacing between the vortices also increases. For each of these cases, the center of regions of highest helium concentrations

also move further apart after the formation of well defined cores. The vortex spacing for the Mach 1.14 case with p_1 = 1 atm, as shown in Figure 4-10.

A summary of the velocities of the vortex pairs and the spacing between the cores based on the highest concentrations of helium is shown in table 4-1. The velocity is normalized by the speed of sound ahead of the shock, and the spacing is normalized by the initial half height diameter.

Table 4-1. Summary of the Vortex Velocities and Spacing.

Mach #	U_v / a_1	$\bar{y}_v / d$
1.066	0.020	0.86
1.142 (0.55 atm)	0.039	0.90
1.50	0.068	1.07
2.00	0.070	1.26

The velocity U_v is the slope of the straight line fit through the position measurements, and represents an average velocity. To be consistent with the average velocity measurement, the vortex center spacing represents the average spacing over the range of times used in the velocity fit.

4.4. Comparison with Computational Results.

The conditions of the experiments were similar to but not exactly the same as the conditions of the computations performed by Yang (1991). Estimates of the computational velocities and spacing for the exact conditions of the experiments were made by interpolating between the Mach numbers and density ratio's in the computations and correcting for the differences in channel spacing and jet interface thicknesses. Table 4-2 shows the comparison of the experiments with the computations.

Table 4-2. Comparison of the Experiments with the Computations of Yang.

Mach #	U_{cmf}/a_1 exp.	$\bar{y}_{cmf}/d$ exp.	U_{cmf}/a_1 comp.	y_{cmf}/d comp.
1.066	0.0175	0.92	0.019	0.85
1.142	0.035	0.92	0.037	0.90
1.50	0.052	1.11	0.055	1.17
2.00	0.063	1.3	0.059	1.19

The velocities and spacing listed are based on centers of mass fraction. The experimental results are found to be consistent with the computational results.

An estimate of the circulation for the experiments may be made using the result for a point vortex pair: $\Gamma = 2\pi U_v y_v$. This estimate does not include the effect of the vortex core size which Yang (1991) and Pierrehumbert (1980) have shown reduces the total induced velocity for the same total circulation. If the distribution of vorticity in the cores in the experiments is similar for the different Mach number cases, the estimate of the circulation might scale with the actual circulation and the values of $\Gamma/\Gamma_{1.066}$ for the estimate might match the actual values of $\Gamma/\Gamma_{1.066}$. Values of $\Gamma/a_1 d$ and $\Gamma/\Gamma_{1.066}$ that are based on the point vortex pair estimate for the experiments, the circulation from the computations by Yang, and the circulation found from the model developed by Yang are given in Table 4-3.

Table 4-3. Comparison of the Circulation From the Experiments, the Computations of Yang (1991), and the Model of Yang.

Mach #	Experiments		Computations		Model	
	$\frac{\Gamma}{a_1 d}$	$\frac{\Gamma}{\Gamma_{M=1.066}}$	$\frac{\Gamma}{a_1 d}$	$\frac{\Gamma}{\Gamma_{M=1.066}}$	$\frac{\Gamma}{a_1 d}$	$\frac{\Gamma}{\Gamma_{M=1.066}}$
1.066	0.111	1.0	0.116	1.0	0.119	1.0
1.142	0.218	1.97	0.224	1.93	0.234	1.96
1.50	0.455	4.11	0.391	3.39	0.494	4.14
2.0	0.554	5.00	0.487	4.21	0.621	5.20

The values listed in Table 4-3 for the computations are estimates for the exact experimental conditions that were made by interpolating between the Mach numbers and density ratio's in the computations and correcting for the differences in channel spacing and jet interface thicknesses. The agreement in the values of $\Gamma/a_1 d$ and $\Gamma/\Gamma_{1.066}$ for the experiments, the computations, and the model is very good considering the sensitivity of the velocity measurements to small errors and the variation in the spacing between the cores in Figures 4-6 to 4-10. The experimental estimates of $\Gamma/\Gamma_{1.066}$ seem to have better agreement with the circulation model than with the computational results which is a little surprising given the approximate nature of the similarity argument used by Yang (1991). This agreement shows the product of the velocity of the vortex pair and the spacing between the cores scales with the circulation model developed by Yang.

4.5. Other Properties of the Vortex Pairs.

Shown in Table 4-4 are values of the Reynolds number of the vortex pairs defined as Γ/ν and values of U_v/a_2 which give an indication of effect compressibility on the vortex pair.

Table 4-4.

Mach #/P_1(atm)	Γ/ν_2	U/a_2
1.07/1.0	2800	0.02
1.14/1.0	6060	0.037
1.14/0.55	3990	0.037
1.50/0.23	4900	0.058
2.00/0.08	2450	0.054

Here, ν_2 and a_2 are the kinematic viscosity and speed of sound after the shock interaction. Although the values of Γ/ν_2 are as high as 6000, the vortex pairs appear laminar in the pictures of the cross sections viewed by planar Rayleigh scattering, and in the shadowgraph photographs of the side views. It should be noted that the stratification of the light helium in the centers of the vortex cores and the heavy air outside the cores helps to stabilize the flow. Yang (1991) used the results of Moore and Pullin (1987) to show that the velocity of the vortex pairs is not significantly affected by compressibility for values of U_v/a_2 below 0.06 .

CHAPTER 5

MIXING

5.1. Considerations for Quantitative Analysis.

5.1.1. Dependence of the Signal on Pressure and Temperature

The objective of the quantitative analysis is to find the molar concentration field of helium from the light intensity field in the pictures taken with the CCD camera. The intensity of light measured by a pixel on the camera is related to the concentration field through:

$$\text{Signal} \sim n\,(\alpha_{air}\chi_{air}+\alpha_{He}\chi_{He})$$

where n is the number density of molecules, χ is the mole fraction, and α is the scattering cross section of the molecules. Since the number density is a function of pressure and temperature, the signal also depends on the pressure and temperature.

Computations by Yang (1991) show that the largest pressure variation throughout the structure after the formation of the vortex pair is about 1% for a Mach 1.1 shock, and about 5% for a Mach 2.0 shock, which indicates that the pressure variation is about 1% for the M = 1.066 and 1.142 cases, and between 1% and 5% for the M = 1.50 case. Since it was not possible to account for these differences, the quantitative analysis assumes the pressure is constant in each picture. Furthermore, because the specific heat ratio is different between helium and air, the temperature of the helium after the shock will be higher than the temperature of the air. For example, for an isentropic compression with the same pressure ratio as a Mach 1.1 shock, the number density in Helium will be 2.3% lower than the number density in air. A first order correction for this error was made by assuming $n \sim (p_2/p_1)^{1/\gamma}$, where p_2/p_1 is the pressure ratio calculated from the normal shock

relations for a perfect gas, and where γ (the specific heat ratio) was evaluated locally in the picture as a function of the mole fraction of helium.

5.1.2. Resolution Limits of the Camera and Laser

The molar concentrations measured by the pixels of the CCD camera represent average values of the concentration over a small volume of fluid and over a short time. The volume of fluid was contained in a parallelepiped; the cross section of the parallelepiped was the square area defined by the area viewed by an individual camera pixel (0.06mm by 0.06 mm in the test section), and the length was the thickness of the laser sheet (1.5 mm). If the flow was purely two-dimensional the thickness of the laser sheet would not be very important. However, the shadowgraph pictures of the jet side view indicate that for the case where M = 1.14, and p_1 = 1 atm (the case with the smallest concentration scales) the jet is inclined at a 5 degree angle relative to the normal of the laser sheet. This implies that averaging perpendicular to the plane of the laser sheet over the sheet thickness is equivalent to averaging over a distance of (1.5mm)tan(5^o) or about two pixels in the plane of the laser sheet.

The length of time over which the average was taken was defined by the laser pulse length which was about 700 nsec. During this time, fluid elements of air behind shocks which have Mach numbers of 1.07, 1.14, and 1.50, will move respectively 0.43 pixels, 0.90 pixels and 1.9 pixels.

5.1.3. Estimate of the Scales of Interest

In order for the volumetric average of helium concentrations in this laminar flow to accurately represent the molecular concentration, the length scales over which changes in concentrations occur must be larger than the lengths of the averaging. Diffusion acts to increase the concentration length scale while the straining imposed by the vorticity generated by the shock shortens the length scale. This process is similar to that which

occurs in the diffusion layers of a small flame element in a straining flow where it is found for fast chemical kinetics, a constant strain rate, and $\varepsilon t >> 1$ that the diffusion layer thickness for the fuel and oxidant are each about $(2\mathcal{D}/\varepsilon)^{1/2}$. Here $\mathcal{D}$ is the binary diffusion coefficient, and ε is the strain rate.

Because the strain rates are caused by the vorticity generated during the shock interaction it is reasonable to expect the strain rates in the flow to scale with Γ/d^2 and for the concentration length scales to scale with $\mathcal{D}/\Gamma$. For gas, the Schmidt number, $\nu/\mathcal{D}$ is about one and $\mathcal{D}/\Gamma \sim \nu/\Gamma$. Since the value of ν/Γ (see Table 4-4) is the smallest for the case where M = 1.14 and p_1 = 1 atm, it is expected that this case will have the smallest concentration length scales of all the cases studied. For this case, in two pictures with times close together strain rates were estimated by measuring the length of an element of fluid in the strand of fluid which joins the top vortex and bottom vortex, and the length of an element of fluid in the core regions. The values $(1/L)(\Delta L/\Delta T)$ were calculated for both elements to be about 5000 sec^{-1}. These rates should be the highest strain rates in the flow and imply that the smallest diffusion scales should be about $2(2\mathcal{D}/\varepsilon)^{1/2}$ = 7 pixels. Since the averaging is over about 2 pixels, the measurements should accurately represent the helium concentrations.

5.1.4. Noise Considerations

The ratio of (scattering signal):(rms of signal) was found to be 30:1 for each pixel for pure air at atmospheric pressure. The noise in the signal is mostly due to shot noise, which results from the finite number of photons striking a pixel. The initial pressure before the shock wave had to be lowered for the higher Mach number experiments to keep the test section pressure behind the reflected shock within the safe limits of the structure. Since the number density of molecules was lower, the scattering signal was also reduced, and the ratio for pure air of the (signal):(rms signal) decreased. As mentioned earlier, this decrease caused the pictures for the higher Mach number cases to

be more grainy than the pictures for the lower Mach number cases. Table 5-1 shows the ratio for the different cases.

Table 5-1

Case	(Air Signal)/(Rms of Signal)
M = 1.07, 1.14 p1 = 1 atm	30
M = 1.14 p1 = 0.55 atm	20
M = 1.50 p1 = 0.23 atm	15
M = 2.00 p1 = 0.08 atm	8

5.2. Definition of the Mass Distribution Function

The objective of the study is to measure the mixing between helium and air. In order to facilitate this a mass distribution function for each picture is defined which shows how the helium is distributed in different molar concentrations of helium for that picture. The mass distribution function, $m_{He}(\chi_{He})$ is defined such that:

$$\frac{(\#\text{ of moles in the mole fraction range } \chi^0_{He} \text{ to } \chi^0_{He} + d\chi_{He})}{(\text{total \# of moles of helium})} = m_{He}(\chi^0_{He})d\chi_{He},$$

where χ_{He} is the mole fraction of helium and χ^0_{He} is a particular value of the mole fraction of helium. Formally the definition is:

$$m_{He}(\chi_{He}) = \frac{1}{M_{tot}}\frac{dM_{tot}}{d\chi_{He}},$$

where M_{tot} is the total number of moles of helium in the cross section. The mass distribution function has the property that:

$$1 = \int_0^1 m_{He}(\chi_{He})d\chi_{He} \ .$$

If the initial jet was a top hat profile of pure helium, the mass distribution function would be a delta function at $\chi_{He} = 1$. On the other hand, if an initial finite mass of

helium were allowed to mix uniformly with a very large amount of air, the distribution would approach a delta function at $\chi_{He} = 0^+$. For combustion between hydrogen and air the goal is to have as much mass as possible near the stoichiometric ratio of $\chi_{H_2} = 0.3$.

For an individual picture, a box is drawn around the region which contains the helium. The mole fraction range from 0 to 1 is divided up into a finite number of bins. The number of bins used was set roughly equal to the dynamic range of the picture as defined by the ratio of (signal of pure air)/(rms of the signal). For each pixel in the box the mole fraction of helium, and mass of helium were calculated. The mass of helium was added to the bin appropriate for the measured mole fraction. This results in the relation:

$$m_{He} \propto A(\chi^0_{He})\, n\, \chi^0_{He},$$

where $A(\chi^0_{He}) \equiv$ area of fluid with concentrations in the range χ^0_{He} to $\chi^0_{He} + d\chi_{He}$, and n is the number density of molecules. This shows that the mass distribution function has an area weighting and concentration weighting. Nominally, the distribution would not be affected by the size of the box used in the calculation, as long as the box contained all of the helium mass. However, because there is noise in the signal, the distribution in the lowest mole fraction ranges will be affected by the size of the box. In addition, the pictures in general did not view all of the helium mass, but missed some of the mass in the lowest concentrations of helium; details are given in Appendix E.

The cross sections of the jets investigated did not have pure helium in the center of the jet. Air diffused into the center and premixed with the helium. To take this into account, the mole fractions of helium are converted to mole fractions of jet fluid χ_{jet}, by dividing the mole fractions of helium by the maximum helium mole fraction in the initial jet. Thus, $\chi_{jet} = 1$ represents the initial jet centerline mixture of air and helium at the cross section studied.

A typical experimentally measured initial jet distribution is shown in Figure 5-1. The mass distribution function has the value 0, at $\chi_{jet} = 0$, because of the mole fraction weighting. Although on average pure air will be represented by $\chi_{jet} = 0$, the noise in the signal causes some pixels in regions with pure air to be brighter than average and some darker than average. The pure air pixels which are brighter than average result in negative concentrations and masses of jet fluid. The darker than average pure air signals add to the positive but low concentrations of jet fluid. In addition, noise in the signal near $\chi_{jet} = 1$ allows mole fraction values larger than 1.

In the mole fraction range from 0 to 0.2, the distribution rises sharply. Part of this increase is produced by the noise, but a larger part represents the large mass of helium which is contained in this range. In the mole fraction range from 0.2 to 0.4 the distribution decreases. This change indicates that the area weighting is decreasing faster that the mole fraction weighting. The distribution is roughly level for mole fractions between 0.4 and 0.9, and this indicates a balance between the decrease in area and increase in mole fraction.

In addition to drawing a box around the entire region containing the helium, boxes were drawn around the tail regions, and the vortex core regions as in Figure 5-2. This allows the contribution to the mixing in the core and tail regions to be studied separately. The representation of the distribution in the tails and cores depends on the size of the boxes drawn.

Figure 5-3 compares the mass distribution for a helium jet at 1 atm at two different cross sections, which are, respectively, 4.9 and 5.7 jet exit diameters above the jet exit. When taking a picture of the initial jet distribution, light scattering off of the jet apparatus the prevented the entire cross section from being viewed. As shown in Figure 3-2a, the left most part of the jet cross section is cut off, and the mass distribution function for the cross section is not accurate for the lowest concentrations of helium. If the jet were perfectly symmetric, a correction could be made. Since the jets were slightly

asymmetric, and only the lowest concentrations in the initial jet distribution were affected, the correction was not made, and the curves in Figure 5-3 are only plotted for values which are unaffected.

Because the average exit velocity of the jet was 130 cm/sec, an element of fluid takes 5 milliseconds (or $a_1t/r_0 = 350$) to travel between the two cross sections. The small difference between the two curves in Figure 5-3 shows that little mixing occurs in the jet cross section over the 5 milliseconds.

5.3. Mass Distributions for Mach numbers 1.066, 1.142, and 1.50.

The mass distribution function for the whole picture, the tail regions, and the core regions is shown in Figure 5-4 for M = 1.066 and $a_1t/r_0 = 156$. There is no pure jet fluid left at this time. On the right side of the Figure, the mass distribution function increases (with decreasing mole fraction of jet fluid) from zero. The first rise with decreasing mole fraction represents the maximum concentrations of jet fluid left in the cross section. The curves for the whole picture and core regions are identical at the highest mole fractions. This indicates that the cores contain the regions with the highest helium concentrations. As the mole fraction continues to decrease, the curves separate as mass appears in the tail regions. The tails are shown to add a second distinct rise to the curve for the whole picture, and help to form a broad peak in the curve between mole fractions of 0.75 and 0.4. The second rapid rise represents the maximum jet fluid concentrations in the tails.

Figure 5-5 shows the total mass distribution curves for the initial jet and at three times after the shock interaction. When comparing the initial jet distribution with the first time shown of $a_1t/r_0 = 85$, it is seen that the major effect of the shock is to move mass from the highest concentrations into a broad peak in the curve for $a_1t/r_0 = 85$ which occurs in the concentration range 0.65 to 0.85. The distribution at $a_1t/r_0 = 85$ below a

mole fraction value of 0.5 is not much different than the initial jet distribution. Most of the mass that was above a mole fraction of 0.5 is still above 0.5.

For each of the times shown, the first slope from the right which brings the mass distribution function up from zero represents the maximum concentrations of jet fluid found in the vortex cores and in the entire picture. As time increases, this curve shifts to the left as more air is mixed in the center of the cores. For each time, there is a second slope from the right which represents the maximum jet fluid concentrations in the tails. The fact that the second slope from the right, shifts to the left faster than the first slope is an indication that the tails are being strained and mixed faster than the cores. The difference in the mass distribution function for the initial jet and $a_1 t/r_0 = 204$, which corresponds to about 2.0 milliseconds, can be compared to the difference between the two curves in Figure 5-3. Much more mixing occurred in the cross section of the laser sheet after the shock interaction over two milliseconds, than occurred as a cross section of the jet moved from h/d = 4.9 to 5.7 over 5 milliseconds without a shock interaction.

Figure 5-6 shows the total mass distribution function and the contributions from the tails and vortex cores for M = 1.142 and p_1 = 0.55 atm. In Chapter 3 it was noted that the tail regions were smaller in the M = 1.142 case than in the M = 1.066 case. Figure 5-6 also indicates that the contribution of the tails is much smaller here. The second slope from the right which represents the tails is much less pronounced. Figure 5-7 shows the total mass distribution for three different times. In this case the broad peak which forms is much less prominent than in the 1.066 case. At $a_1 t/r_0 = 28$, a more uniform shift of high concentrations to lower concentrations seems to have occurred than in the 1.066 case. Mass which was in concentrations above 0.5 has shifted below mole fractions of 0.55.

Figure 5-8 shows the mass distribution for the Mach 1.5 shock wave. The mass distribution in the tails is negligible here. Substantial mixing appears to have occurred even at the first time shown of $a_1 t/r_0 = 6$.

5.4. Mass of Jet Fluid in Regions at Least 30% and 50% Jet Fluid.

Another measure of the mixing is the mass of jet fluid contained in regions where the mole fraction of jet fluid is greater than 30% ($M_{30\%}$) or greater than 50% ($M_{50\%}$). These values are defined by the integrals:

$$M_{30\%} = \int_{0.3}^{1.0} m_{jet}(\chi_{jet})d\chi_{jet} \quad , \quad \text{or} \quad M_{50\%} = \int_{0.5}^{1.0} m_{jet}(\chi_{jet})d\chi_{jet} \quad .$$

One value each of $M_{30\%}$ and $M_{50\%}$ is found for each experiment performed and curves of $M_{30\%}$ and $M_{50\%}$ are generated for each series of experiments. Figure 5-9 shows $M_{30\%}$ and $M_{50\%}$ for M = 1.066 with the cross section taken 5.7 diameters away from the jet exit. The mass distribution functions showed (see Figure 5-5) that for early times the effect of the shock was to move the highest concentrations in the initial jet cross section, into a broad peak. Since the broad peak was located above the 0.5 mole fraction level, there is initially little change in $M_{30\%}$ and $M_{50\%}$. As the broad peak shifts to lower concentrations the curves for $M_{30\%}$ and $M_{50\%}$ decrease, reflecting the mixing which occurs.

Figure 5-10 shows $M_{50\%}$ for Mach numbers 1.066, 1.142, and 1.50 vs. a_1t/r_0. In order to emphasize the effect of the shock, the curves have been normalized by the initial values of $M_{50\%}$ in the jet cross sections before the shock interaction. Figure 5-10 shows that the mixing occurs much faster for the higher Mach numbers. Given the fact that the fuel may be in the engine for maximum times in the range $80 < a_1t/r_0 < 160$, the mixing is found to be rapid enough to be of interest for supersonic combustion for shock Mach numbers in the range 1.15 to 1.50. Figure 5-11 plots the same information with the time normalized by (t/τ) where τ is the characteristic time:

$$\tau = \frac{r_0}{a_1}\left(\frac{M}{M^2-1}\right)\left(\frac{1+\frac{\rho_1}{\rho_h}}{1-\frac{\rho_1}{\rho_h}}\right)$$

This time scale provides a rough collapse of the mixing data. The time $(t/\tau) = 5$, is roughly the time it takes for the stream of air to move all the way through the initially circular jet cross section. As mentioned above $M_{50\%}$ does not change much initially for the M = 1.066 case, and it decreases only after $(t/\tau) = 5$. For the Mach 1.14 cases and the Mach 1.50 case, $M_{50\%}$ decreases almost immediately as the stream of air moves through the cross section before $(t/\tau) = 5$. This initial decrease is larger for the M = 1.50 case than for the M = 1.14 case. This indicates that as the shock Mach number increases, more mixing occurs initially as the stream of air moves through the cross section.

At later times, however, there is more mixing in the M = 1.066 case as the tails are strained by the vortex pair. The large tails for the lower Mach number allow $M_{50\%}$ for the M = 1.066 case to decrease below the values for the M = 1.14 cases, to about the same level as the M = 1.50 case. Figure 5-12 shows $M_{30\%}$ for the three Mach numbers. Overall, the behavior is similar to $M_{50\%}$.

5.5. The Effect of the Reflected Shock.

In Chapter 3 it was described how the reflected shock tore part of the vortex cores away causing additional straining and deformation. Figure 5-13 compares two mass distribution functions at similar times; one developed after a reflected shock interaction $a_1t/r_0 = 110$, while the other developed without a reflected shock interaction. The additional mixing caused by the reflected shock is shown by the shift to the left in the mass distribution from the case with no reflected shock to the case with a reflected shock. The additional enhancement in mixing is also shown in Figure 5-14 which gives the mass in regions greater than 30% and 50% for the Mach 1.066 case with and without

the reflected shock. The reflected shock also enhances the mixing for M = 1.142 as shown in Figure 5-14.

5.6. Summary of the Mixing Results

To summarize the amount of mixing which occurs after the initial and reflected shock interactions, values of $M_{50\%}$ for the initial jet in each case and for the last picture in each case are given in Table 5-2 along with values of $M_{50\%}/(M_{50\%})_{initial}$.

Table 5-2

Case	$(a_1t/r_0)_{final}$	$(M_{50\%})_{initial}$	$(M_{50\%})_{final}$	$M_{50\%}/(M_{50\%})_{initial}$
Initial Jet as Cross-Section Moves from h/D=4.9 to 5.7 (No Shocks)	350	0.47	0.45	0.96
M=1.066 (One Shock)	250	0.45	0.20	0.45
M=1.066 with Reflected Shock	202	0.45	0.12	0.27
M=1.146 (One Shock) P=1 atm	74	0.46	0.30	0.66
M=1.142 (One Shock) P=0.55 atm	107	.45	0.27	.59
M=1.142 (with Reflected Shock) P=0.55 atm	120	.45	0.17	.38
M=1.50 (One Shock)	26	0.39	0.20	0.53

As shown in the first row of Table 5-2, there is little difference between $M_{50\%}$ at h/D = 4.9 and h/D =5.7, which indicates that without a shock interaction little mixing occurs over a time interval of $a_1t/r_0 = 350$. In contrast, substantial mixing occurs over

shorter time intervals with one or two shock interactions as shown in the rest of Table 5-2. A comparison of the values of a_1t/r_0 in Table 5-2 with the estimate of the time available for mixing in a supersonic combustion engine of a_1t/r_0 = 80 to 160 indicates that the mixing which occurs after a shock interaction happens fast enough (especially for shock Mach numbers above 1.15) to be of interest to the designers of supersonic combustion engines.

CHAPTER 6

CONCLUSIONS

Planar Rayleigh scattering was used to study the enhancement in molecular mixing after a shock passes through a laminar jet of helium. Molar concentration fields in two-dimensional cross sections were determined at increasing times after the shock interaction. The shock Mach number was varied, and the effect of a reflected shock was studied.

The mixing in the two-dimensional cross sections of the jet is found to be significantly enhanced after the interaction of a shock wave compared to the mixing which would occur if the cross sections continued to travel in the direction of the jet without a shock interaction. Furthermore, the increased mixing occurs fast enough for shock Mach numbers in the range 1.15 - 1.50 to be useful in supersonic combustors.

For Mach number 1.066, at early times the center of the jet is mixed the most as the stream of air moves through the center of the jet. Little change occurs in the mass distribution function in the helium mole fraction values below 0.5. Relatively large tail lobes form. As the vortex pair pulls ahead of the tail regions, the tails are strained and mixed.

As the Mach number increases, better mixing occurs as the stream of air moves through the center of the jet. As the Mach number increases, changes increase in the mass distribution function in the helium mole fraction values below 0.5 increase. The tail regions contain progressively less helium as the Mach number increases. Less mixing occurs at the later times since less mass is strained in the tails as the vortex pair pulls ahead. A rough collapse of the mixing data occurs when time is normalized with the

velocity of air behind the shock, which is consistent with the development time of Yang (1991).

The reflected shock tears away and strains part of the vortex cores. The tail regions are also additionally strained by the reflected shock. An increase in the enhancement in the mixing occurs. The core regions remaining after the reflected shock are closer together.

As the Mach number increases, the spacing between vortex cores increases. For Mach numbers 1.066 and 1.142, the spacing between the vortex cores based on the centers of mass fraction, rise quickly as the stream of air moves through the center of the jet, but is relatively constant after the formation of well developed core regions. The spacing based on the regions of highest helium concentrations appears to mover further apart throughout the times studied. For M = 1.5 and 2.0 an increase is observed in the spacing based on the center of mass fraction, and the spacing based on the centers of highest helium concentrations increase faster.

The measurement of the vortex pair velocities relative to the surrounding air was found to be very sensitive to small errors in the Mach number. Planar Rayleigh scattering images of the Mach 1.066 shock wave indicated the speed of sound in the lab was 0.5 % higher than the speed estimated from $(\gamma RT)^{1/2}$. The measured velocities and the estimated values of the circulation agree very well with previous computational results, and the product of the velocity of the vortex pair and the spacing between the cores scales with a previously developed circulation model.

REFERENCES

Bohren, B. F., Huffman, D. R. (1983), Absorption and Scattering of Light by Small Particles, John Wiley & Sons, New York.

Born, M., Wolf, W. (1980), Principles of Optics, Pergamon Press, Oxford.

Drummond, J. P., Carpenter, M. H., Reggins, D. W., and Adams, M. S. [1989], "Mixing Enhancement in a Supersonic Combustor," AIAA/ASME/SAE/ASEE 25th Joint Propulsion Conference, AIAA Paper 89-2794.

Eckbreth, A. C. (1988), Laser Diagnostics for Combustion Temperature and Species, Abacus Press, Tunbridge Wells, Kent.

Haas, J. L. [1984], "Interaction of Weak Shock Waves and Discrete Gas Inhomogeneities," Ph.D. Thesis, California Institute of Technology, Pasadena, California.

Haas, F., and Sturtevant, B. [1987], "Interaction of Weak Shock Waves with Cylindrical and Spherical Gas Inhomogeneities," J. Fluid Mechanics, v. 181, pp. 41-76.

Hall, J. L. [1991], "An Experimental Investigation of Structure, Mixing and Combustion in Compressible Turbulent Shear Layers," Ph.D. Thesis, California Institute of Technology, Pasadena, California.

Hendricks, G. J., and Marble, F. E. [1990], "Shock Enhancement of Supersonic Combustion Processes," Jet Propulsion Center Report, California Institute of Technology, Pasadena, California.

Jacobs, J. W. [1992], "Shock-Induced Mixing of a Light-Gas Cylinder," J. Fluid Mechanics, v. 234, pp. 629-649.

Liepmann, H. W., Roshko, A., Coles, D., and Sturtevant, B. [1962], "A 17-inch Diameter Shock Tube for Studies in Rarefied Gas Dynamics," Rev. Sci. Instrum. 33, pp. 625-631.

Marble, F. E., Hendricks, G. J., and Zukoski, E. E. [1987], "Progress Toward Shock Enhancement of Supersonic Combustion Processes," AIAA/SAE/ASME/ASEE 23rd Joint Propulsion Conference, AIAA Paper 87-1880.

Marble, F. E., Zukoski, E. E., Jacobs, J. W., Hendricks, G. J., and Waitz, I. A. [1990], "Shock Enhancement and Control of Hypersonic Mixing and Combustion," AIAA/SAE/ASME/ASEE 26th Joint Propulsion Conference, AIAA Paper 90-1981.

Moore, D. W. and Pullin, D. I. (1987), "The Compressible Vortex Pair," J. Fluid Mechanics, v. 185, pp. 171-204.

Papamoschou, D., and Roshko, A. [1988], "The Compressible Turbulent Shear Layer: An Experimental Study," J. Fluid Mechanics, v. 197, pp. 453-477.

Picone, J. M. and Boris, J. P. [1988], "Vorticity Generation by Shock Propagation Through Bubbles in a Gas," J. Fluid Mechanics, v. 189, pp. 23-51.

Pierrehumbert, R. T. (1980), "A Family of Steady, Translating Vortex Pairs with Distributed Vorticity," J. Fluid Mechanics, v. 99, pp. 129-144.

Rudinger, G. and Somers, L. M. (1960), "Behavior of Small Regions of Different Gases Carried in Accelerated Gas Flows," J. Fluid Mechanics, v. 7, pp. 161-176.

Waitz, I. A. [1991], "An Investigation of Contoured Wall Injectors for Hypervelocity Mixing Augmentation," Ph.D. Thesis, California Institute of Technology, Pasadena, California.

Waitz, I. A., Marble, F. E., and Zukoski, E.E. [1991], "An Investigation of a Contoured Wall Injector for Hypervelocity Mixing Augmentation," AIAA/SAE/ASME/ASEE 27th Joint Propulsion Conference, AIAA Paper 91-2265.

Waitz, I. A., Marble, F. E., and Zukoski, E.E. [1992], "A Systematic Experimental and Computational Investigation of a Class of Contoured Wall Fuel Injectors," 30th Aerospace Sciences Meeting & Exhibit, AIAA Paper 92-0625.

Yang, J. [1991], "An Analytical and Computational Investigation of Shock-Induced Vortical Flows with Applications to Supersonic Combustion," Ph.D. Thesis, California Institute of Technology, Pasadena, California.

APPENDIX A

Sample Combuster Calculation

Starting with the one dimensional energy equation:

$$\frac{u_0^2}{2}+C_pT_0 = \frac{u_1^2}{2}+C_pT_1 = C_pT_{0t}$$

From which it can be shown that:

$$T_{0t} = T_0\left(1+\frac{\gamma-1}{2}M_0^2\right) = T_1\left(1+\frac{\gamma-1}{2}M_1^2\right)$$

and

$$u_0^2\left(1+\frac{2}{(\gamma-1)M_0^2}\right) = u_1^2\left(1+\frac{2}{(\gamma-1)M_1^2}\right)$$

For $M_0 = 15$ and $M_1 = 5$:

$$\frac{u_1^2}{u_0^2} = 0.85\ ,\ \frac{u_1}{u_0} = 0.92\ ,\ \frac{T_1}{T_0} = 7.66\ ,\ \text{and}\ \frac{a_1}{a_0} = \left(\frac{T_1}{T_0}\right)^{\frac{1}{2}} = 2.77;$$

APPENDIX B

Method for Measuring the Mach Number.

Four pressure transducers were installed in the shock tube for incident wave interactions at distances upstream from the shock tube end plate of 6.423 meters (transducer #1), 3.113 meters (#2), 0.8128 meters (#3), and 0.0762 meters (#4). For reflected shock interactions, three transducers were installed 5.813 (#1), 2.503 (#2), and 0.2032 (#3) meters upstream from the end plate. Transducers 1, and 2 were in the main tube before the cookie cutter, while 3 and 4 were in the test sections. The shock velocity was found by dividing the known distance between transducers by the time for the shock wave to pass between the transducers. The Mach number was found by dividing this velocity by the speed of sound estimated from $a = (\gamma RT)^{1/2}$. The Mach number in the main tube was found to differ slightly from the Mach number in the test sections. A plot of M_{34} (Mach number measured between transducers 3 and 4) vs. M_{12} (Mach number measured between transducers 1 and 2) along with a straight line fit is shown in Figure B-1 for shock Mach numbers around 1.07. The experiments shown in Figure B-1 were performed without a jet in the test sections. The primary measurement of Mach number during an experiment with a jet in the test section was made between transducers (#1) and (#2), and the straight line fit was used to find the Mach number in the test section before the interaction with the jet.

Errors in the Mach number measurement are caused by a lack of precision in measuring the time for the shock to travel between transducers, and by errors in the estimate for the speed of sound. The distance between transducers 1 and 2 is five times the distance between transducers 3 and 4, and hence the measurement between 1 and 2 is five times as precise as the measurement between 3 and 4. The scatter about the line in

Figure B-1 is predominately due to the lack of precision in the measurement of M_{12}. The maximum deviation of M_{12} from the straight line fit is 0.022%.

Since the straight line fit is similar to an average, the actual error in the velocity of the shock wave should be on the order of the maximum deviation from the straight line divided by the square root of the number of points in the fit. The error in the measurement of the velocity of the shock wave should be about 0.0078 % for the 1.07 Mach number case. The maximum error in measuring the velocity of the shock was for the Mach 2.0 case, where the error is estimated to be 0.06%.

The speed of sound was estimated by measuring the temperature from a thermometer on the outside of the test sections and using $\gamma = 1.4$, $R = 287.1$. However, three planar Rayleigh scattering experiments without a jet in the test section measured the density ratio across Mach 1.07 shock waves, and Mach numbers based on the density ratios were found. The average Mach number based on the density ratio was 0.5% lower than the Mach number based on the timing between transducers. The maximum deviation from the average was 0.1 %. The difference between the Mach number measurements is attributed to a consistent error in the estimate of the speed of sound, and a 0.5 % correction was made on the speeds of sound estimated from $a = (\gamma RT)^{1/2}$.

APPENDIX C

Calibration of the Rayleigh Scattering Images

The Rayleigh Scattering pictures had to be calibrated to account for the effects of variations in the two-dimensional scattering image that were not related to the air-helium concentration field. The factors which affected the measurement included variations in the laser sheet intensity, background scattering, the response of the camera pixels, and the imaging optics.

The laser sheet energy density had variations normal to its direction of propagation of about ±15% of the mean, and these variations, as well as the total beam energy, could be different each time the laser was fired. Furthermore, the width of laser sheet typically increased slightly with increasing distance from the sheet forming optics which caused a slight decrease in the energy density of the laser sheet in the direction of the light propagation. The increase in the sheet's width over the region viewed by the camera was linear and the virtual origion of the laser sheet did not change each time the laser was fired.

Another factor which had to be accounted for was the background light scattering, which was found to be less than 5% of the scattering signal of air at one atmosphere. Tthe background scattering light was found to be repeatable to within 5% each time the laser was fired.

The response of the CCD camera had to be accounted for. Each camera pixel had a slightly different response to incident light. Furthermore, part of the signal read from the camera was generated by thermal excitation, and by a bias current. This 'dark signal' also varied throughout the pixel array.

The collection optics, which included the window in the test section and the nikon lens, caused small variations in the scattering image. Reasons for these variations included the loss of light in the collection system, and the photometry result (Born and Wolf 1980) that in the image on the camera array the illumination decreases as the fourth power of the cosine of the angle between the principal ray through the image point and the lens axis.

If the camera and laser systems were not changed between the times the laser was fired, the only factor which changed significantly each time the laser was fired, was the laser sheet energy distribution. The effects of all the other factors were very repeatable and could be measured before each experiment. In the scattering experiments with the deforming helium jet, the right of the image always contained pure air and was used to measure the laser sheet energy distribution.

The following procedure was developed to take into account the variations which were not related to air-helium concentration variations. First, just after a picture was taken with the CCD camera, a corresponding 'dark image' was generated by taking a picture with the sutter closed. The dark image represents the part of the signal in the other picture that is due to thermal excitation and the bias current. The signal from each pixel in the dark image was subtracted from the signal of the corresponding pixels in the other image.

Before each experiment the following steps were taken without changing the position of the camera or laser systems. The background scattering was determined by evacuating the shock tube and firing the laser while taking a picture. The virtual origion of the expanding sheet was found by placing three thin brass tubes in the path of the laser sheet, and viewing the scattering image with only air in the test section. Since the light was blocked by the brass tubes, the pictures had three dark stripes. Straight lines were fit to the six transions between light and dark, and were extrapolated back to an intersection point which was the virtual origion of the laser sheet. Then, after removing the tubes

from the laser sheet path, multiple planar Rayleigh scattering pictures were taken which viewed air at one atmosphere pressure. The signal from each pixel in the background scattering image was subtracted from the signal of the corresponding pixel in the scattering images of air at one atmosphere to find 'air response images'. The multiple air response images were averaged to find a single 'average air response image'.

Straight lines, which represented light rays, were drawn from the virtual origion through each pixel on the right edge of the average air response image. These rays extended into the average air response image and every pixel in the image was on one of these rays. An average signal was found for each ray by averaging the signals of pixels along the rays in the 50 colums (there were a total of 576 in the entire picture) closest to the right edge of the image. The signal for every pixel in the average air response image was normalized by the average value for the ray that it was on. Because the distribution of laser sheet energy density normal to the light propagation direction could be different each time the laser was fired, the average ray signal could also be different each time the laser was fired. However, in a picture viewing air only, the signal for each pixel normalized by the average ray signal remained the same (except for the noise associated with the signal) each time the laser was fired. This normalized value represented the combined effects of all of the variations that were not related to the air-helium concentration variations except for the laser sheet distribution.

After an experiment was performed which generated an image of the deforming helium after a shock interaction, a dark image and the background scattering image were subtracted from the deforming helium image. Average ray signals were found over the same columns as in the average air response image, and the signal of every pixel in the experiment's image was normalized by its average ray signal. Finally, the normalized signal in the experiment's image was devided by the coresponding normalized signal from average air response image.

APPENDIX D

Definition of the Center of Mass Fraction.

The center of mass fraction is defined such that.

$$x_{cmf} = \frac{\iint_A x f dA}{\iint_A f dA} \quad \text{and} \quad y_{cmf} = \frac{\iint_A y f dA}{\iint_A f dA},$$

where the spacing is defined such that

$$y_{spacing} = \frac{\iint_A n\chi\sqrt{(y - y_{cm})^2}\, dA}{\iint_A n\chi dA}.$$

Definition of the Center of Regions of Highest Helium Concentrations

The center of highest helium concentrations were calculated separately for the top vortex and the bottom vortex. First a mole fraction of helium χ_l is defined such that

$$0.05 = \int_{\chi_\lambda}^{1} m_{He}(\chi) d\chi,$$

where $m_{He}(c)$ is the mass distribution function defined in chapter 5. χ_l is the mole fraction of helium above which 5 % of the mass of helium is contained. The position based on the highest concentrations of helium (x_h, y_h) for each vortex is

$$y_h = \frac{\iint_A yfn(\chi)\chi n \, dA}{\iint_A fn(\chi)\chi n \, dA},$$

$$x_h = \frac{\iint_A xfn(\chi)\chi n \, dA}{\iint_A fn(\chi)\chi n \, dA}, \quad \text{where } fn(\chi) = \begin{cases} 0, & \chi < \chi_1 \\ 1, & \chi > \chi_1 \end{cases}.$$

APPENDIX E

Total Mass of Helium in the Pictures

The total mass of helium for each picture (normalized by an estimate for the initial total mass) is shown in Figure E-1 for shock Mach numbers of 1.07, 1.14, and 1.50. If the flow were purely two-dimensional, the total mass of helium in the cross section of the laser sheet would be constant as the time after the shock interaction increased. Small decreases in the total mass are observed for M = 1.07 and 1.14, while a small increase is observed for M = 1.50. These trends can be explained (at least in part) by the fact that the field of view of the camera was usually not large enough to see all of the helium present in the plane of the laser sheet. This is illustrated by defining the function:

$$m_x\left(\frac{x}{r_0}\right) = \int_{\left(\frac{y_1}{r_0}\right)}^{\left(\frac{y_2}{r_0}\right)} \frac{n}{n_{\text{pure air}}} \chi_{He}\, d\left(\frac{y}{r_0}\right),$$

which represents the distribution of helium mass along the x axis. Here n is the number density of molecules at a particular place in the picture, $n_{\text{pure air}}$ is the number density of molecules in regions of pure air, χ_{He} is the molar concentration of helium, r_0 is the initial jet radius, y_1 is the y position at the bottom of the picture, and y_2 is the y position at the top of the picture. For example, in Figure E-1 one of the largest decreases in the total mass of helium is for M = 1.066 with $a_1 t/r_0 = 203$. For this case the total mass of helium is only 86% of the initial mass in the plane of the laser sheet and 14% of the mass is

'missing'. The distribution of helium mass along the x axis is shown in Figure E-2 for $M = 1.07$ and $a_1 t/r_0 = 203$. The distribution is not zero at the left edge of the figure, which indicates that additional mass is contained in the cross section of the laser sheet to the left of the camera's field of view. The vortex pair appears to leave behind a 'wake' which contains some helium mass.

Some pictures viewed more of the 'wake' than others. For the same sequence of pictures, each experiment had slightly different Mach numbers, and slightly different vortex pair velocities. Before an experiment, it was not possible to exactly predict the location of the vortex pairs, and more or less of the 'wake' was viewed depending on whether the velocity of the vortex pair in the laboratory reference frame moved slower or faster than expected. However, a trend in the amount of mass viewed developed for Mach numbers 1.07, and 1.14; as the time after the shock interaction increased, the vortex pair which formed pulled further ahead of the tail regions, the horizontal span of the structure and 'wake' increased, and the amount of mass within the camera's field of view on average decreased.

It should be noted that the measurement of the total mass of helium in the plane of the laser sheet is complicated by the fact that a significant amount of the helium mass is contained in regions of low helium concentration which are sensitive to small errors. The scattering technique employed measures air concentrations, and the helium concentrations are found by subtracting the air concentration from 1. In a region of 90% air, a 1% error in the molar air concentration would generate a 10% error in the mass of helium in that region.

To see if the 'wake' may contain all of the missing mass, the area under a curve in Figure E-2 required to contain this mass is calculated, and a straight line is drawn as an extension to the curve in Figure E-2 to a point on the x axis such that the area under the extension contains all of the missing mass. This straight line extension, shown in Figure E-3, extends back a distance equal to about 9 times the half height radius. Figure E-4

shows the mass distribution along the x axis for the initial jet distribution, and for a_1t/r_0 = 67, 164, and 203, at which times the total mass within view of the camera is respectively 99%, 91%, and (as mentioned above) 86% of the estimate for the initial total mass of helium. Because the picture for the initial mass distribution in the jet was cut off on the left, the curve was generated by assuming a symmetry about the jet centerline. The x axis in the figure is the position relative to the surrounding air with 0 being the starting location of the jet centerline. Because the left tail of the initial jet mass distribution is relatively far from the vorticity generated which coalesces into the vortex cores, it is plausible that the 'wake' could extend as far back as the beginning of the left tail (about -6 on the x axis scale). An extension of a straight line to -6 would account for about 95% of the initial total mass for a_1t/r_0 = 203. However, the curves for a_1t/r_0 = 67 and 164 indicate that a more reasonable extension might be to -3 on the x axis scale, which would account for about 90% of the initial mass for a_1t/r_0 = 203. However, (as mentioned above) the calculation of the total mass in the 'wake' region for all of the curves in Figure E-4, is sensitive to small errors in the measured molar air concentration, and it is certainly possible that all of the missing mass is in the part of the 'wake' not viewed by the camera.

The trend of increasing total mass for shock Mach number 1.50 in Figure E-1 may also (at least partly) be explained by mass which initially is not within the view of the camera. In the sequence of pictures for M = 1.50, Figure 3-4, it is observed that the tail regions slightly extend above and below the camera's field of view. The tails receive an induced motion from the vortex pairs which tend to bring more of the tails within the view of the camera. As the time after the shock interaction increases, the mass of helium within the view of the camera increases.

Typically, the only regions affected by the fact that the camera did not view all of the helium in the plane of the laser sheet were regions where the molar helium concentration was less than 5%. The plots in chapter 5 of $M_{30\%}/(M_{30\%})_{initial}$ and $M_{50\%}$

$/(M_{50\%})_{initial}$ were not affected because all of the mass of helium in regions greater than 30% helium were within the view of the camera.

It is also possible that the total mass of helium in the plane of the laser sheet (including the 'wake' region not in the camera's field of view) is less than the estimated initial value. Each picture was generated by a different experiment and the variation in total mass of helium in the cross section before the shock interaction may be as large as ± 5%. This type of variation would not contribute to a trend of increasing or decreasing total mass, but would result in scatter about the initial value. However, straining motions perpendicular to the plain of the laser sheet could cause a trend of increasing or decreasing total mass of helium in the cross section. If straining motions perpendicular to the plane of the laser sheet were present, the values of $M_{30\%}$ and $M_{50\%}$ (which are discussed in chapter 5) could have increases or decreases that are not associated with molecular mixing.

If the total mass of helium in the entire plane of the laser sheet did change (either due to the shot to shot variations or due to straining motions perpendicular to the plane), then the amount of molecular mixing would best be described by plotting:

$$\left(\frac{M_{30\%}}{(M_{30\%})_{initial}}\right)\left(\frac{(M_{tot})_{initial}}{M_{tot}}\right) \text{ and } \left(\frac{M_{50\%}}{(M_{50\%})_{initial}}\right)\left(\frac{(M_{tot})_{initial}}{M_{tot}}\right),$$

instead of $M_{30\%}/(M_{30\%})_{initial}$ and $M_{50\%}/(M_{50\%})_{initial}$ which were plotted in chapter 5. Because of the uncertainty in the total mass calculation, this type of correction was not made. However, given the fact that not all of the helium was viewed by the camera, this correction (at most) would not be greater than 10%, and would not change the character of the plots in chapter 5 or change the conclusion that significant mixing occurs after the shock interactions.

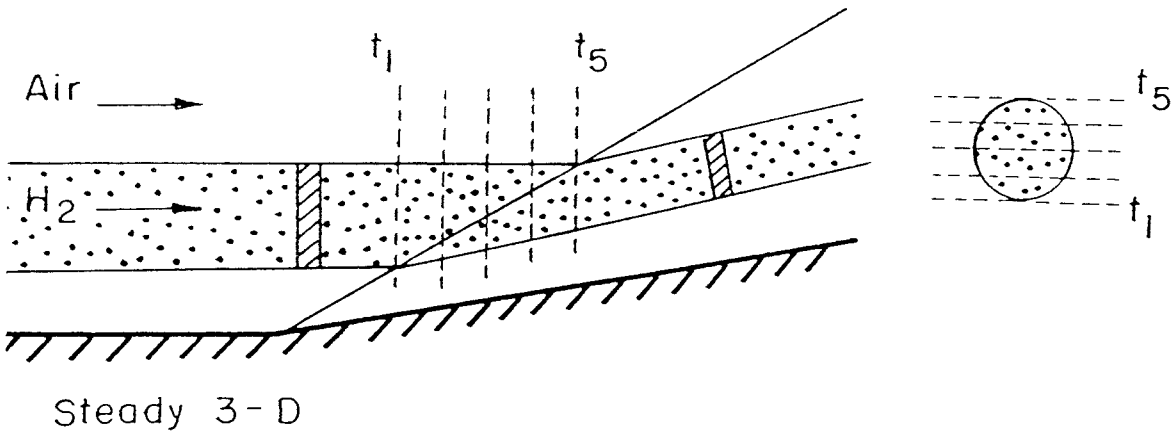

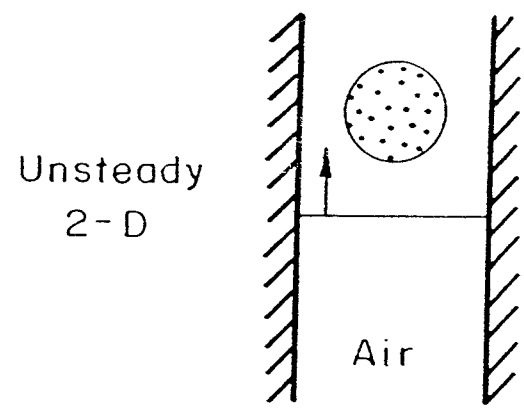

Figure 1-1. Comparison of 3-D Steady and 2-D Unsteady Flows.

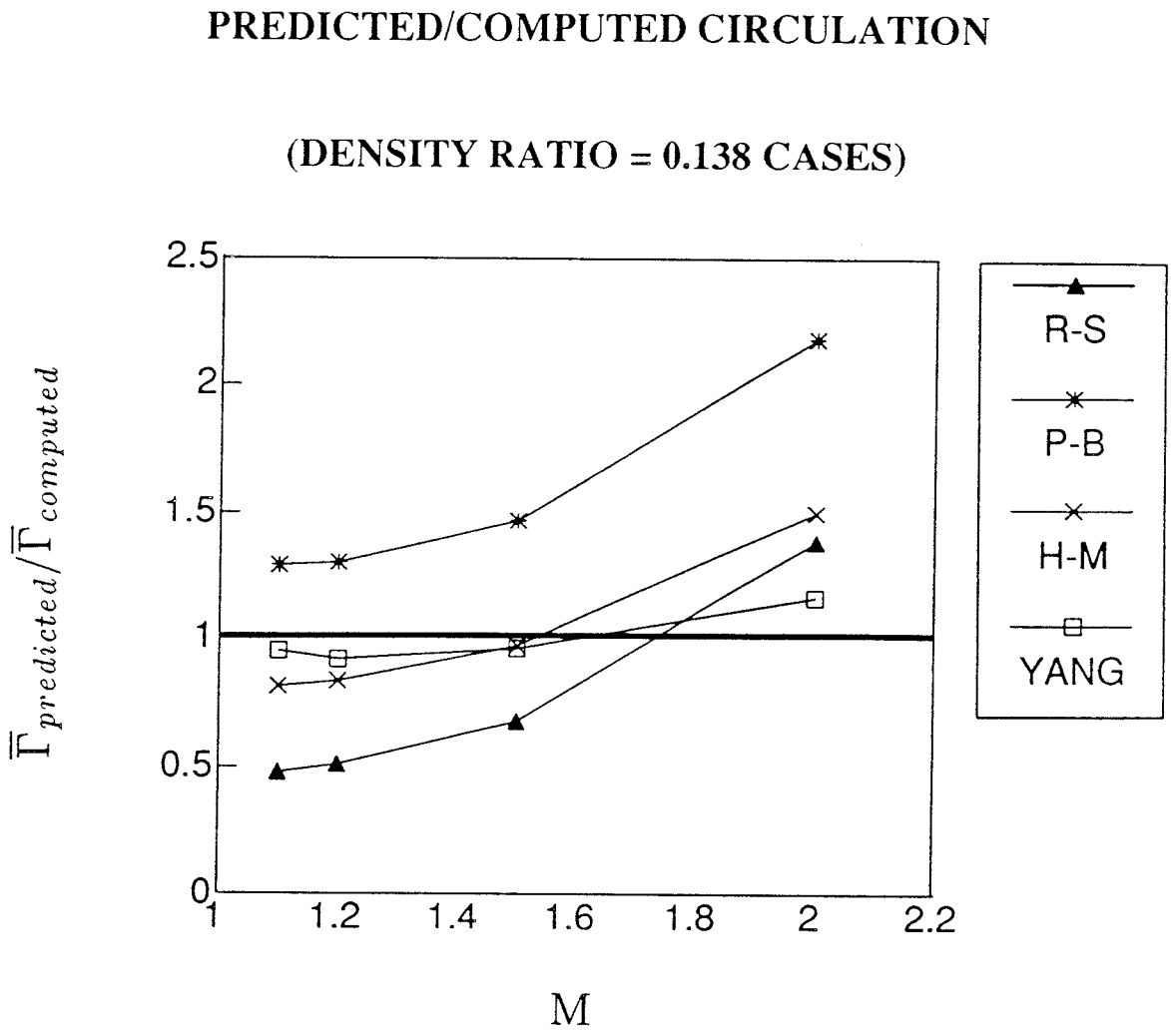

Figure 1-2. Comparison of Circulation Models with Computational Results for a Density Ratio of 0.138 (From Yang 1991).

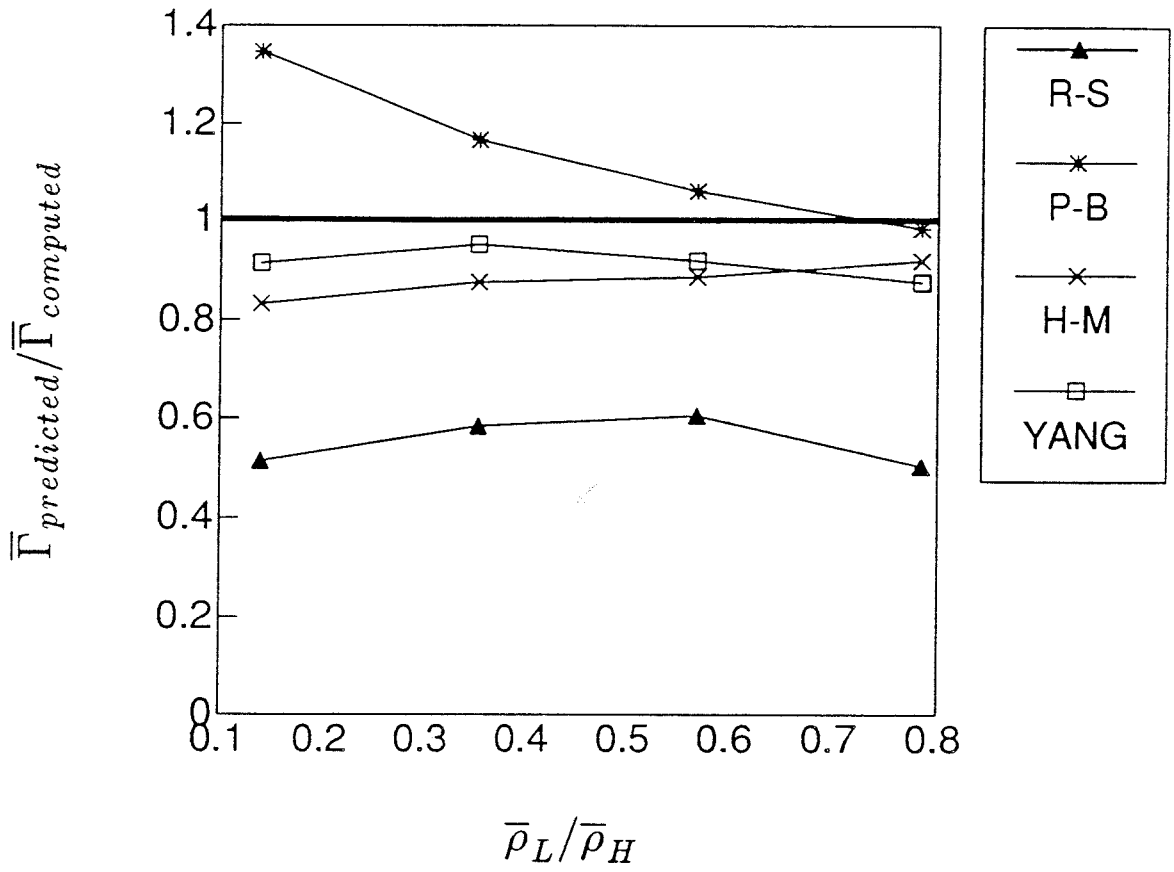

Figure 1-3. Comparison of Circulation Models with Computational Results For Mach Number of 1.1 (From Yang 1991).

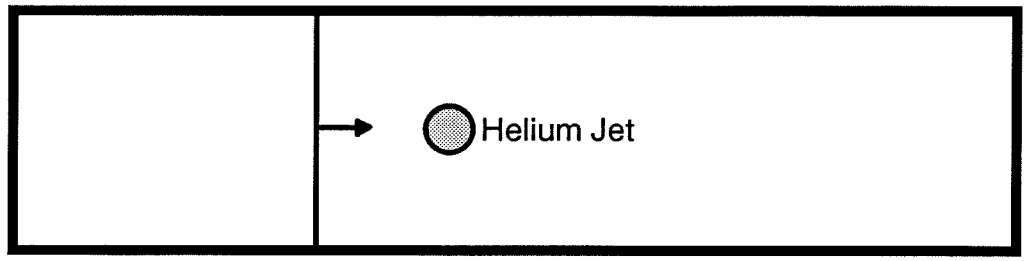

a)

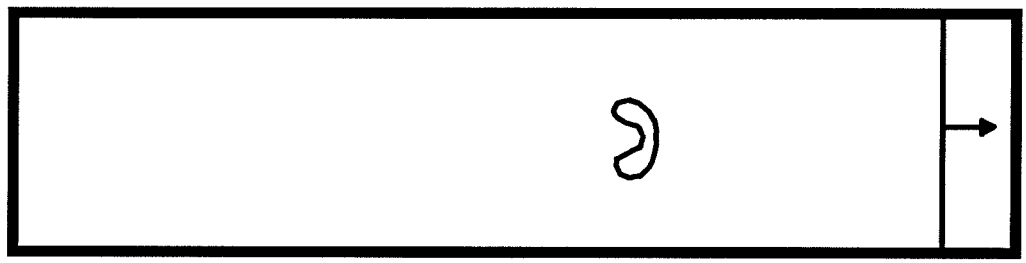

b)

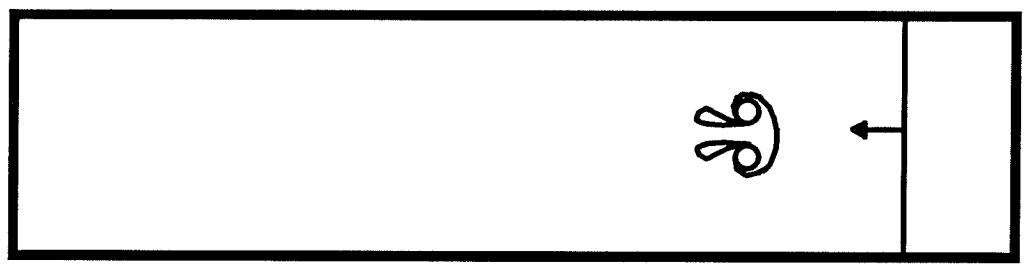

c)

Figure 1-4. Description of the Experiments. a) Helium jet flowing out of page, shock traveling left to right, b) helium jet deforming, shock continues down the tube, c) a vortex pair forms, shock reflects off the end, travels back right to left.

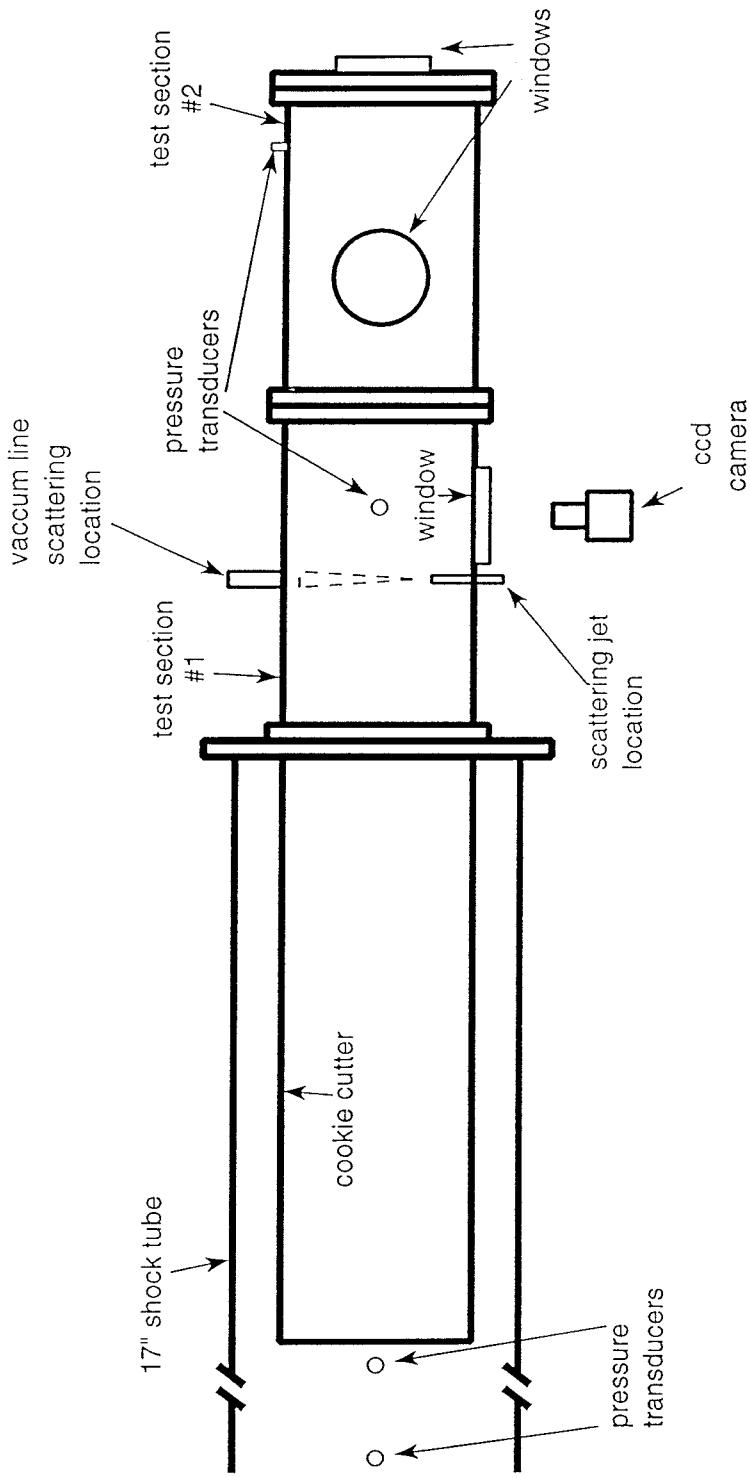

Figure 2-1. The Side View of the 17" Shock Tube.

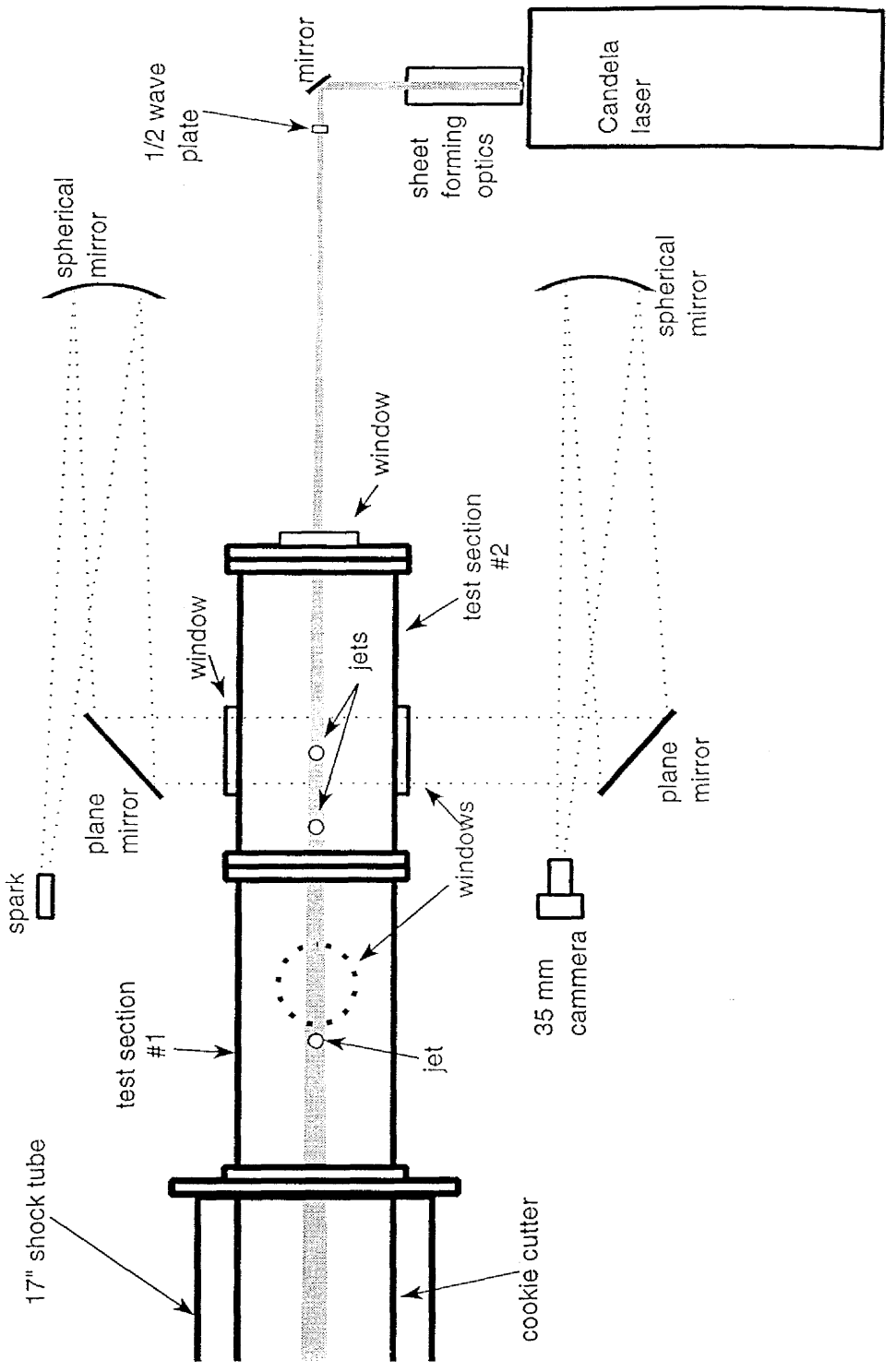

Figure 2-2. The Top View of the 17" Shock Tube.

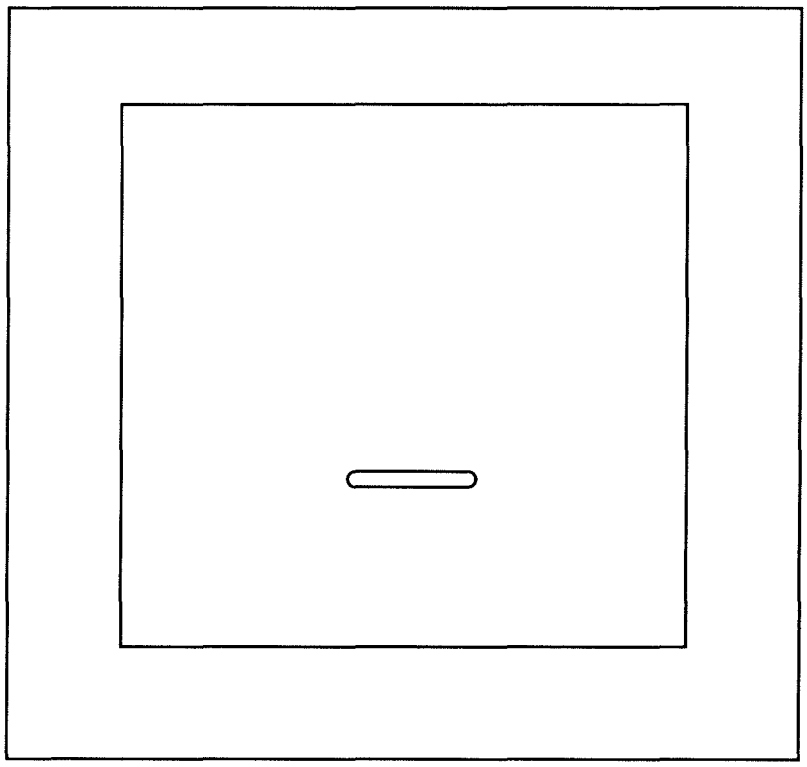

a)

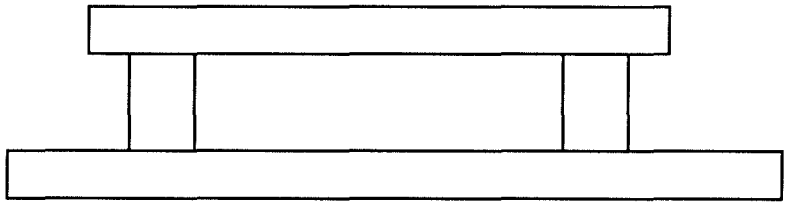

b)

Figure 2-3. The End Plate For The Reflected Mach 2.0 Experiments. a) Top View, b) Side View.

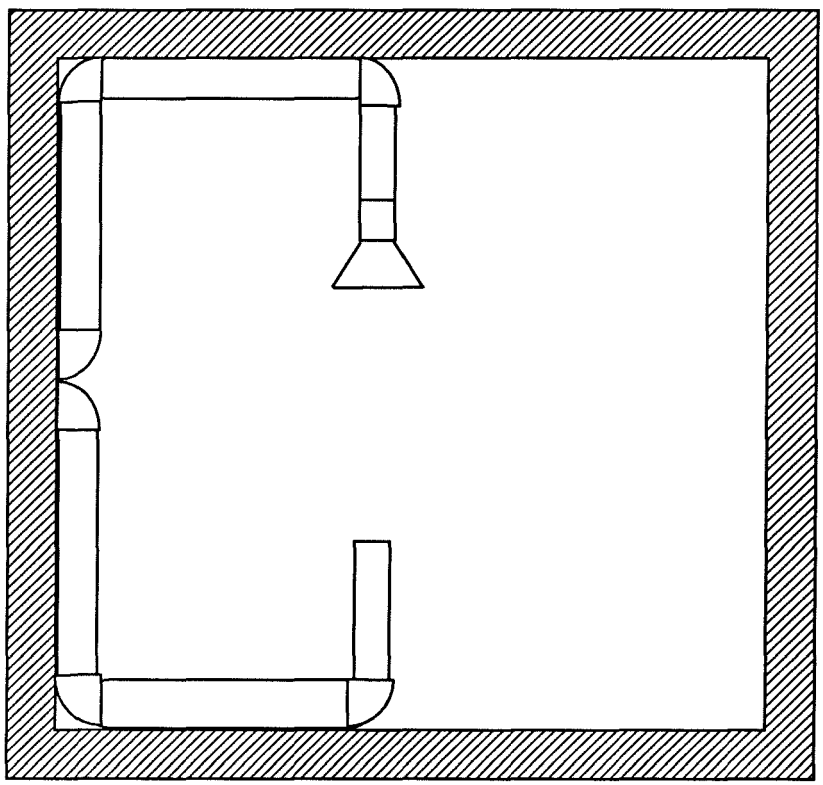

Figure 2-4. The First Jet Apparatus Used.

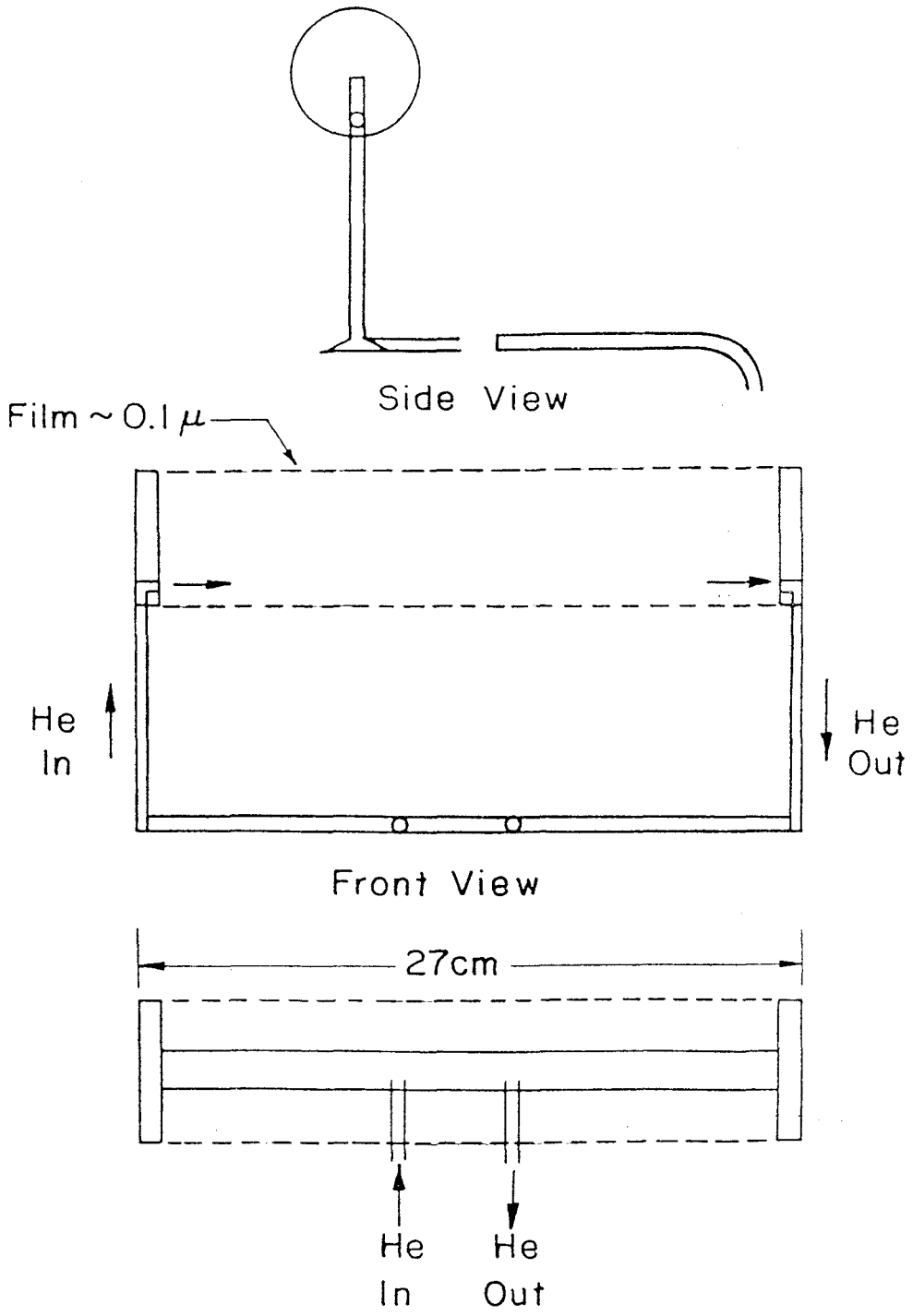

Figure 2-5. The Membrane Holder.

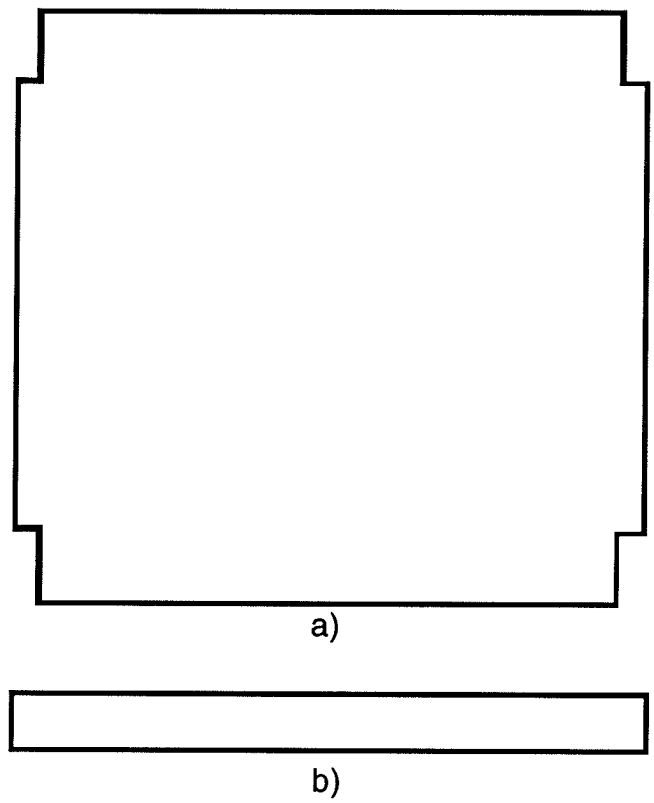

Figure 2-6. The Membrane Plate. a) Top View, b) Side View.

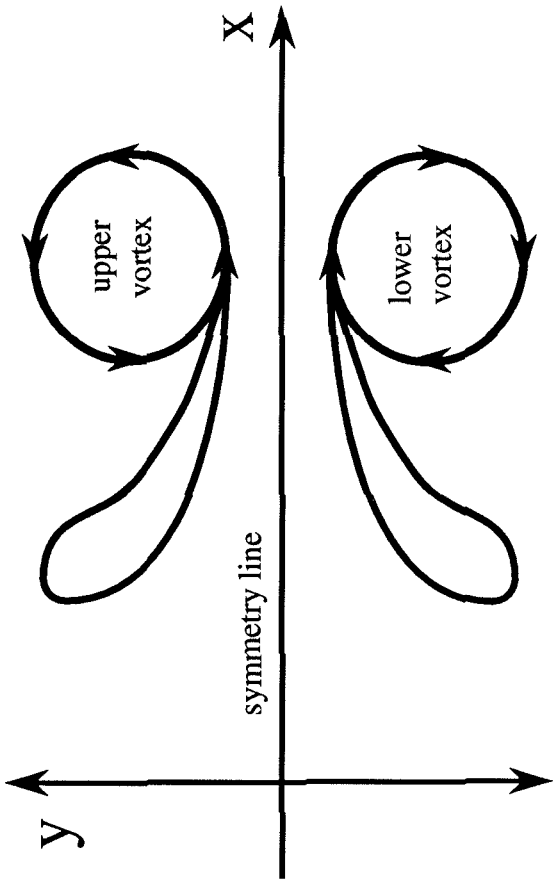

Figure 3-1. Definition of the Conventions Used To Describe the Vortex Pair Structure.

Figure 3-2. Rayleigh Scattering Images for M = 1.066. Without a Reflected Shock (a) a_1t/r_0 = 0, (b) 23, (c) 67, (d) 111, (e) 165, (f) 182, (g) 205, (h) 254, With a Reflected Shock at a_1t/r_0 = 110, (i) 135, (j) 157, (k) 180, (l) 245.

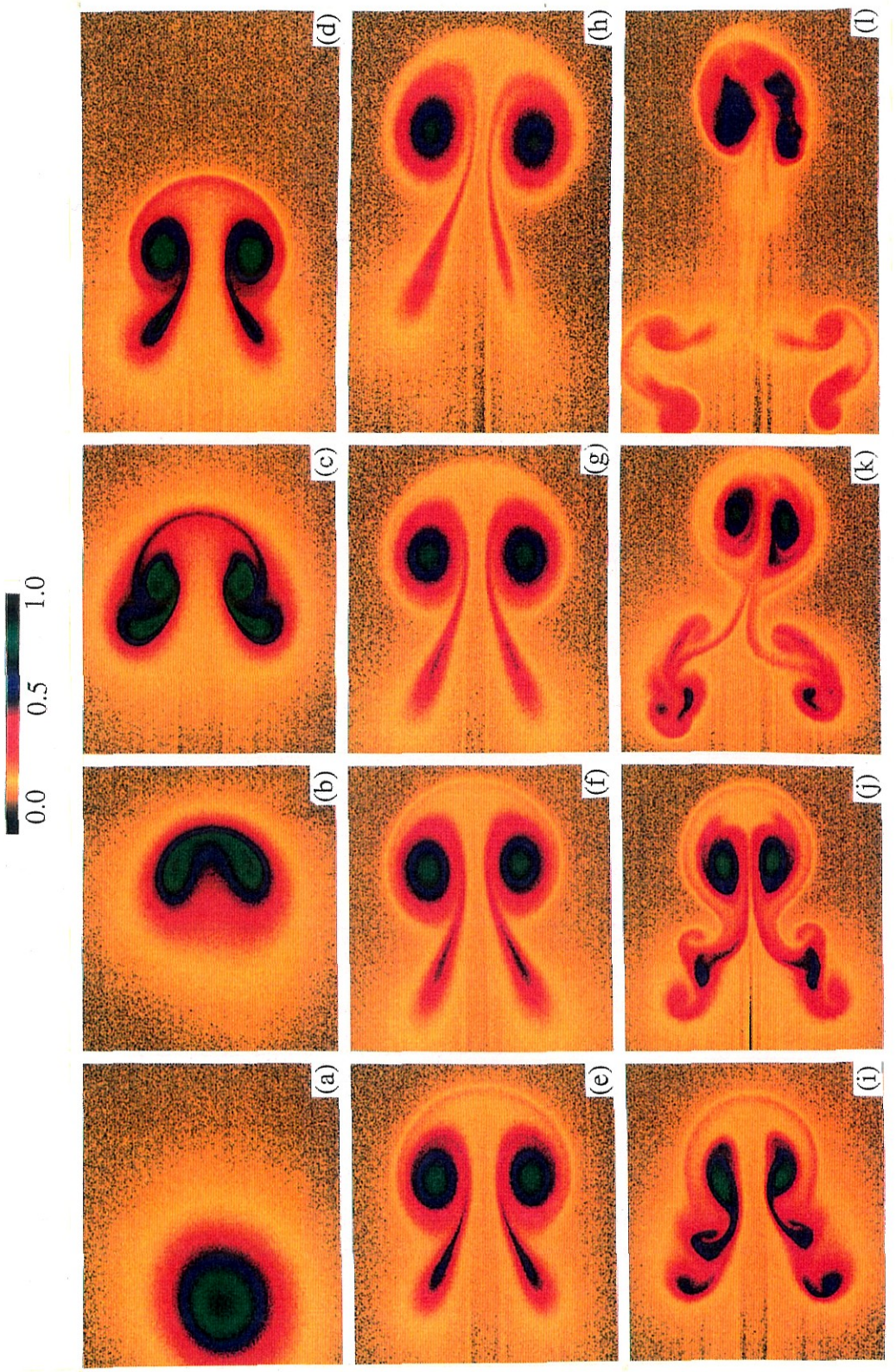
0.0
0.5
1.0
(a)
(b)
(c)
(d)
(e)
(f)
(g)
(h)
(i)
(j)
(k)
(l)

Figure 3-3. Rayleigh Scattering Image, M = 1.066, $a_1 t/r_0 = 111$.

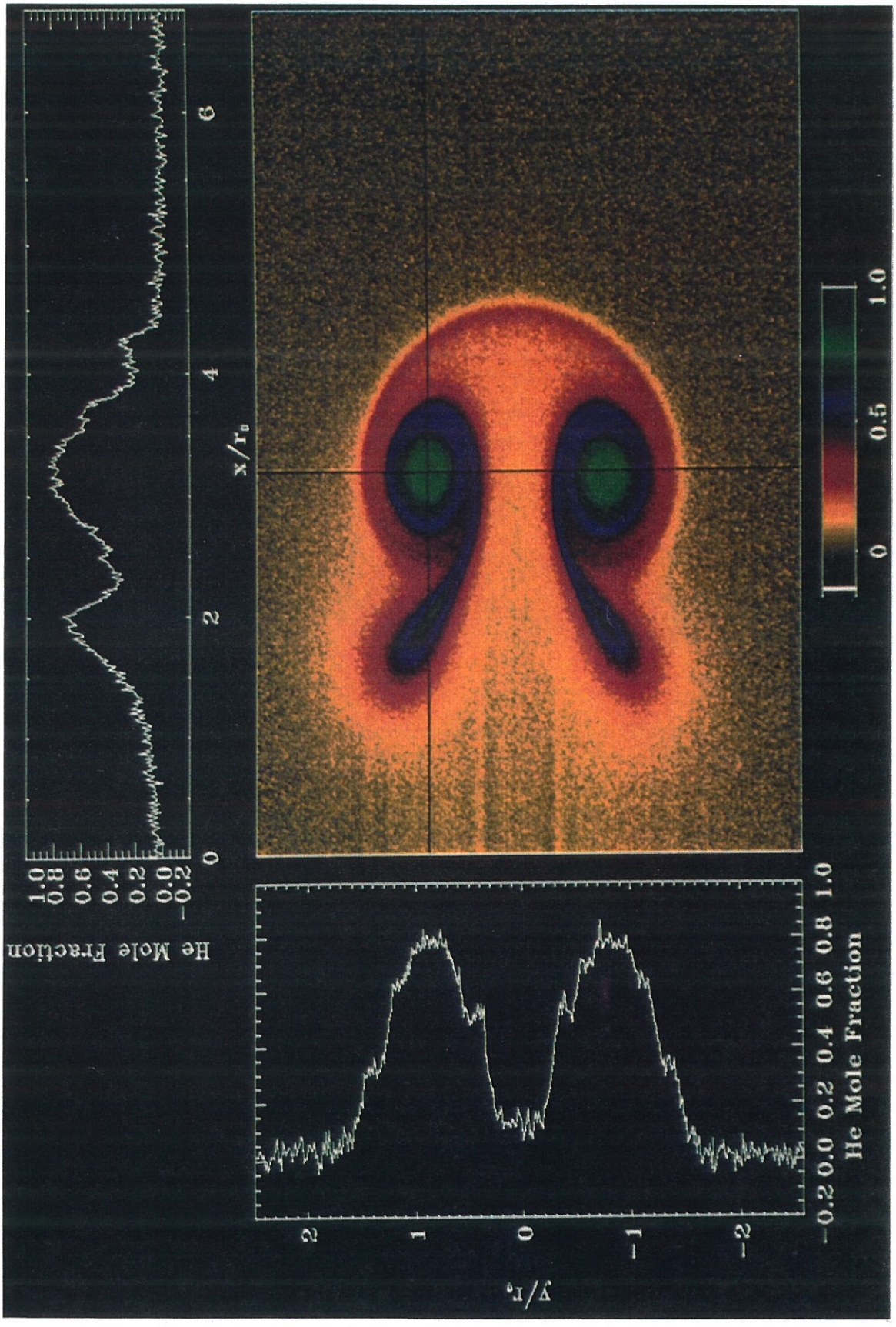
He Mole Fraction
1.0
0.8
0.6
0.4
0.2
0.0
−0.2
0
2
4
6
x/r₀
y/r₀
2
1
0
−1
−2
−0.2 0.0 0.2 0.4 0.6 0.8 1.0
He Mole Fraction
0
0.5
1.0

Figure 3-4. M = 1.146, p = 1 atm (a) $a_1 t/r_0$ = 0, (b) 0.5, (c) 1.5, (d) 4, (e) 15, (f) 22, (g) 29, (h) 45, (i) 52, (j) 74.

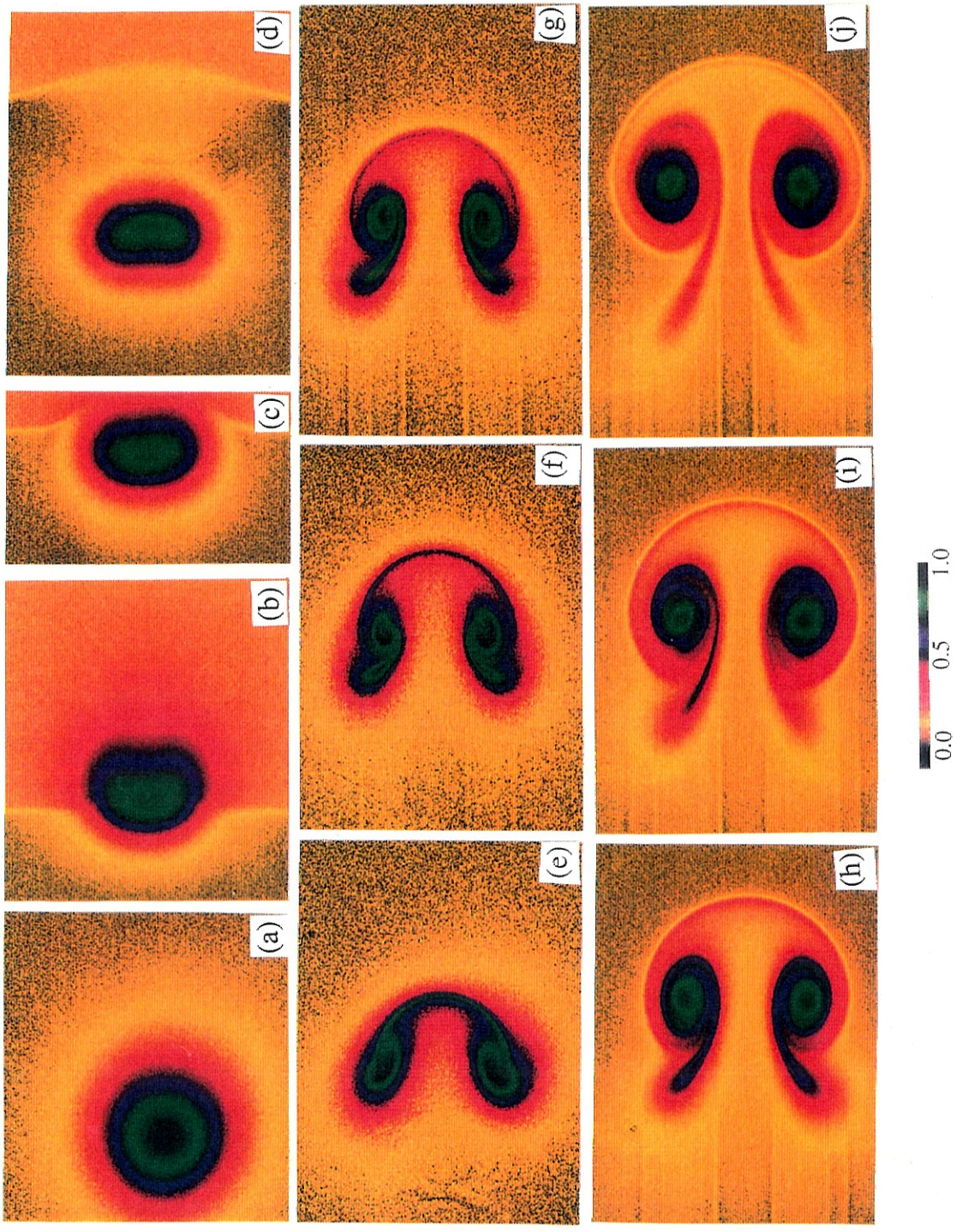
(a)
(b)
(c)
(d)
(e)
(f)
(g)
(h)
(i)
(j)
0.0
0.5
1.0

Figure 3-5. M = 1.142, p = 0.55 atm, Without a Reflect Shock (a) $a_1t/r_0 = 0$, (b) 8, (c) 28, (d) 38, (e) 53, (f) 81, With a Reflected Shock at $a_1t/r_0 = 80$ (g) 88, (h) 107, (i) 120.

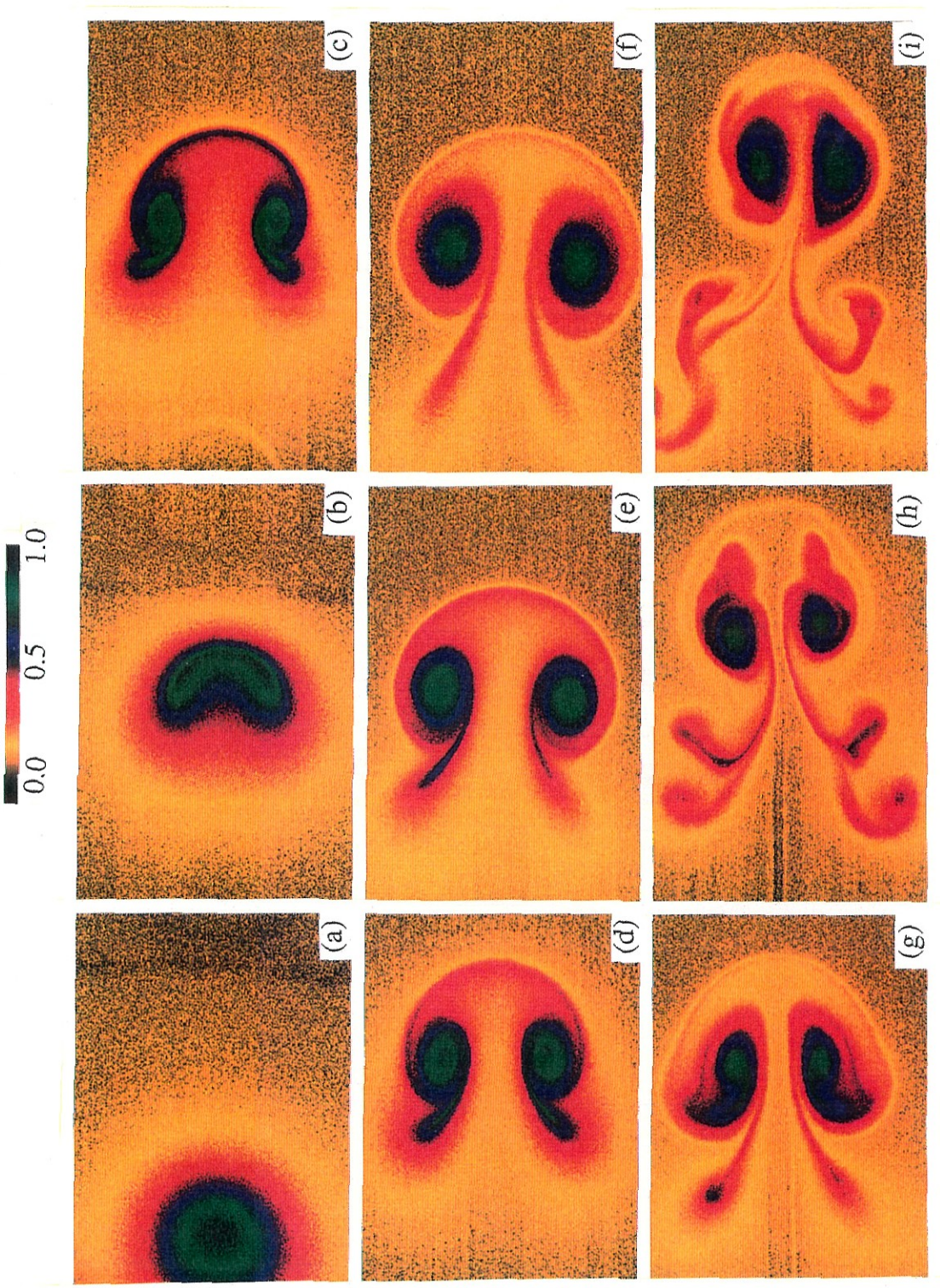
(a)
(b)
(c)
(d)
(e)
(f)
(g)
(h)
(i)
0.0
0.5
1.0

Figure 3-6. M = 1.50, (a) $a_1 t/r_0$ = 6.3, (b) 10.4, (c) 15.5, (d) 21.1, (e) 26.2, (f) 31.7.

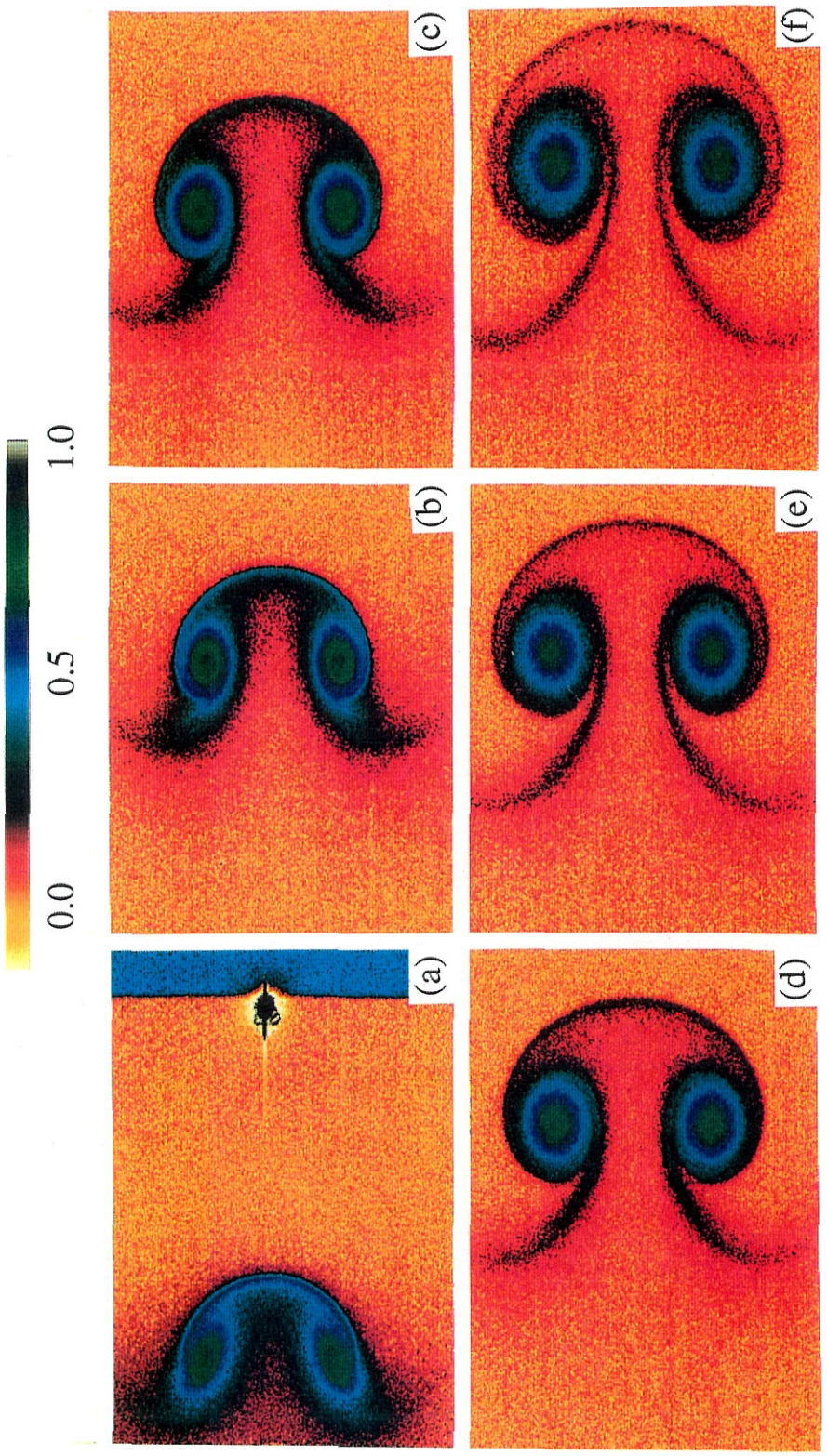
0.0
0.5
1.0
(a)
(b)
(c)
(d)
(e)
(f)

Figure 3-7. M = 2.00 Without a Reflected Shock (a) a_1t/r_0 = 4.9, (b)7.5, (c) 9.3, (d) 10.5, (e) 16.6, (f) 20.6, (g) 24.3, With a Reflected Shock at a_1t/r_0 = 23.5, (h) 23.5, (i) 25.2, (j) 26.9, (k) 29.6.

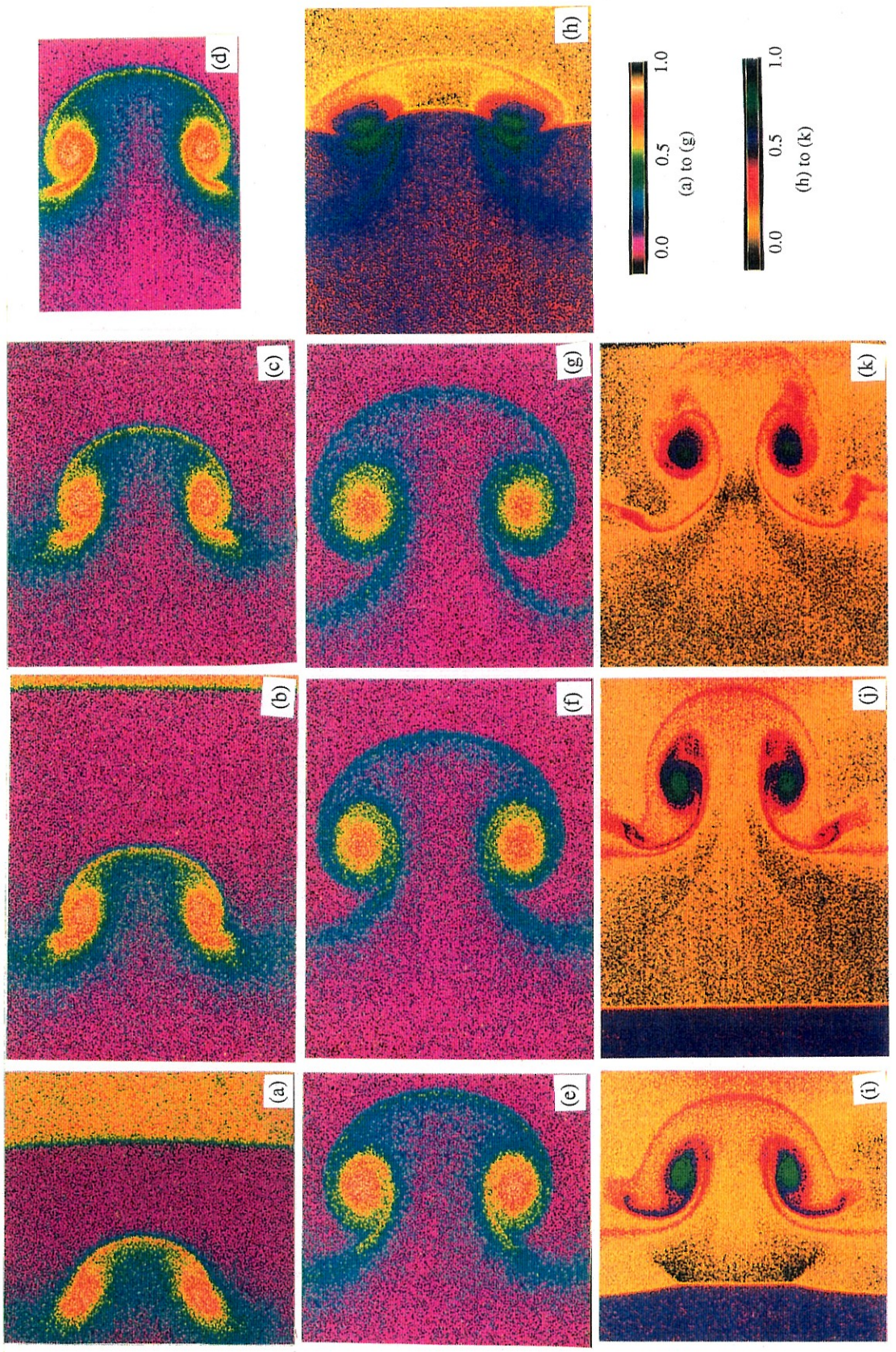
(a)
(b)
(c)
(d)
(e)
(f)
(g)
(h)
(i)
(j)
(k)
0.0
0.5
1.0
(a) to (g)
0.0
0.5
1.0
(h) to (k)

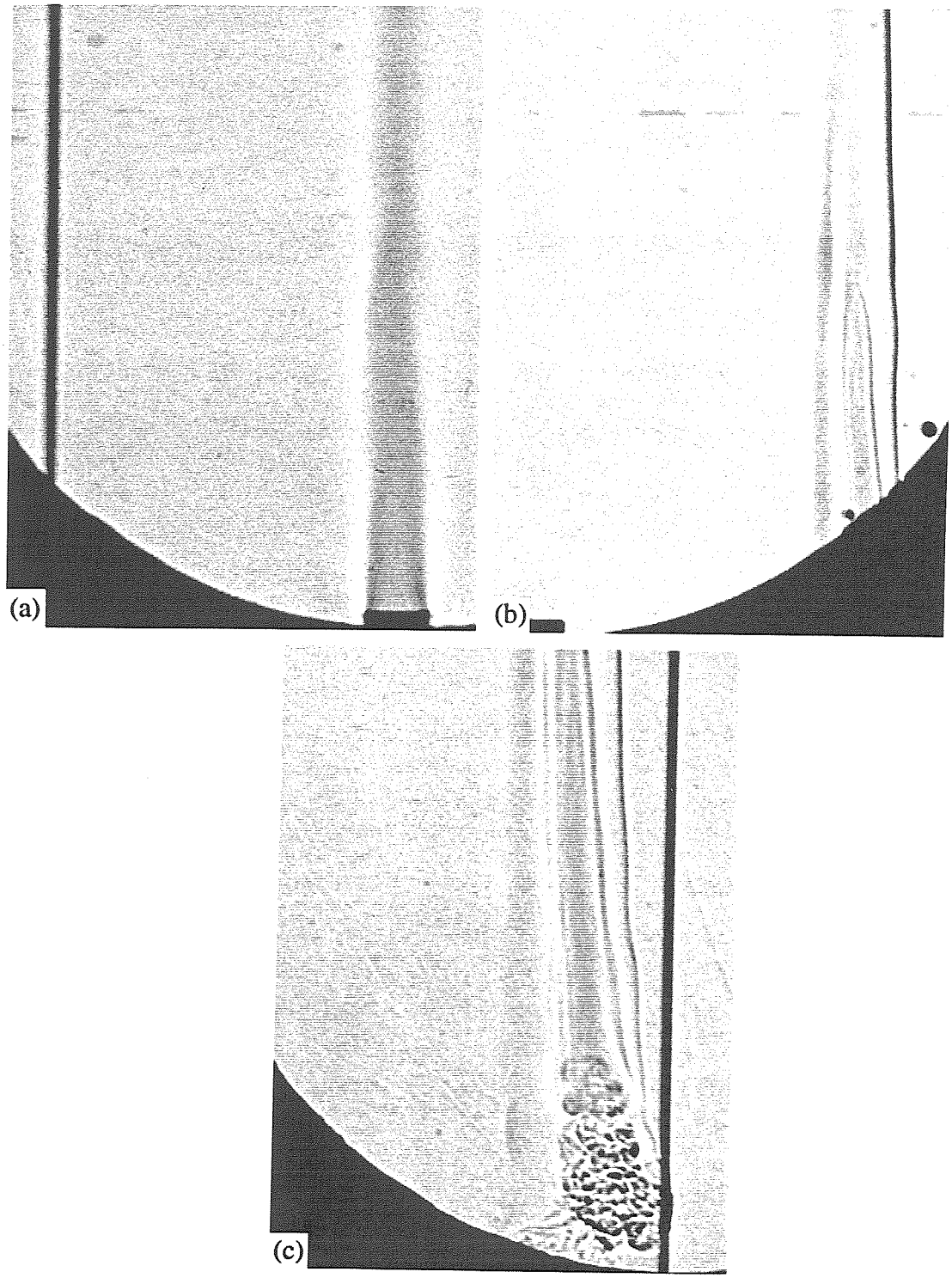

Figure 3-8. Shadowgraph Sequence for M = 1.066, (a) $a_1 t/r_0 = 0$, (b) 99, (c) 202.

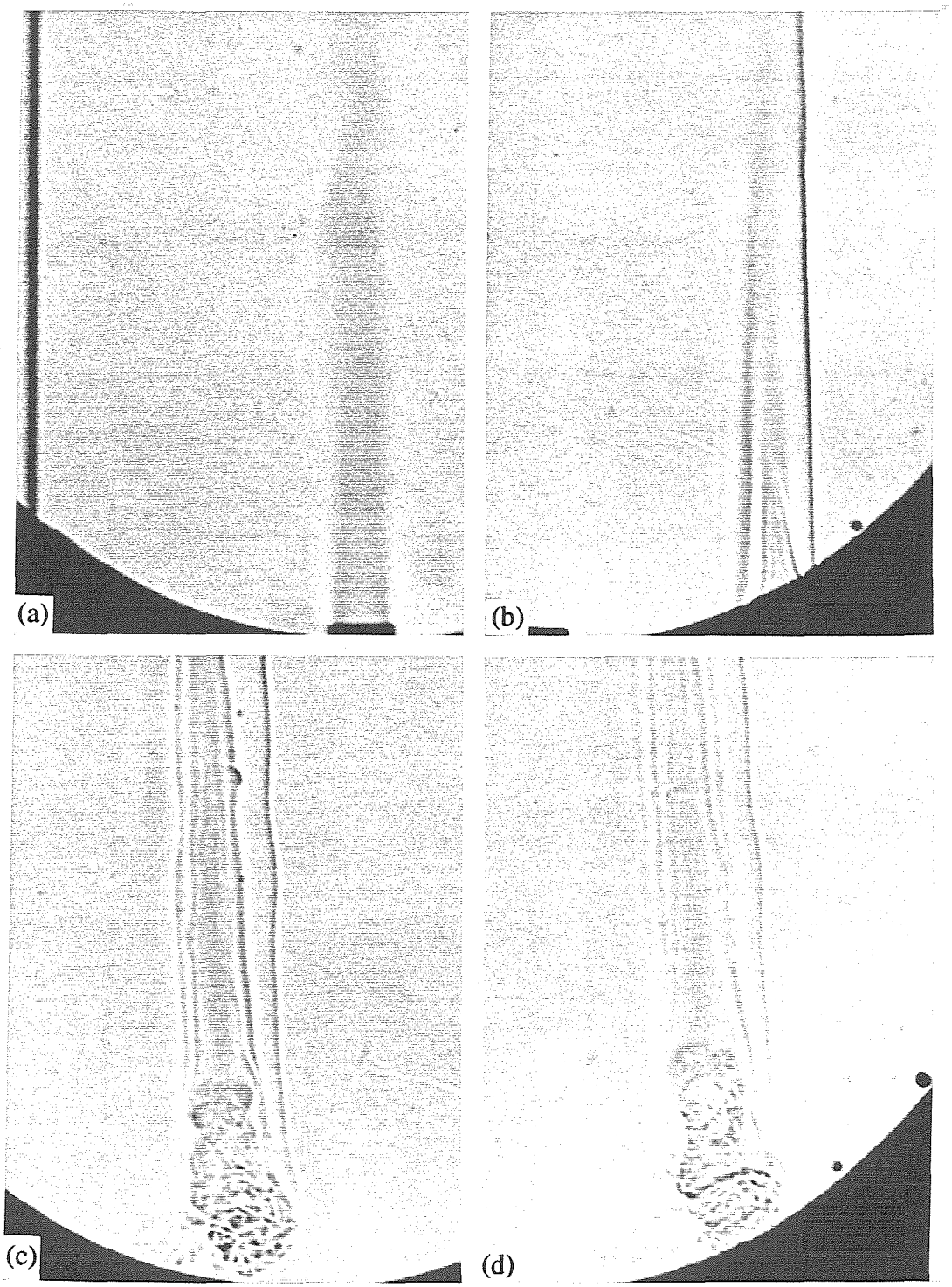

Figure 3-9. Shadowgraph Sequence for M = 1.142, p = 0.55 atm. (a) $a_1 t/r_0 = 0$, (b) 42, (c) 81, (d) 116.

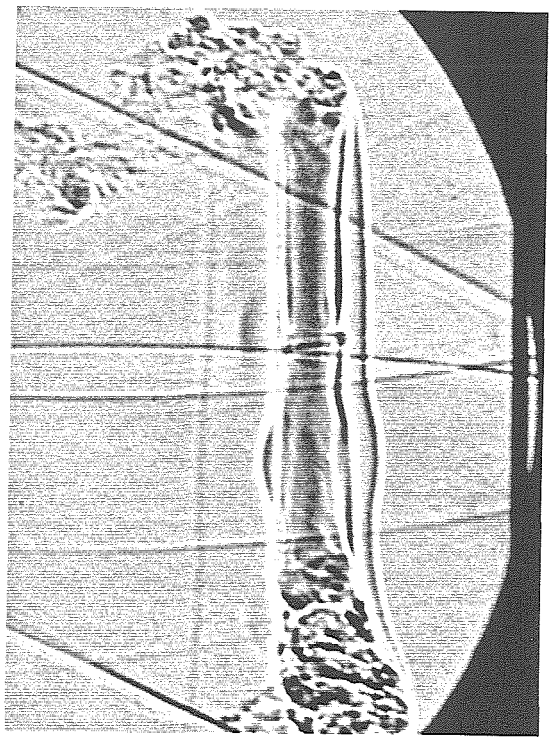

Figure 3-10. M = 1.146, p = 1 atm, $a_1 t/r_0 = 80$.

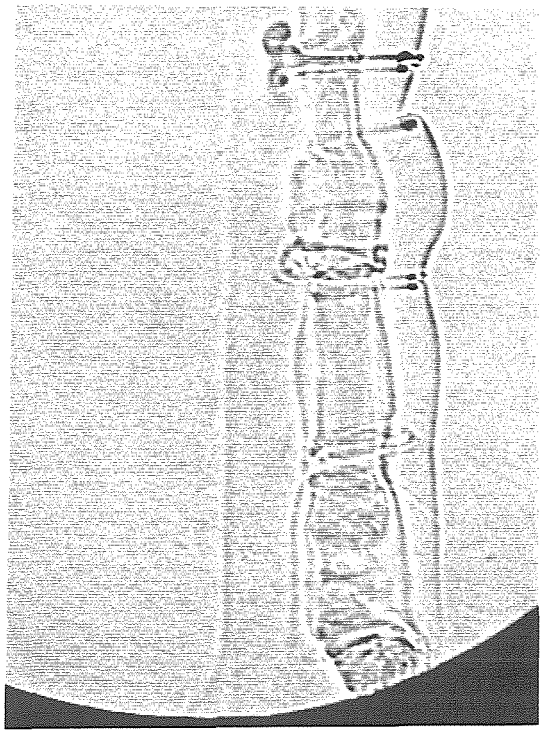

Figure 3-11. M = 1.50, $a_1 t/r_0 = 30$.

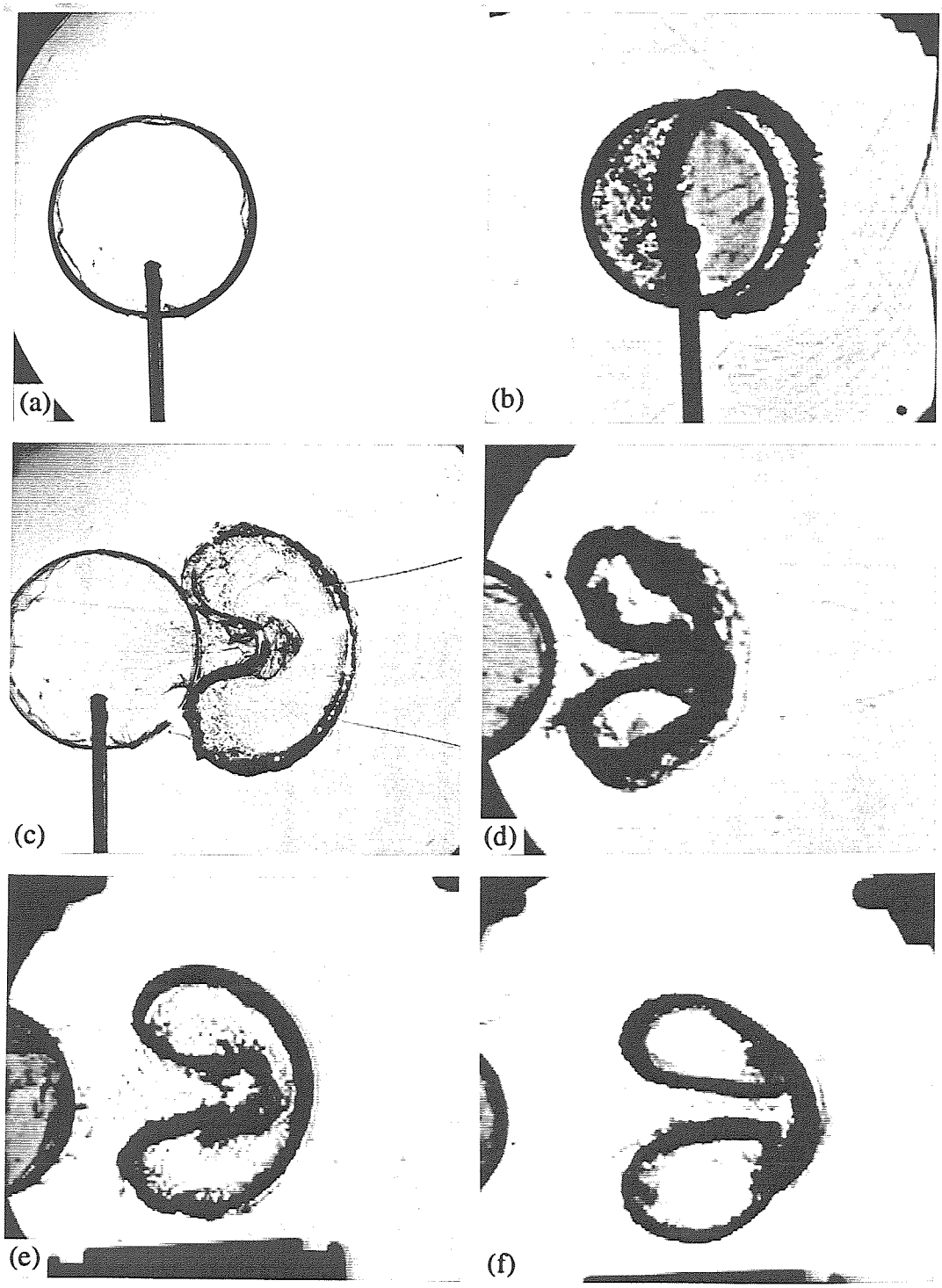

Figure 3-12. Microfilm Experiments, M = 1.1, (a) $a_1 t/r_0$ = 0, (b) 3.0, (c) 9.0, (d) 10.6, (e) 14.0, (f) 17.4.

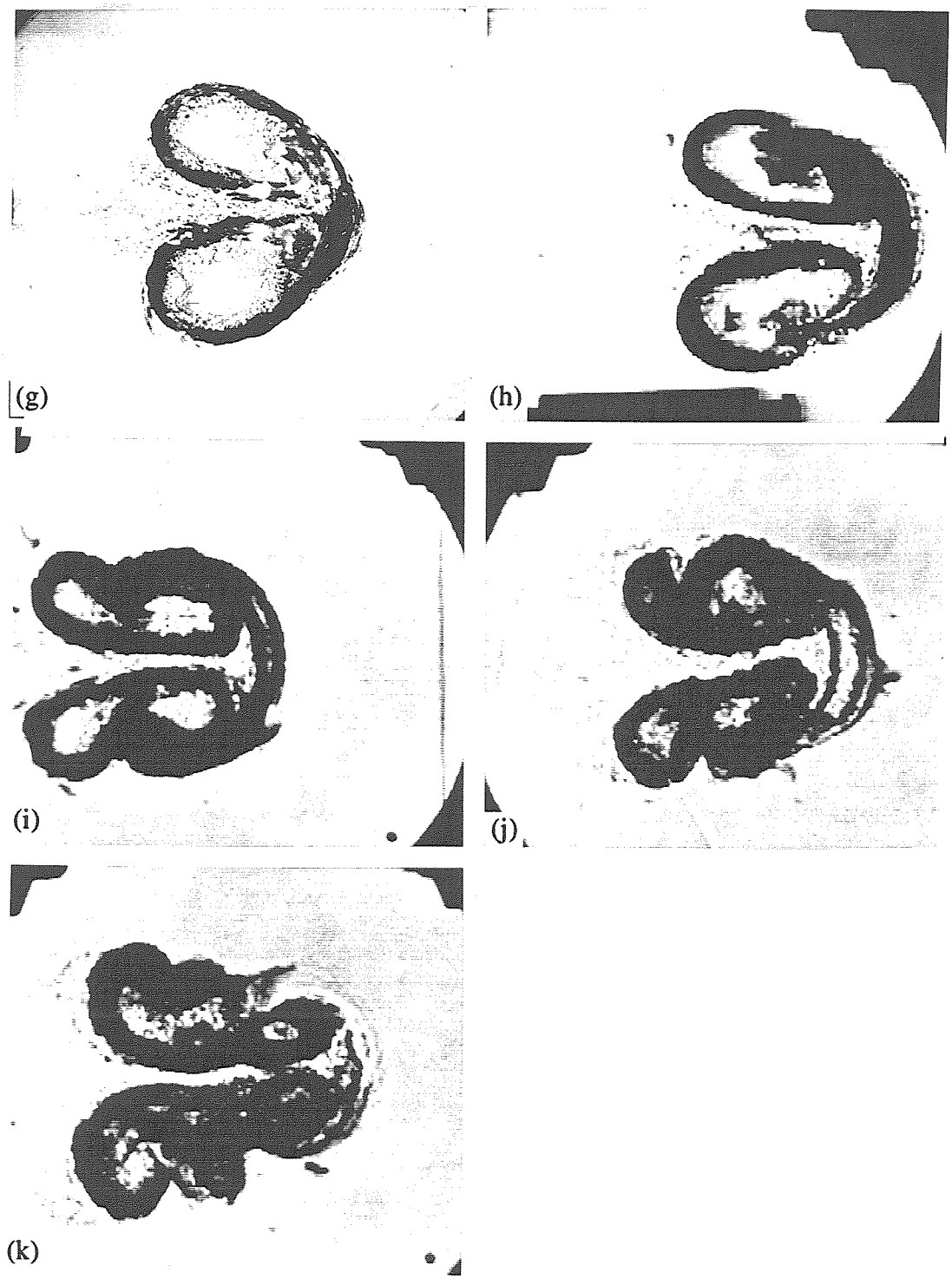

Figure 3-12. (cont) (g) a_1t/r_0 = 20.4, (h) 24.2, (i) 34.5, After the Reflected Shock at a_1t/r_0 = 35, (j) 40, (k) 46.7.

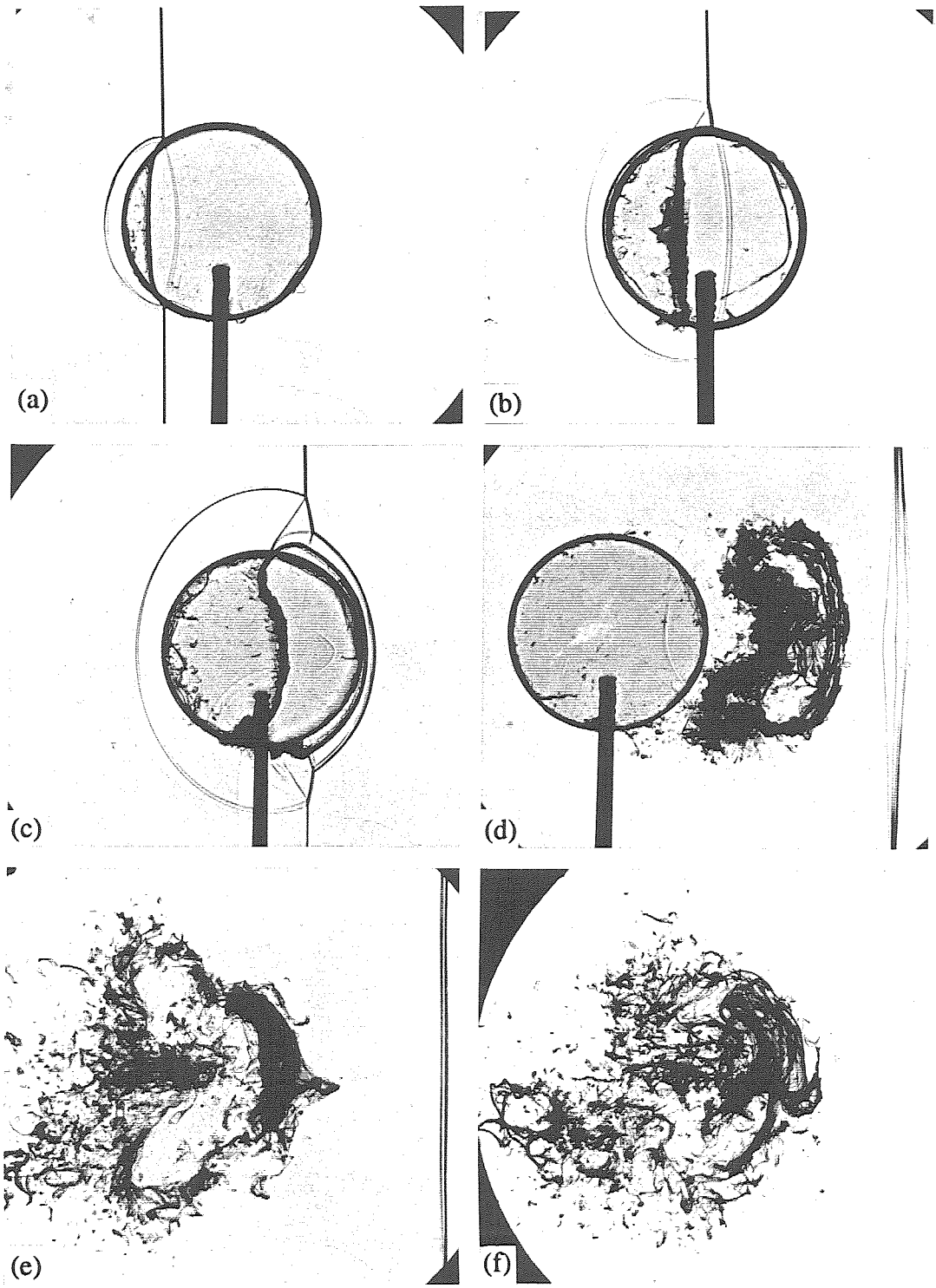

Figure 3-13. Microfilm Experiments, M = 2.0, (a) 0.015 msec, (b) 0.037 msec, (c) 0.055 msec, (d) 0.138 msec, (e) 0.30 msec, (f) 0.44msec.

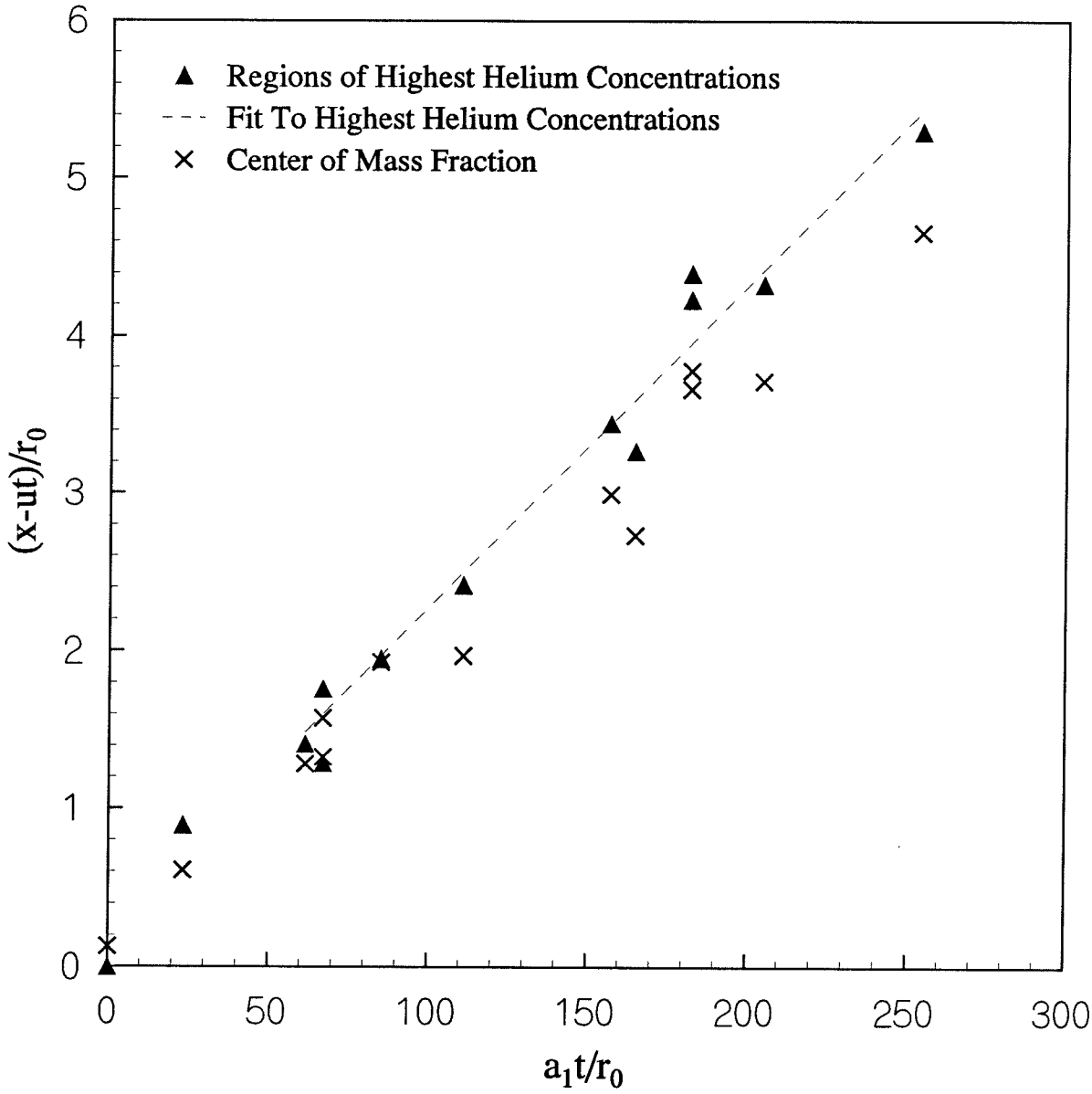

Figure 4-1. Downstream Displacement Relative to the Surrounding Air. M = 1.066, h/D = 5.7

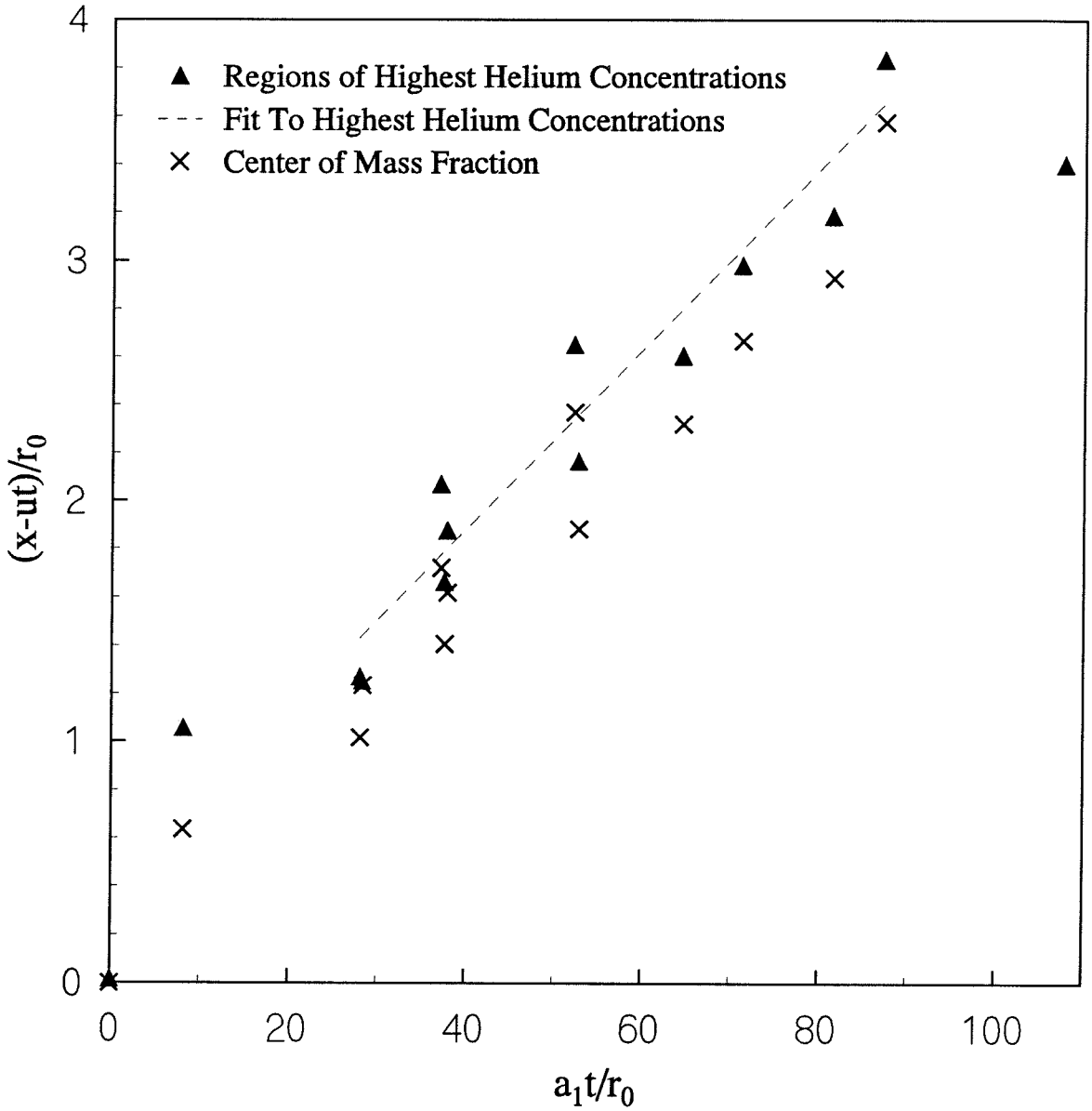

Figure 4-2. Downstream Displacement Relative to the Surrounding Air. $M = 1.142$, $p_1 = 0.55$ atm.

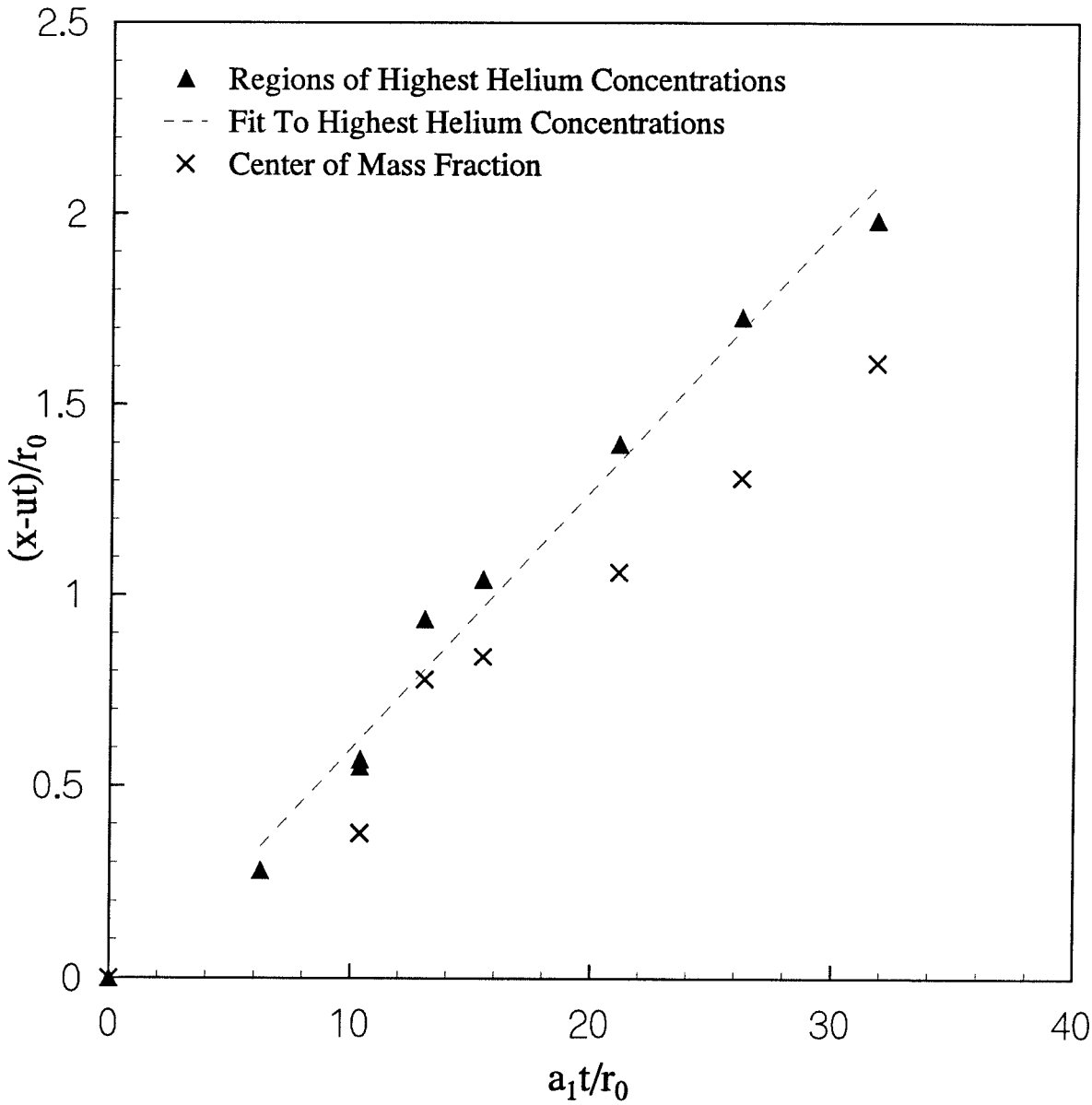

Figure 4-3. Downstream Displacement Relative to the Surrounding Air. M = 1.50 .

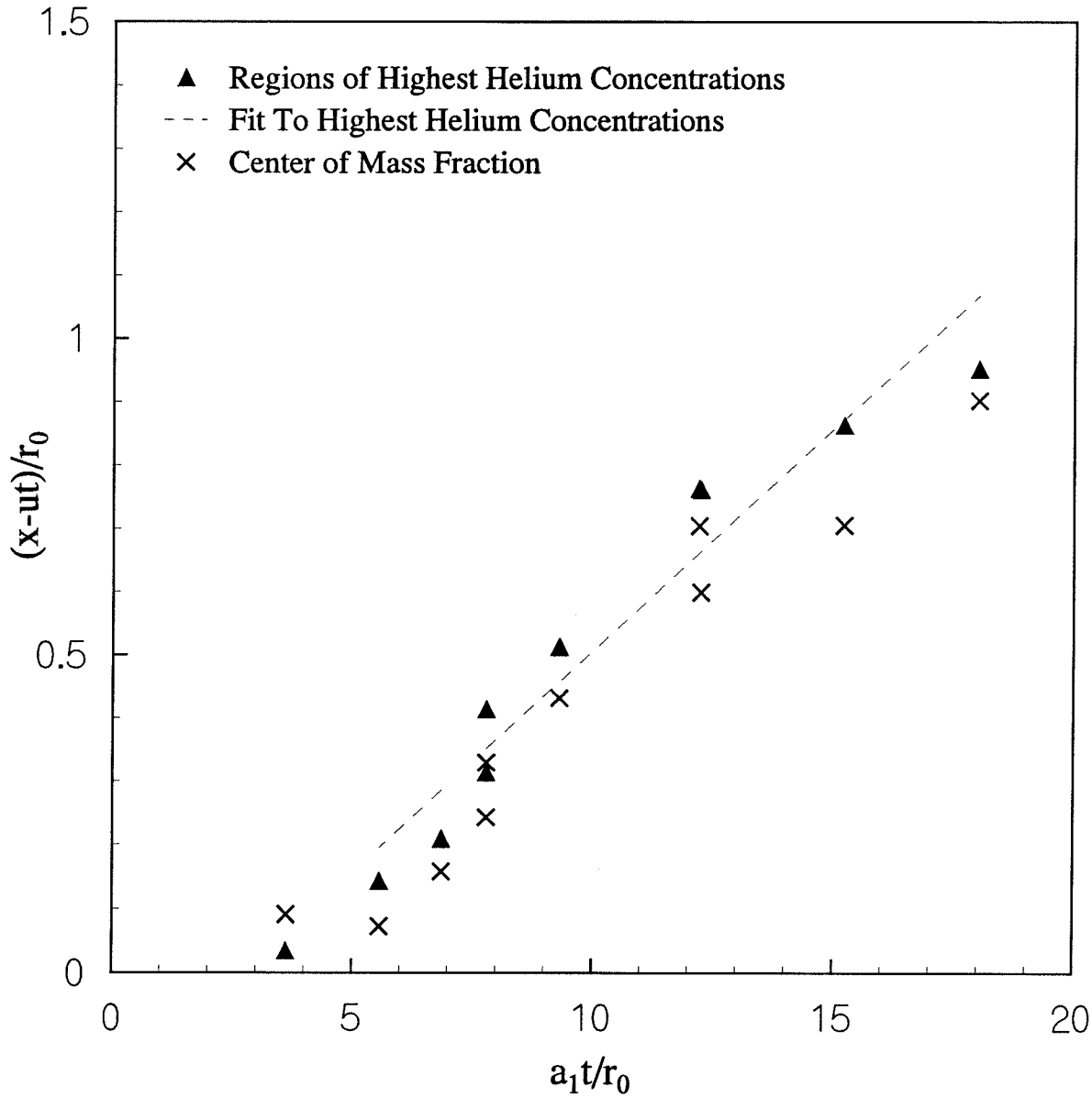

Figure 4-4. Downstream Displacement Relative to the Surrounding Air. M = 2.0 .

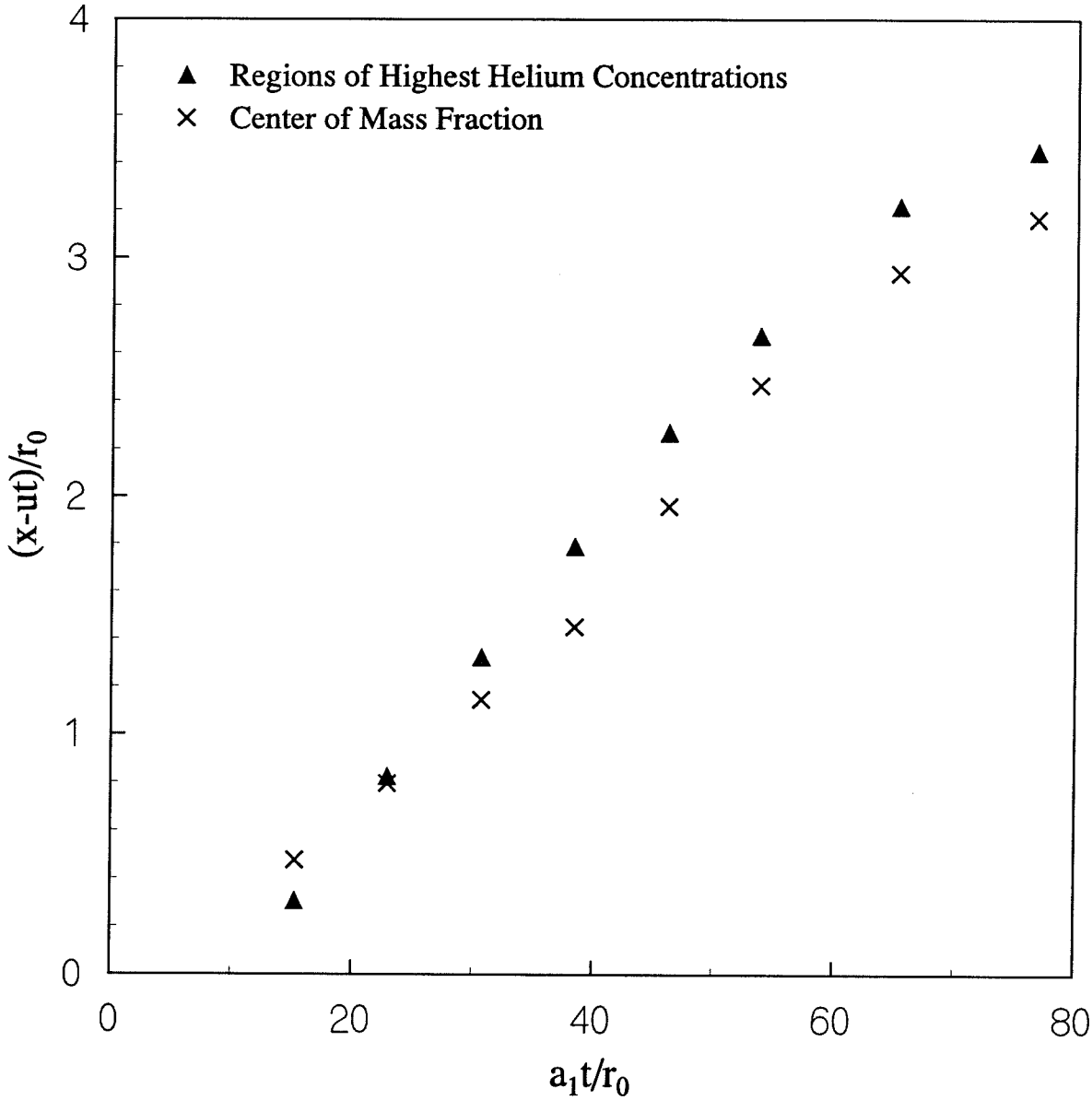

Figure 4-5. Downstream Displacement Relative to the Surrounding Air. M = 1.146, h/D = 4.9, p_1 = 1 atm.

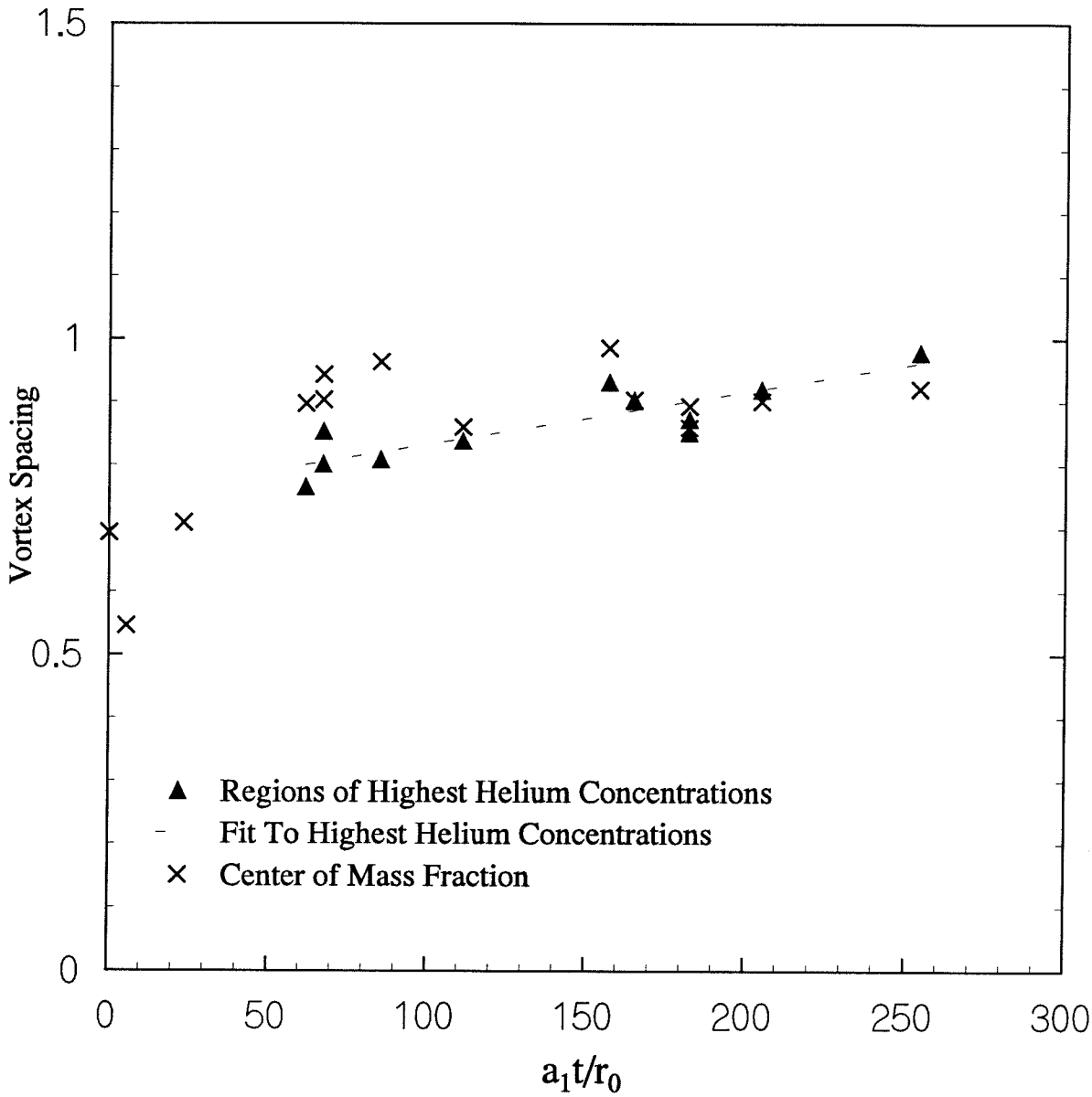

Figure 4-6. Vortex Spacing, M = 1.066, h/D = 5.7 .

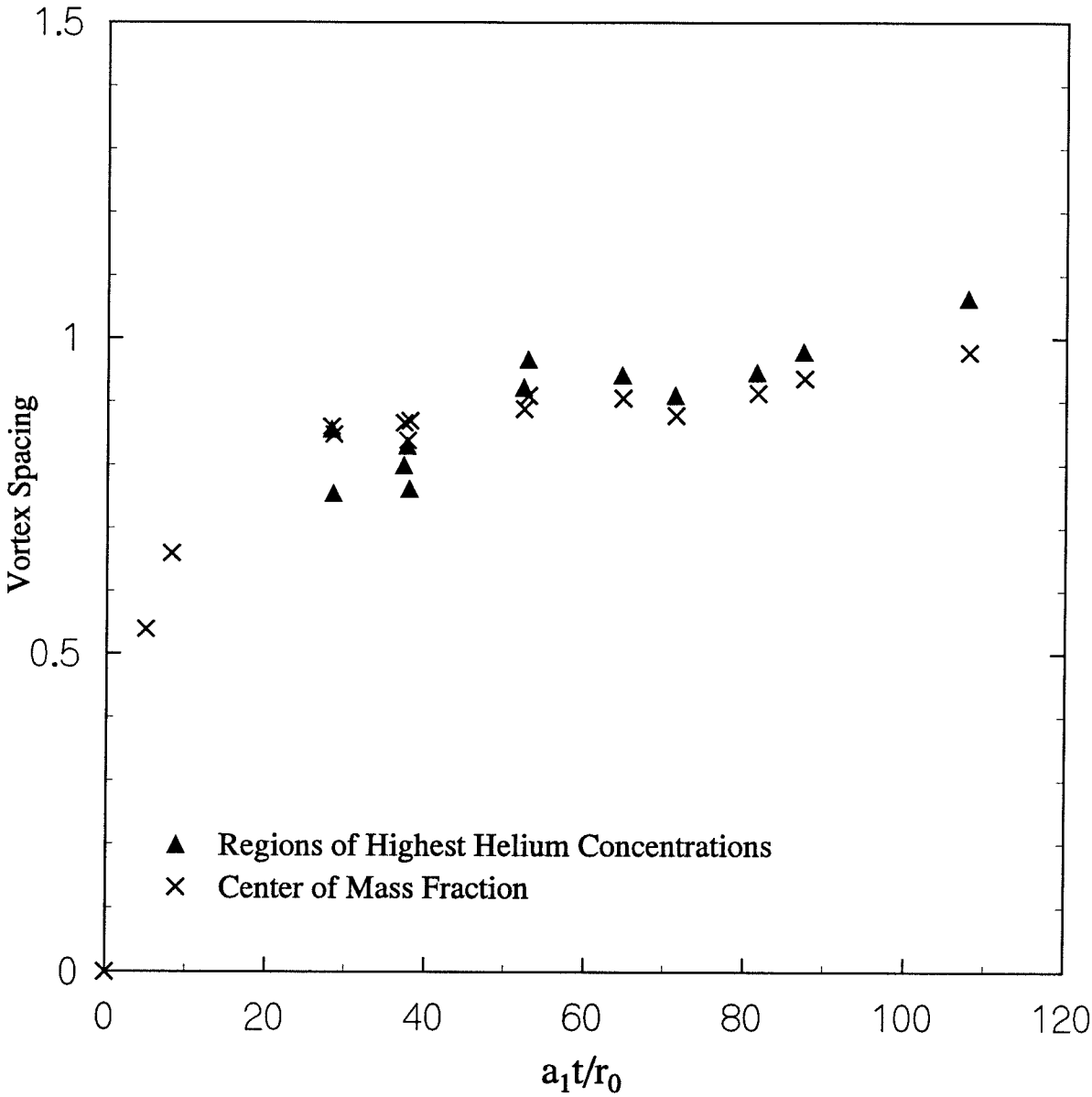

Figure 4-7. Vortex Spacing, M = 1.142 .

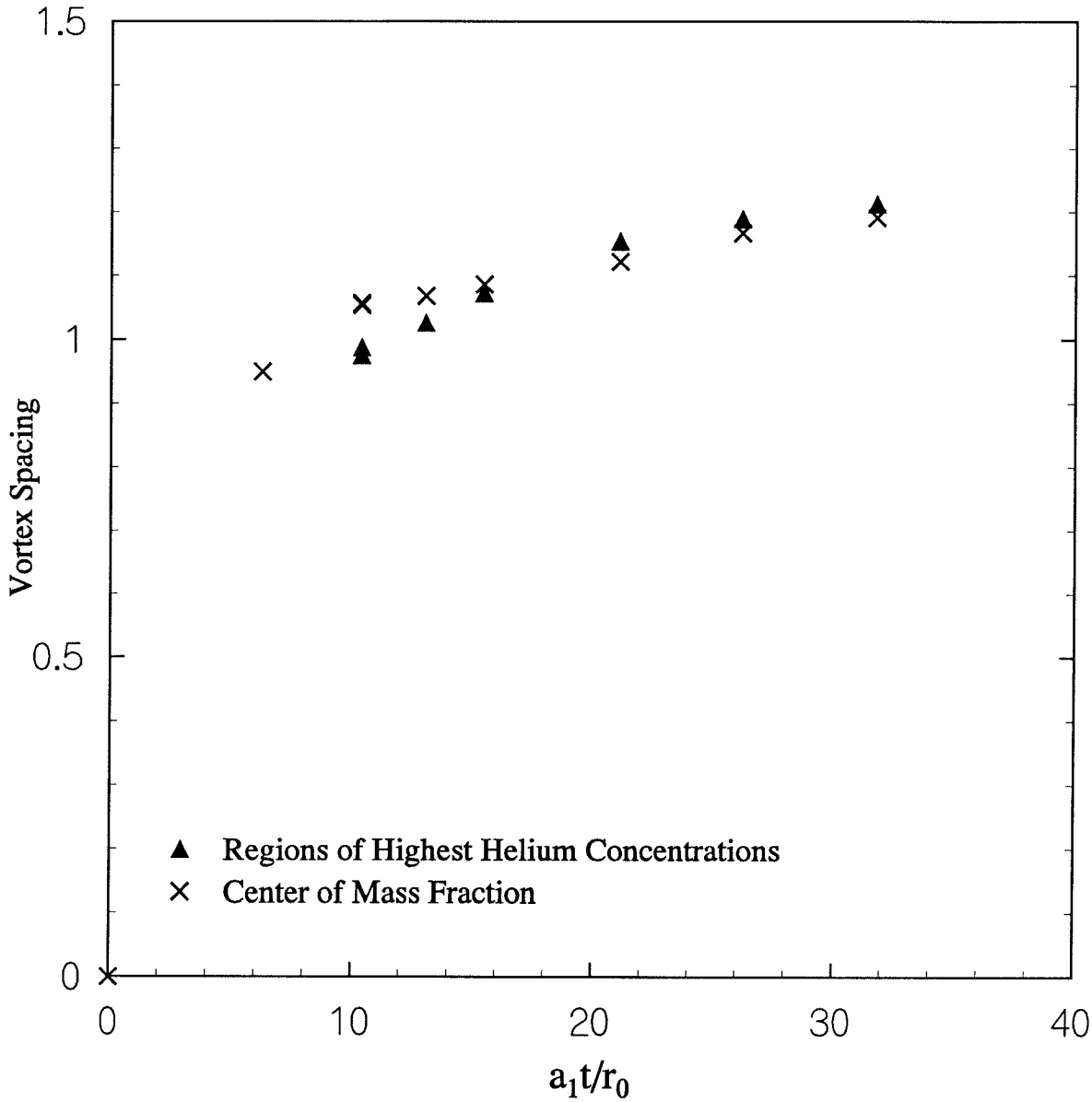

Figure 4-8. Vortex Spacing, M = 1.50 .

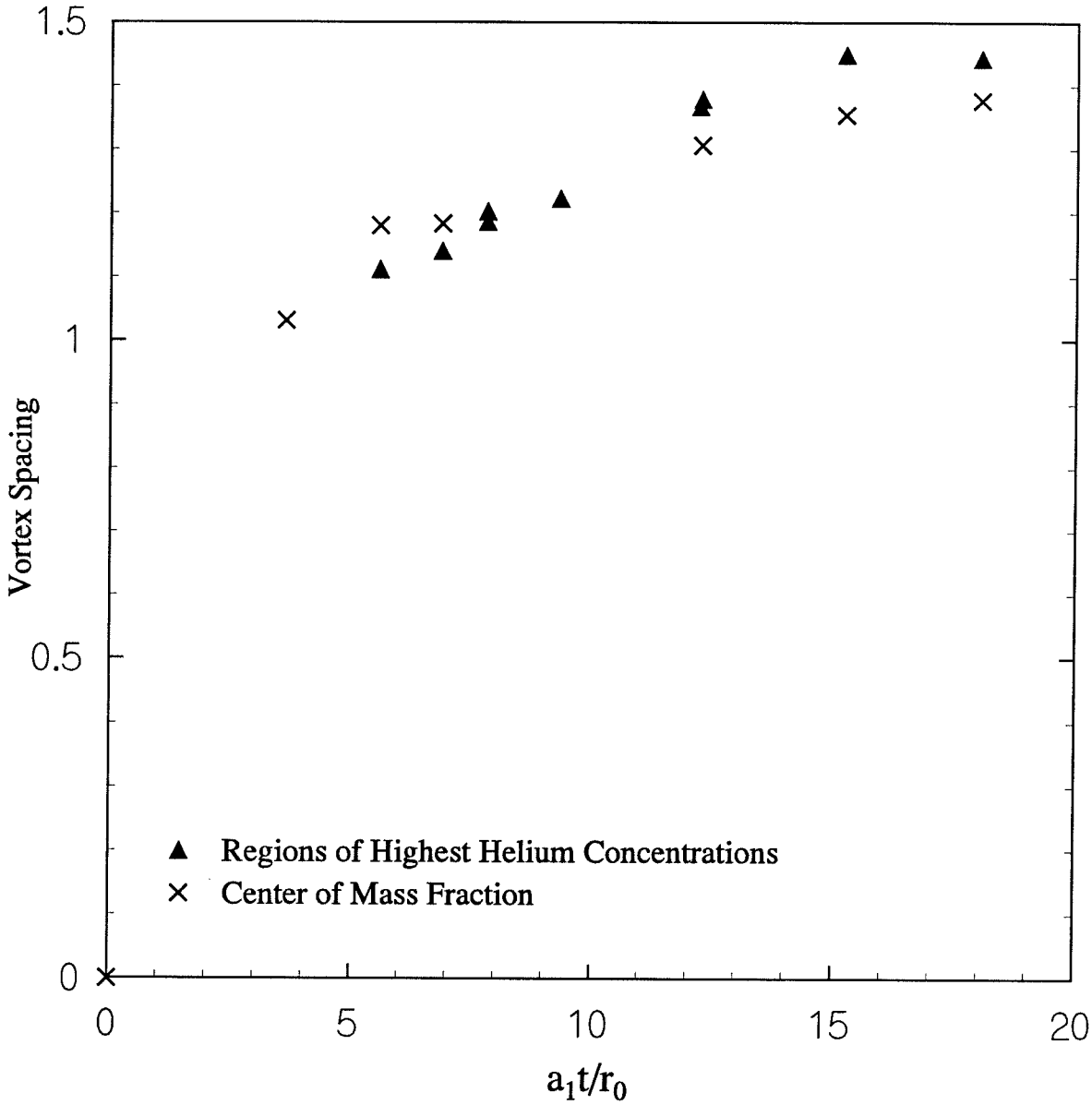

Figure 4-9. Vortex Spacing, M = 2.0 .

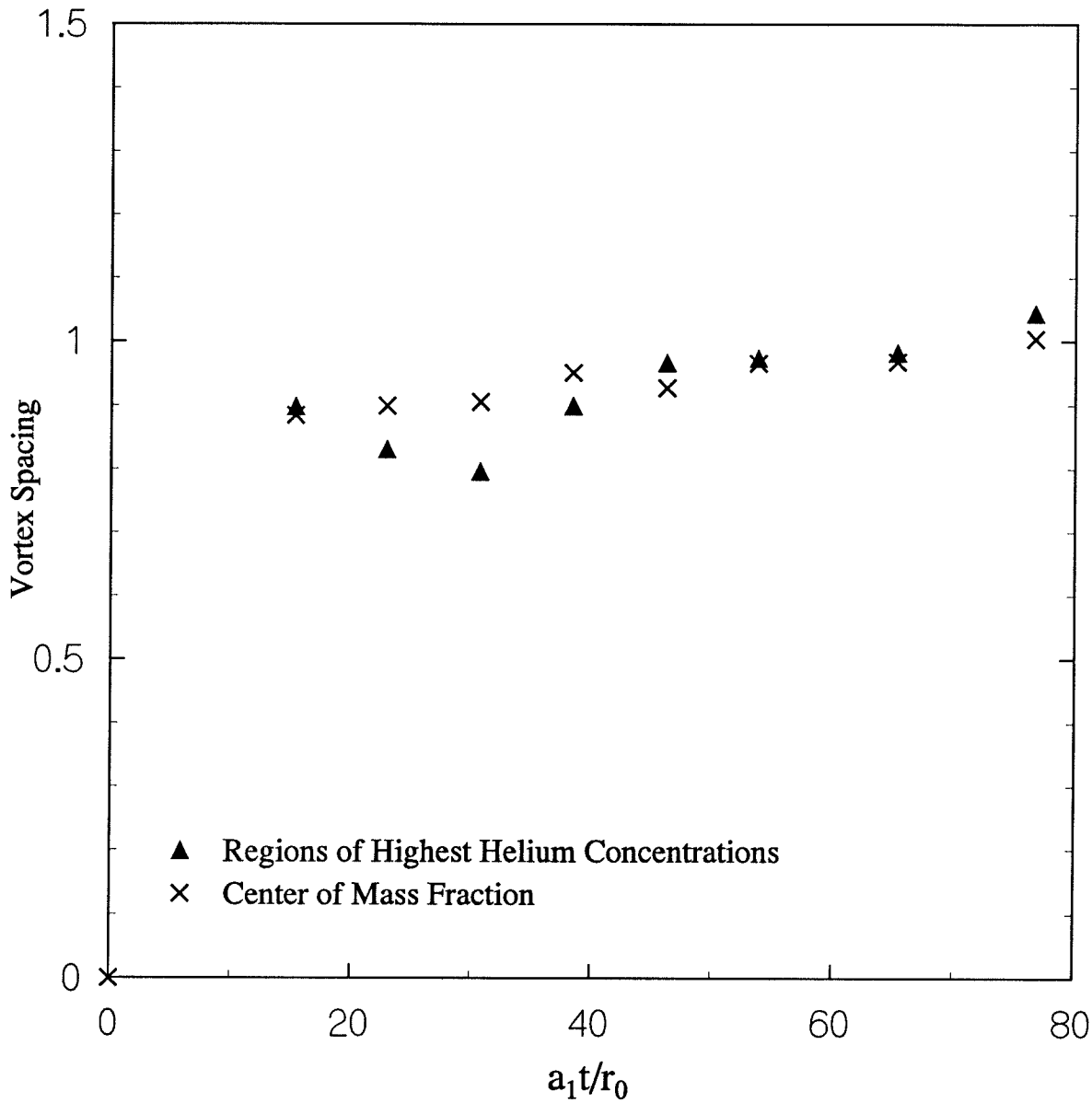

Figure 4-10. Vortex Spacing, M = 1.146, h/D = 4.9 .

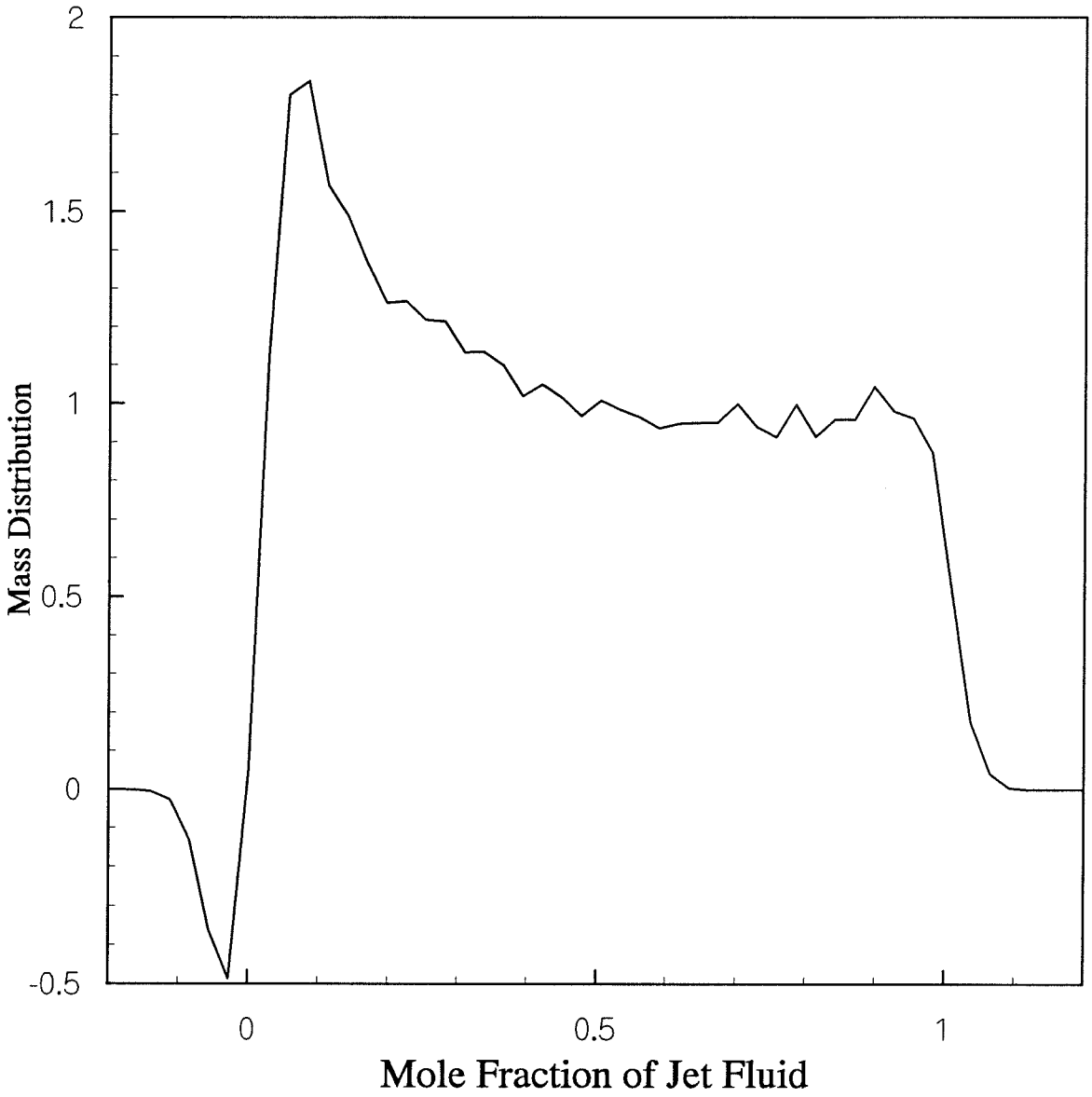

Figure 5-1. Mass Distribution Function for a Typical Initial Jet.

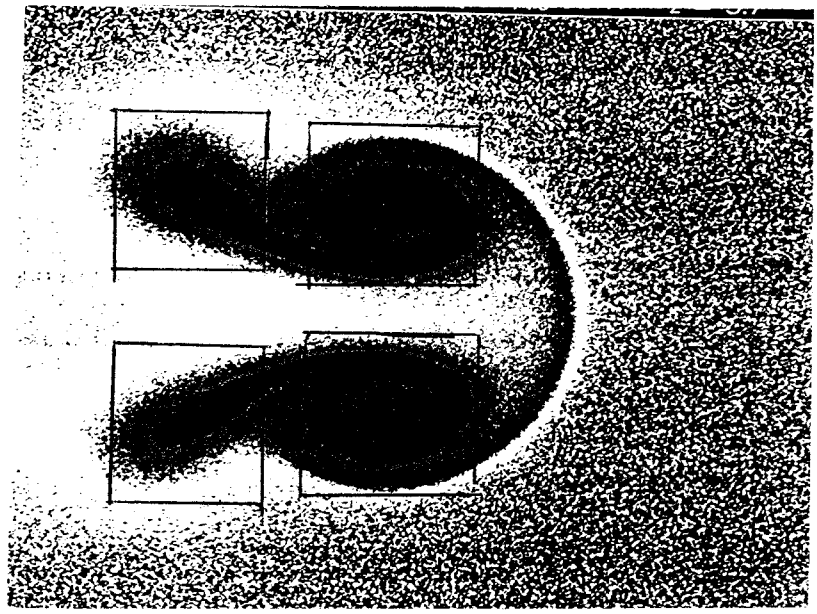

Figure 5-2. Example of the Boxes Around the Tails and Vortex Cores.

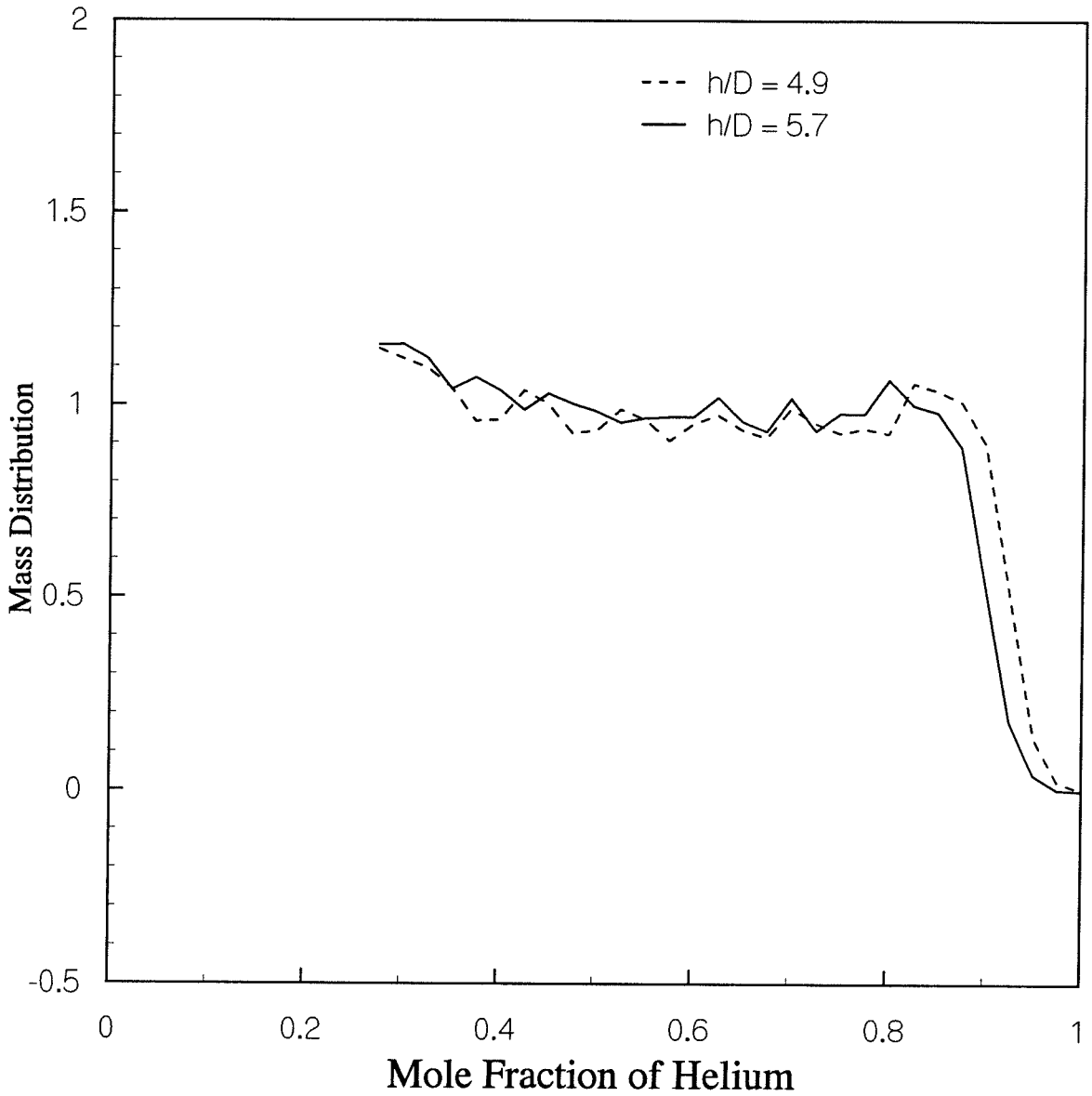

Figure 5-3. Mass Distribution Function for Two Initial Jet Cross Sections, One at h/D = 4.9, and the Other at h/D = 5.7

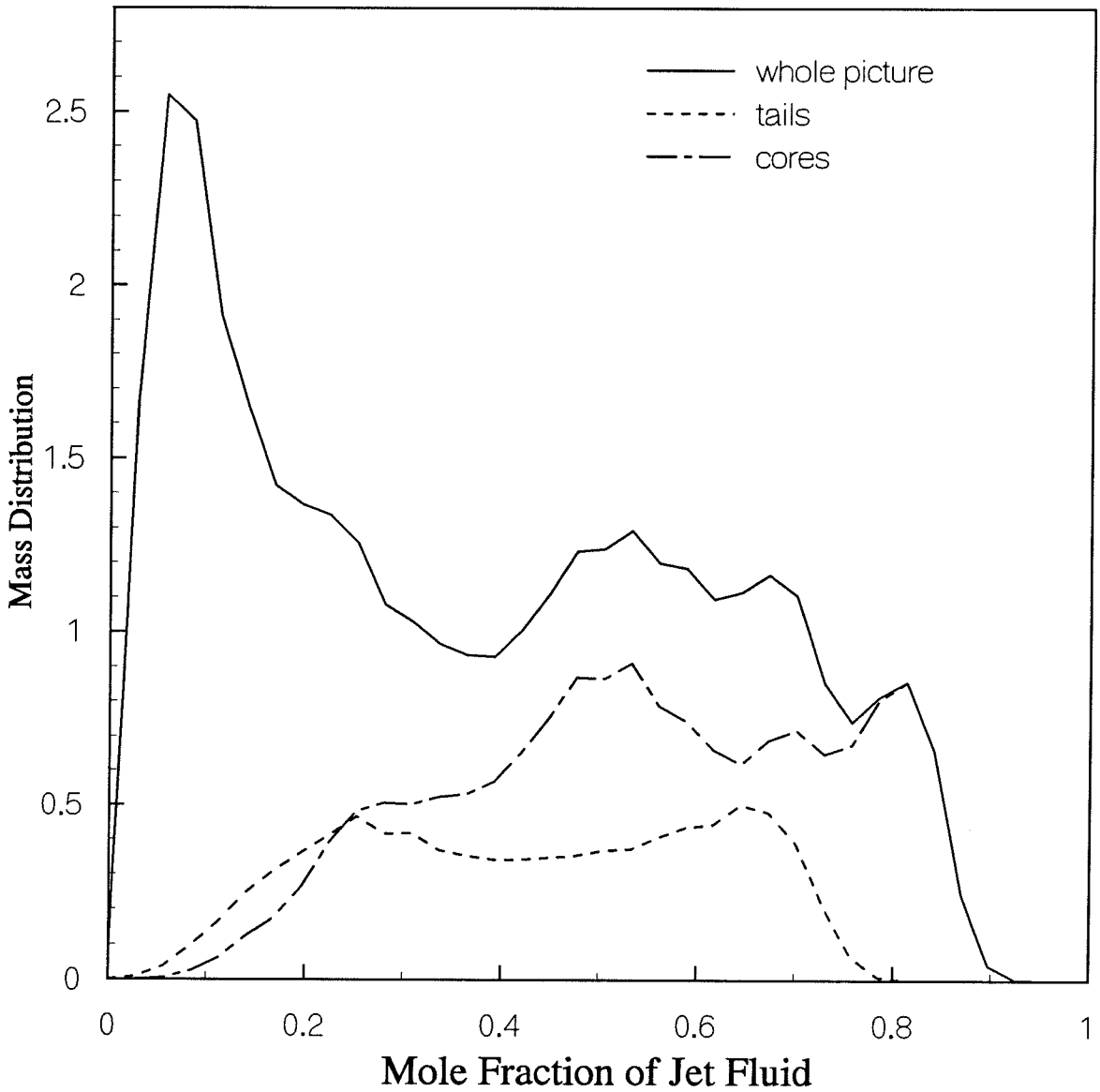

Figure 5-4. Mass Distribution Function for M = 1.066, $a_1 t/r_0 = 156$.

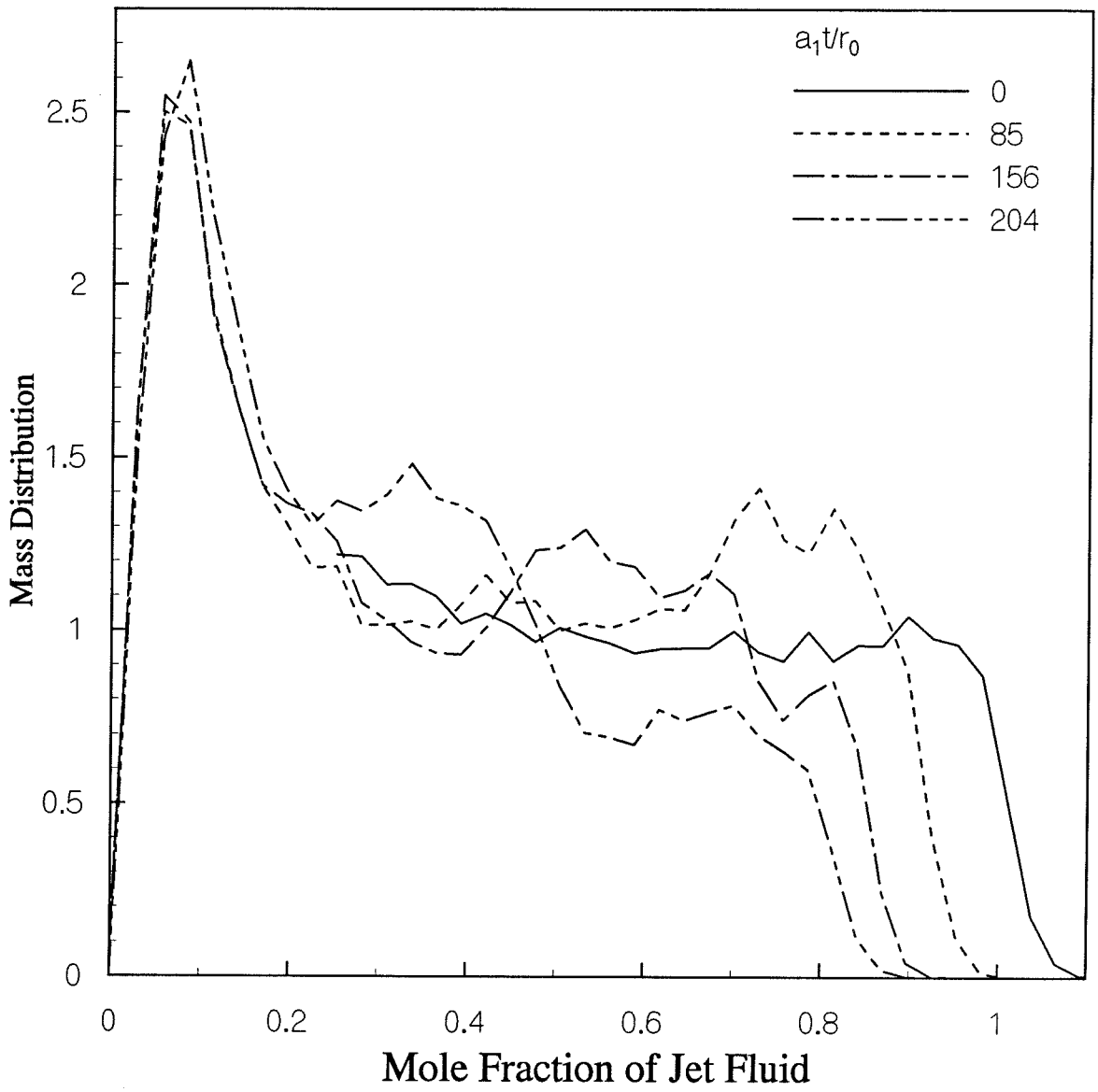

Figure 5-5. Mass Distribution Function for M = 1.066, a_1t/r_0 = 0, 85, 156, and 204.

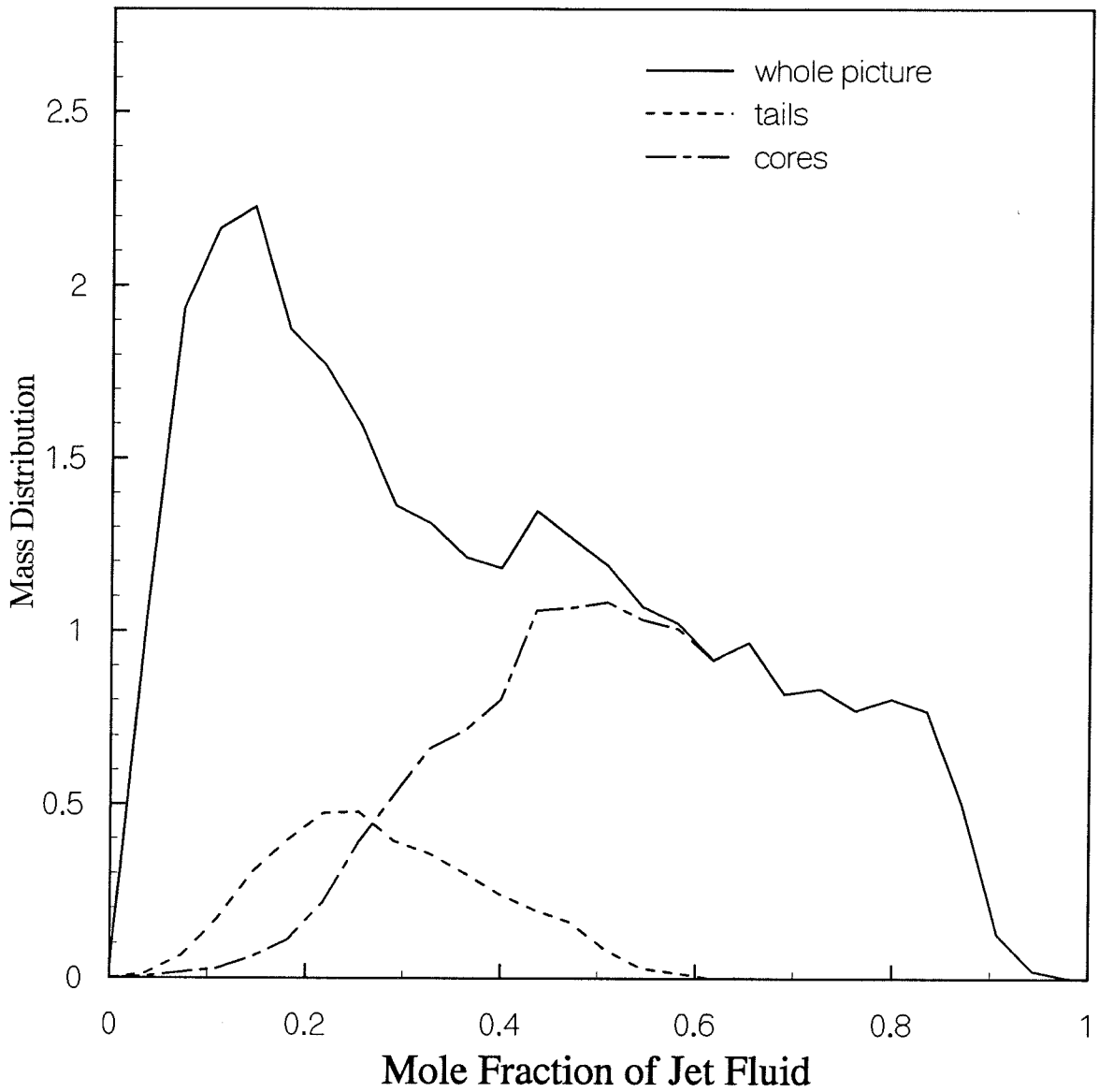

Figure 5-6. Mass Distribution Function for M = 1.142, $a_1 t/r_0 = 64$.

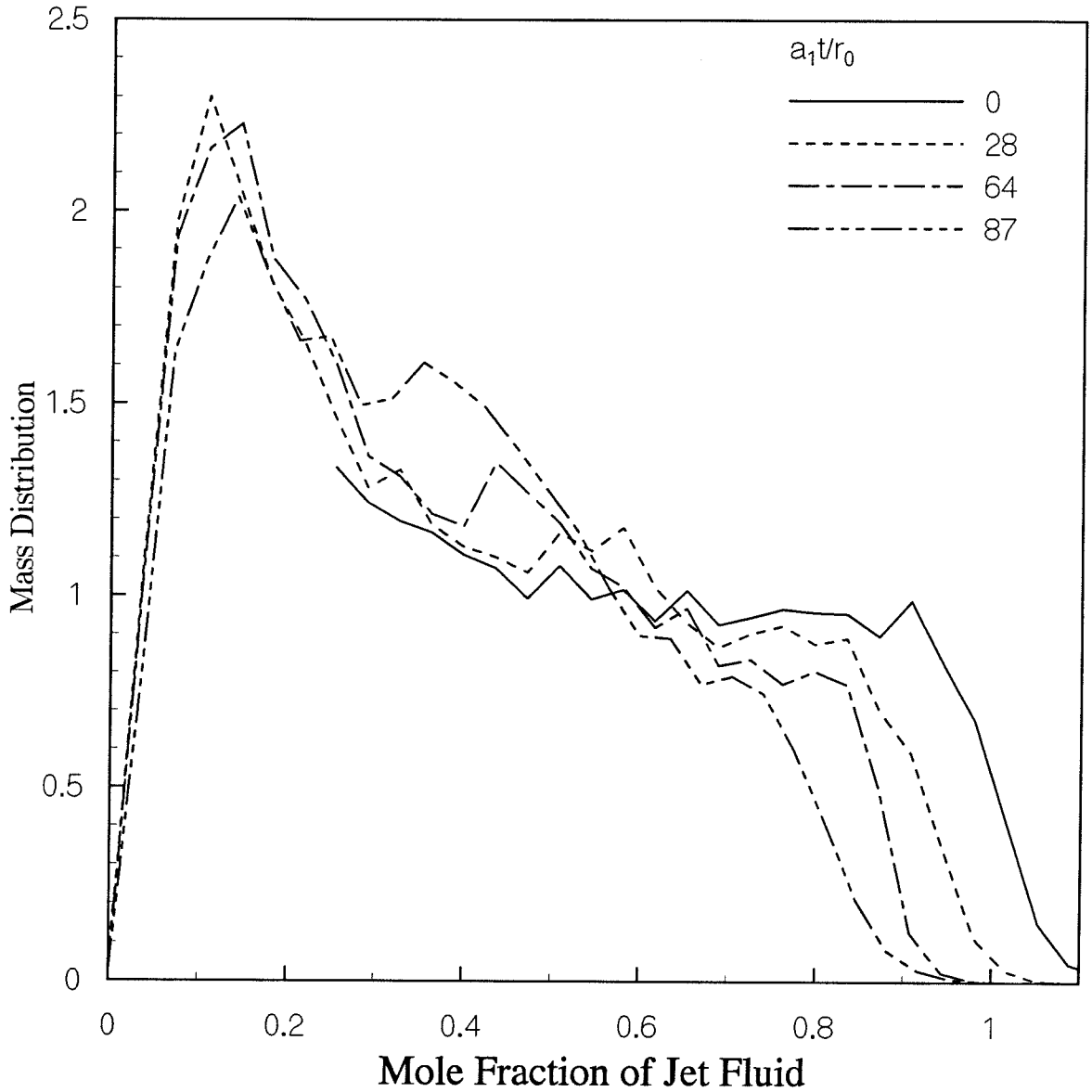

Figure 5-7. Mass Distribution Function for M = 1.142, a_1t/r_0 = 0, 28, 64, and 87.

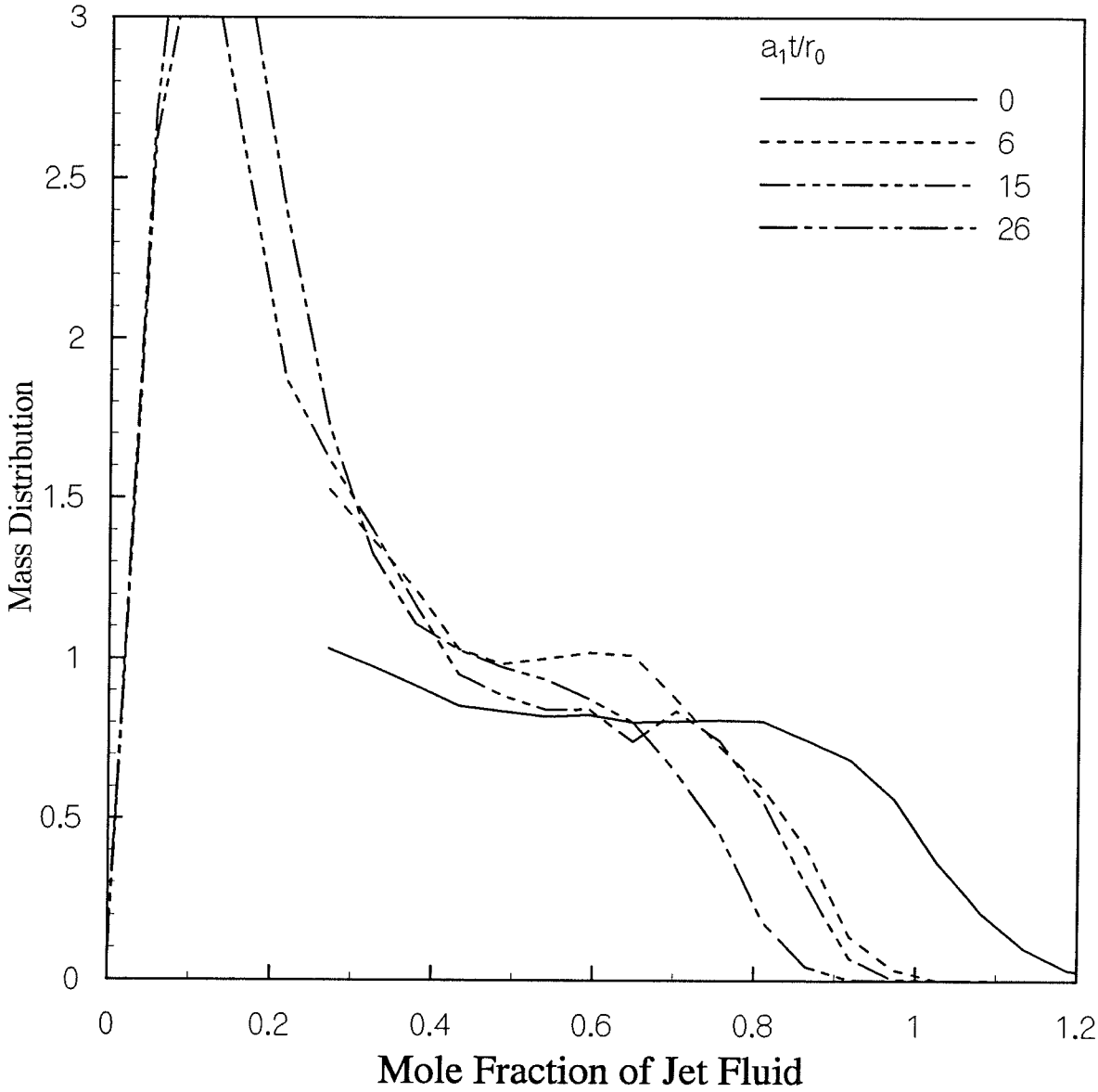

Figure 5-8. Mass Distribution Function for M = 1.50, a_1t/r_0 = 0, 6, 15, and 26.

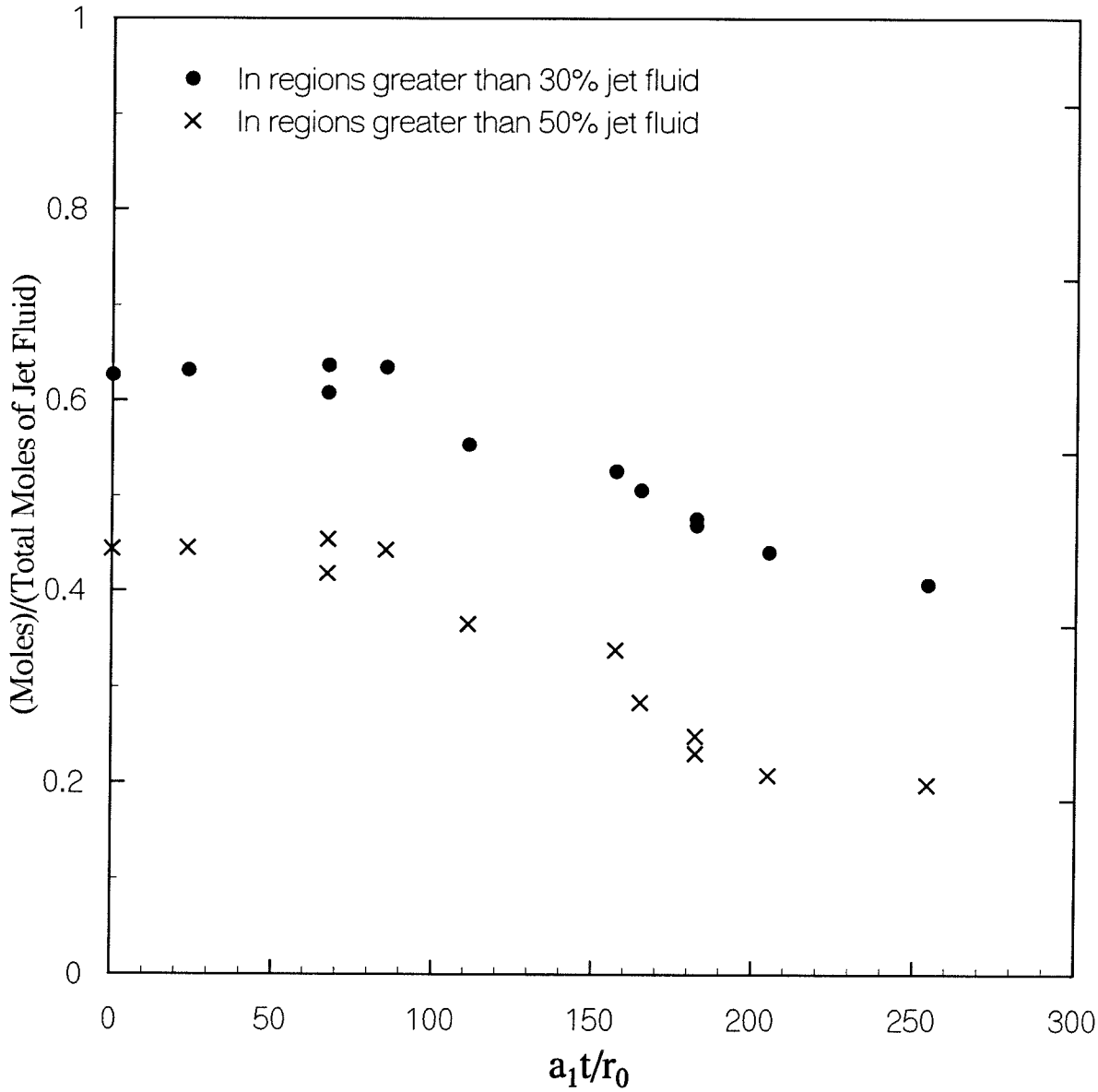

Figure 5-9. Mass of Jet Fluid in Regions at Greater than 30% and 50% Jet Fluid. M = 1.066.

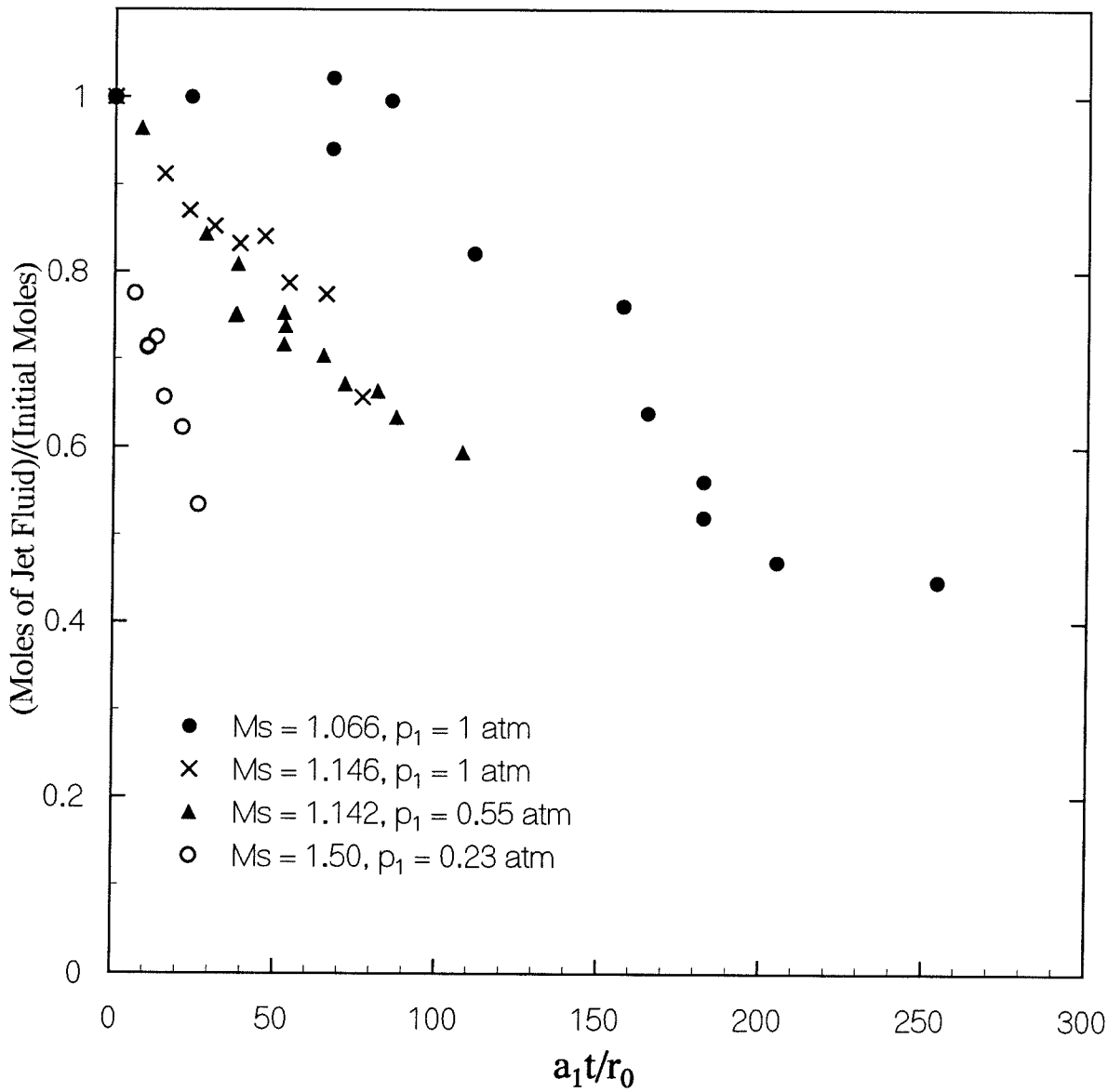

Figure 5-10. Mass of Jet Fluid in Regions Greater than 50% Jet Fluid vs. a_1t/r_0, M = 1.066, M = 1.142, M = 1.146, and M = 1.50.

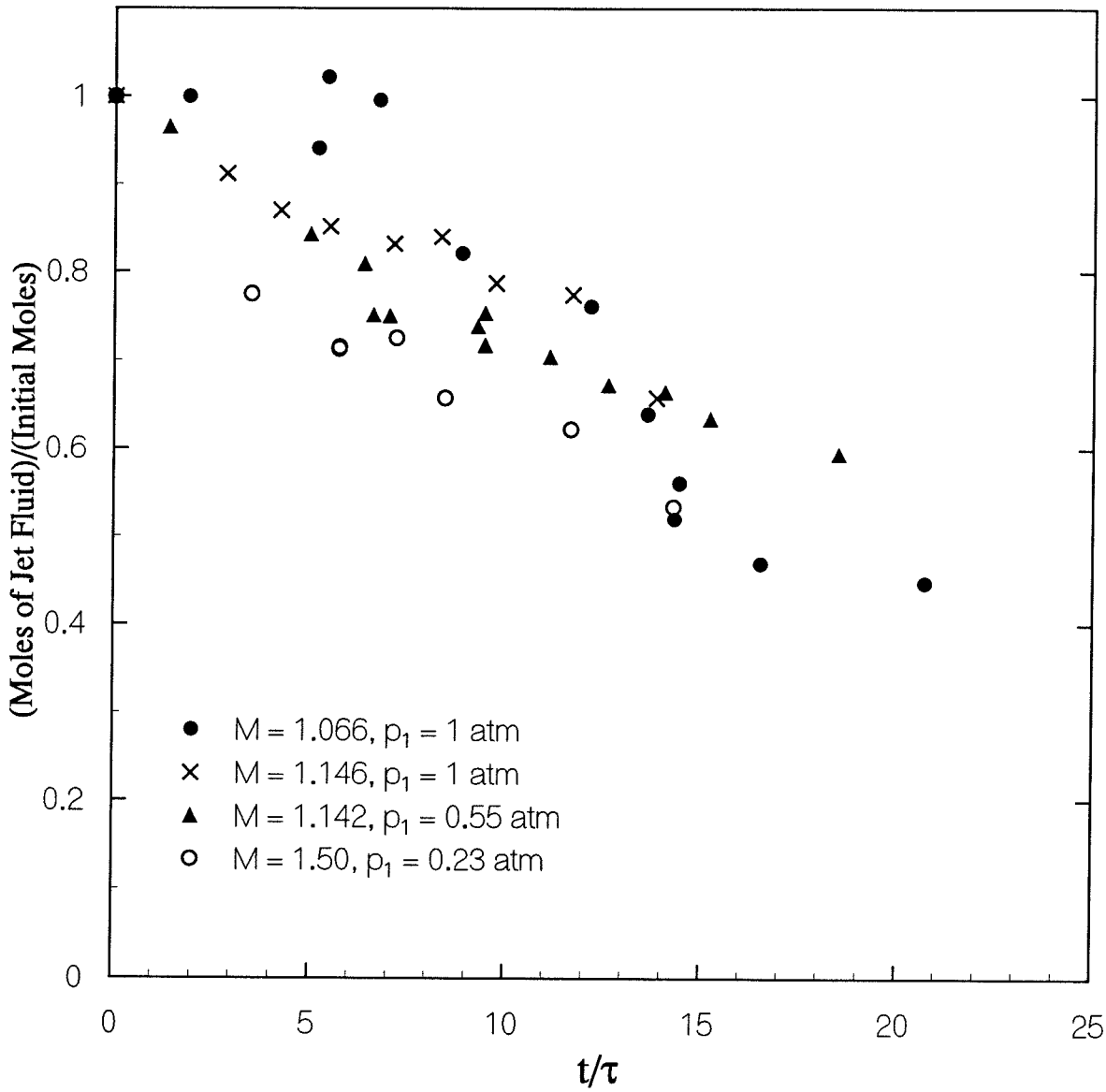

Figure 5-11. Mass of Jet Fluid in Regions Greater than 50% Jet Fluid. M = 1.066. M = 1.142. and M = 1.50.

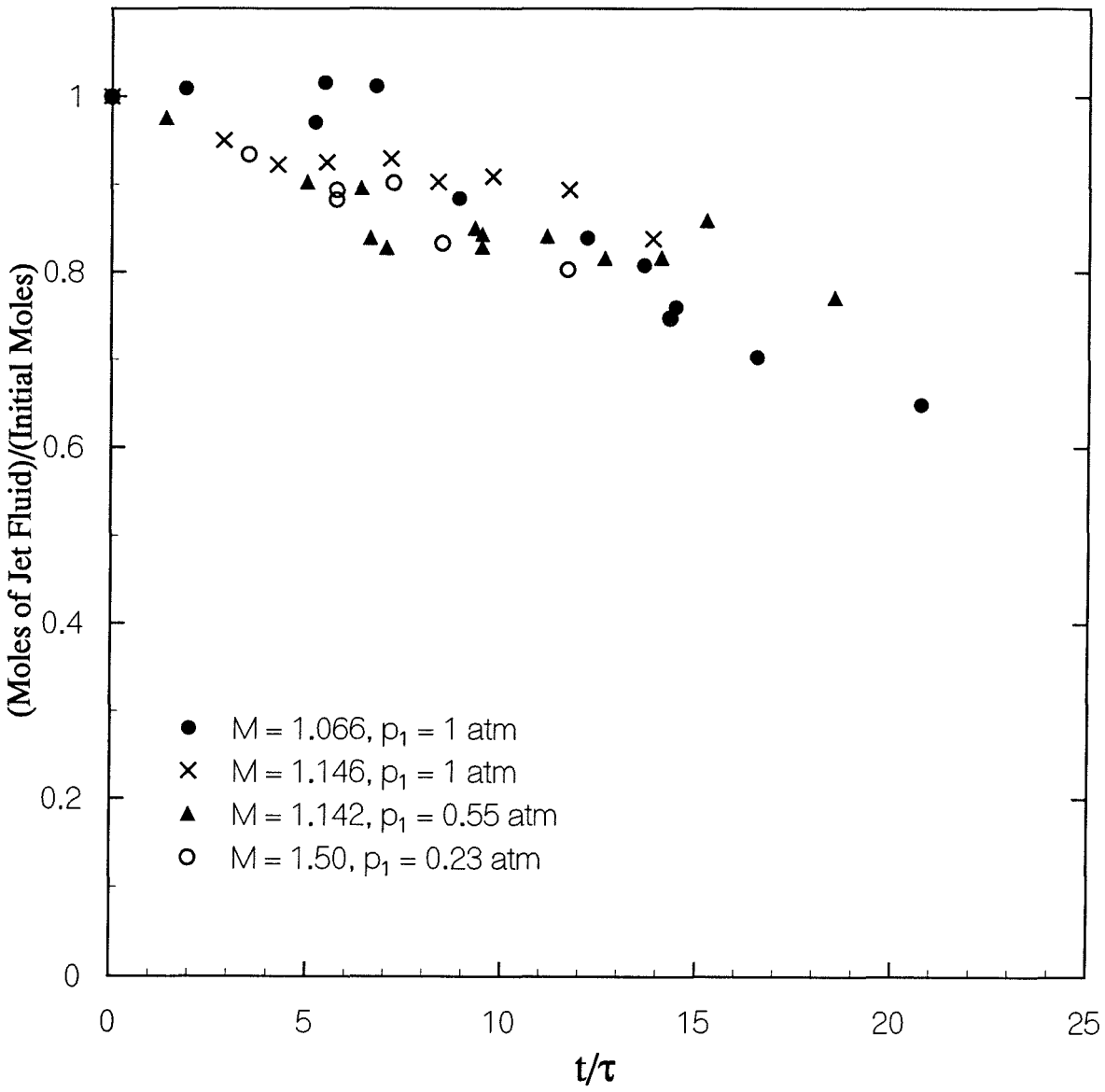

Figure 5-12. Mass of Jet Fluid in Regions Greater than 30% Jet Fluid. M = 1.066. M = 1.142. and M = 1.50.

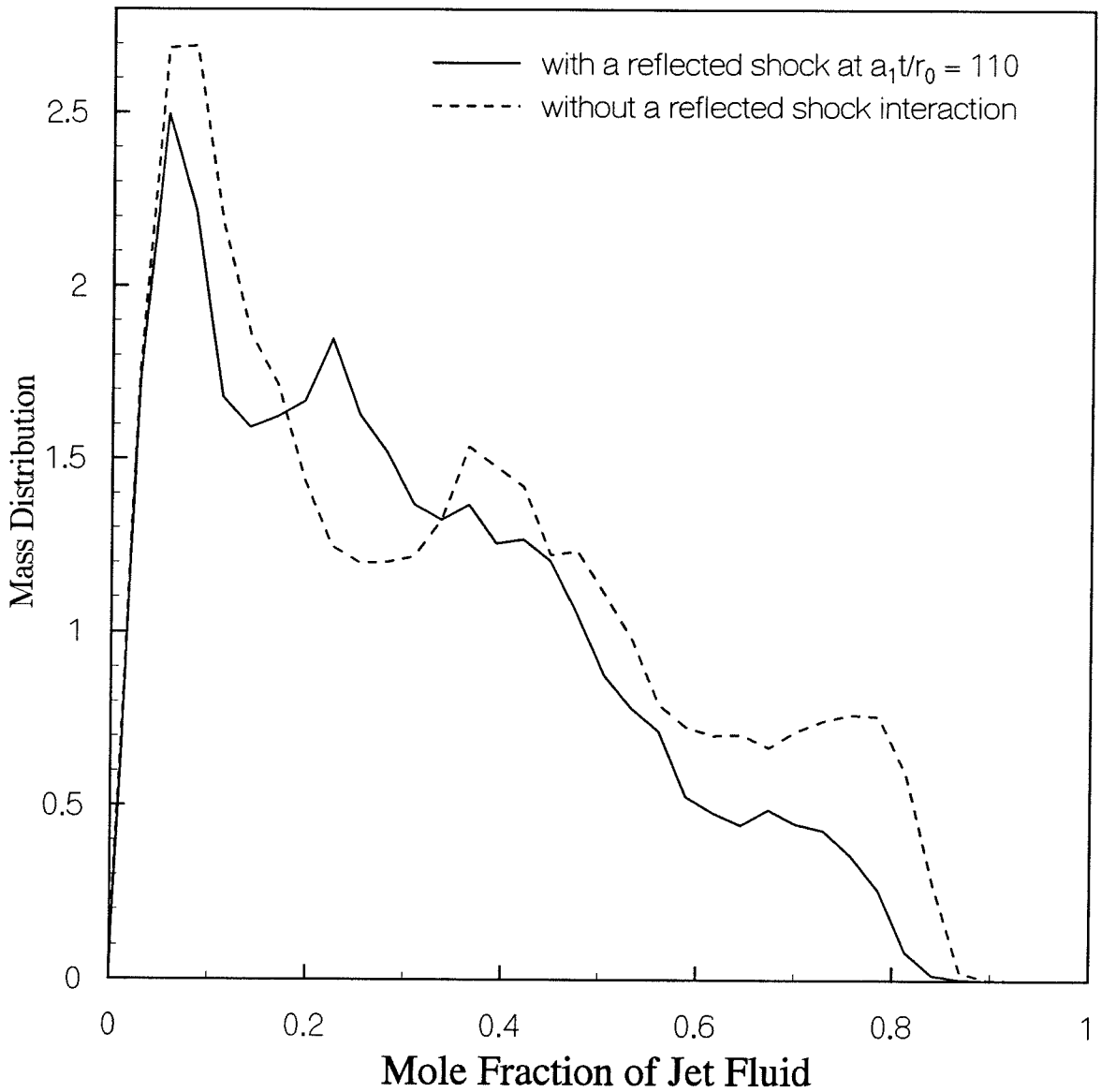

Figure 5-13. Mass Distribution Function for M = 1.066, a_1t/r_0 = 180, Without a Reflected Shock Interaction, and With a Reflected Shock Interaction at a_1t/r_0 = 110.

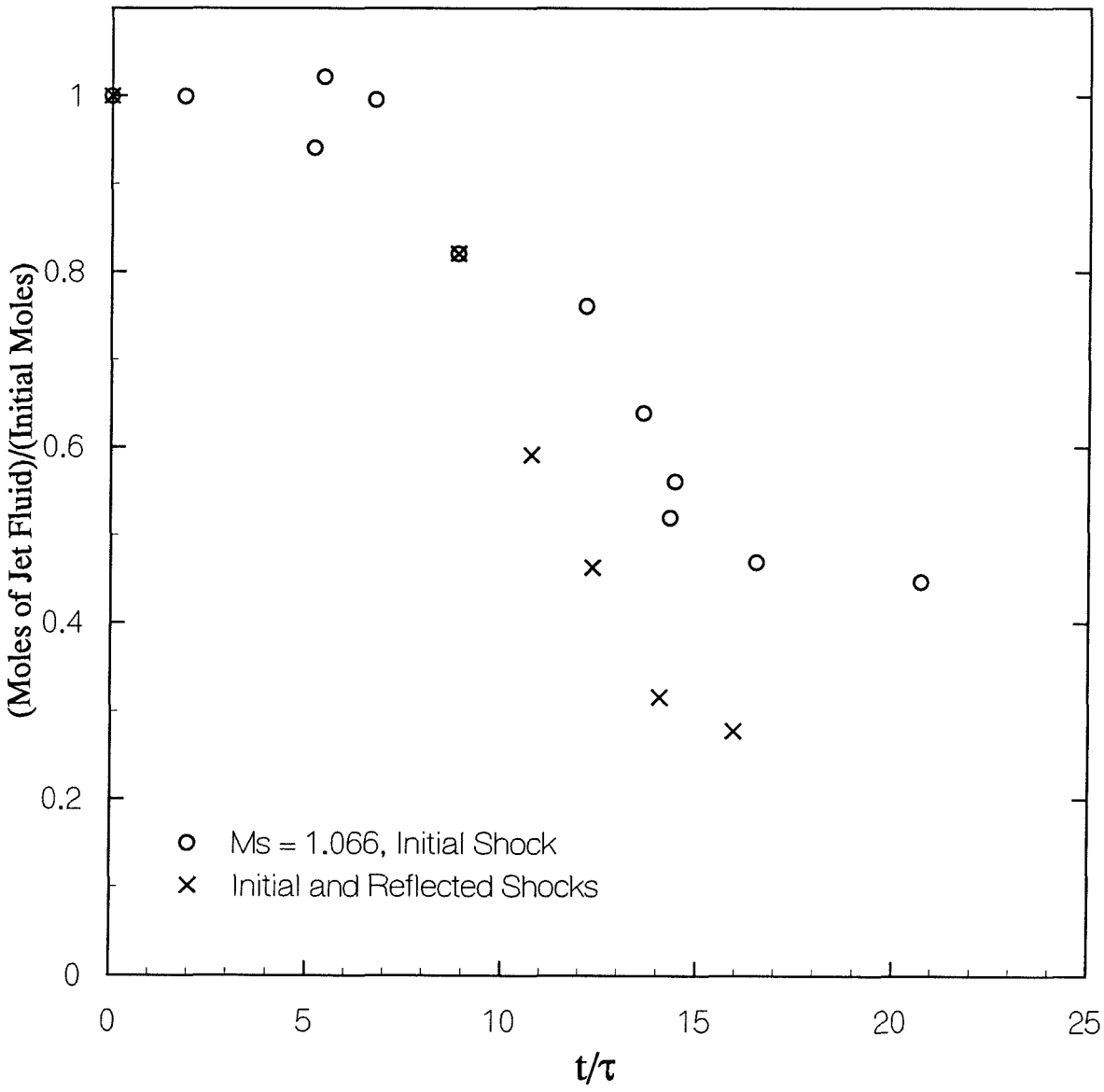

Figure 5-14. Mass of Jet Fluid in Regions Greater than 50% Jet Fluid, With and Without the Reflected Shock. M = 1.066 .

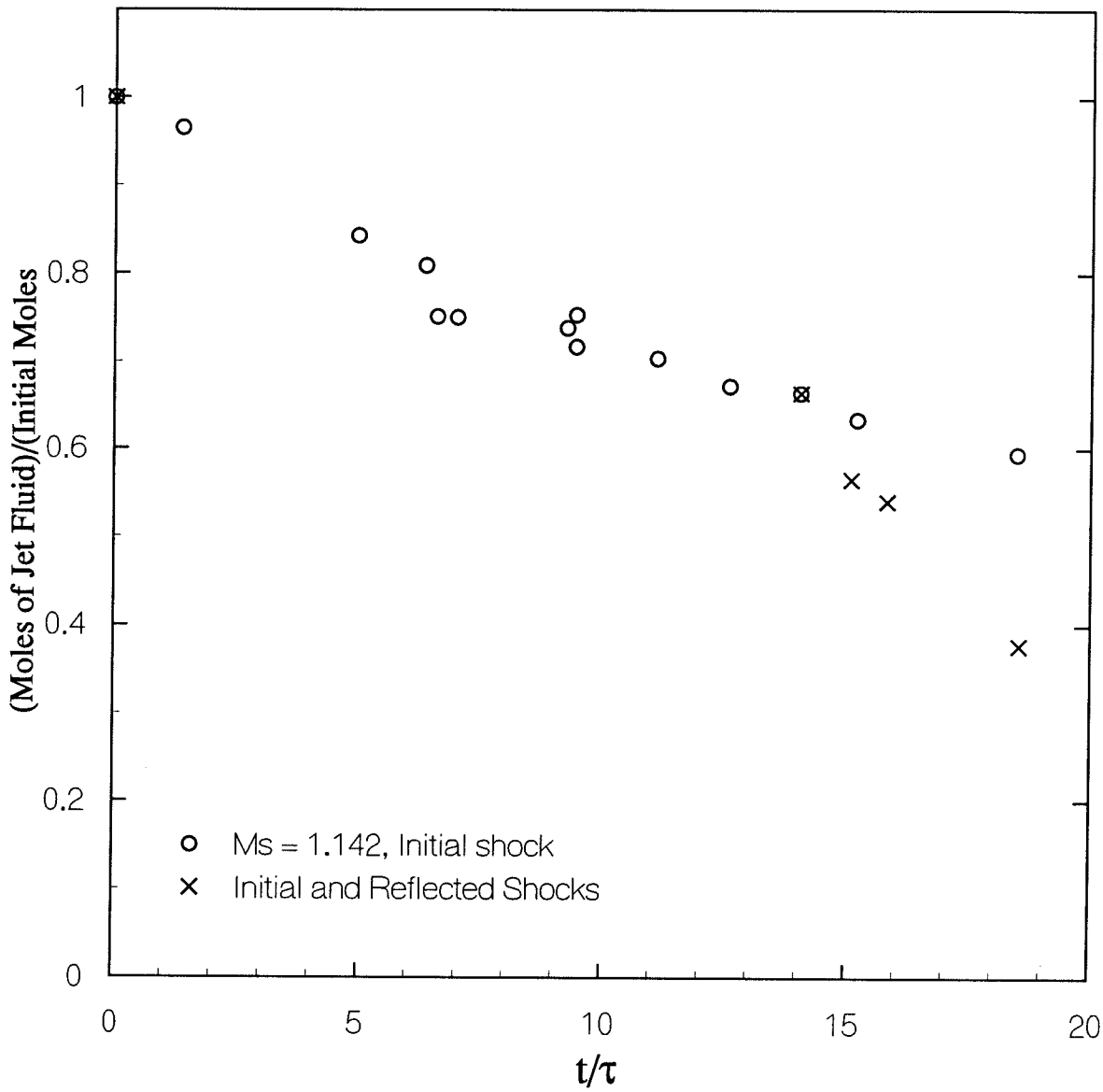

Figure 5-15. Mass of Jet Fluid in Regions Greater than 50% Jet Fluid, With and Without the Reflected Shock. M = 1.142 .

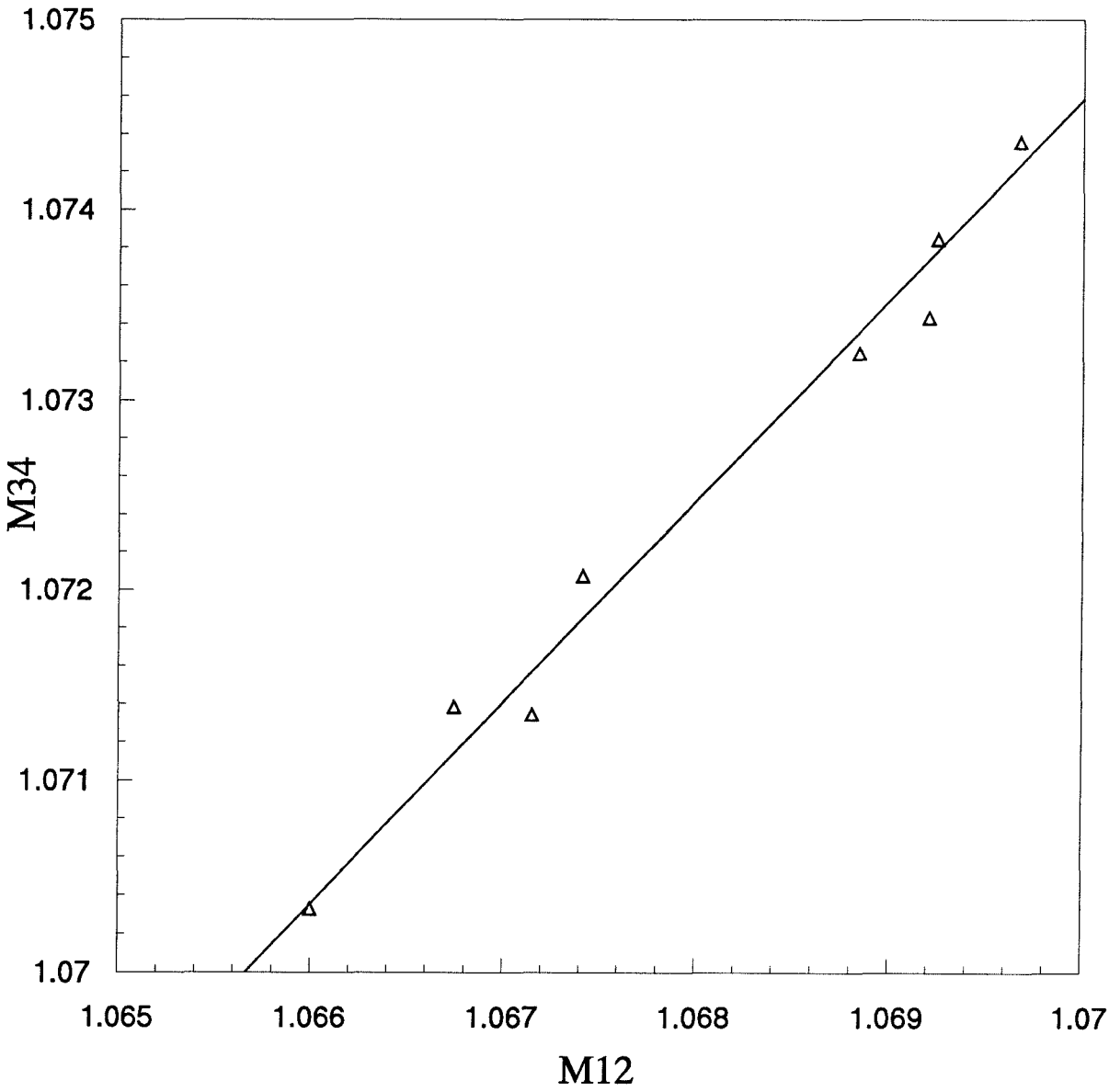

Figure B-1. Mach Number Between Transducers 3 and 4 vs. the Mach Number Between Transducers 1 and 2.

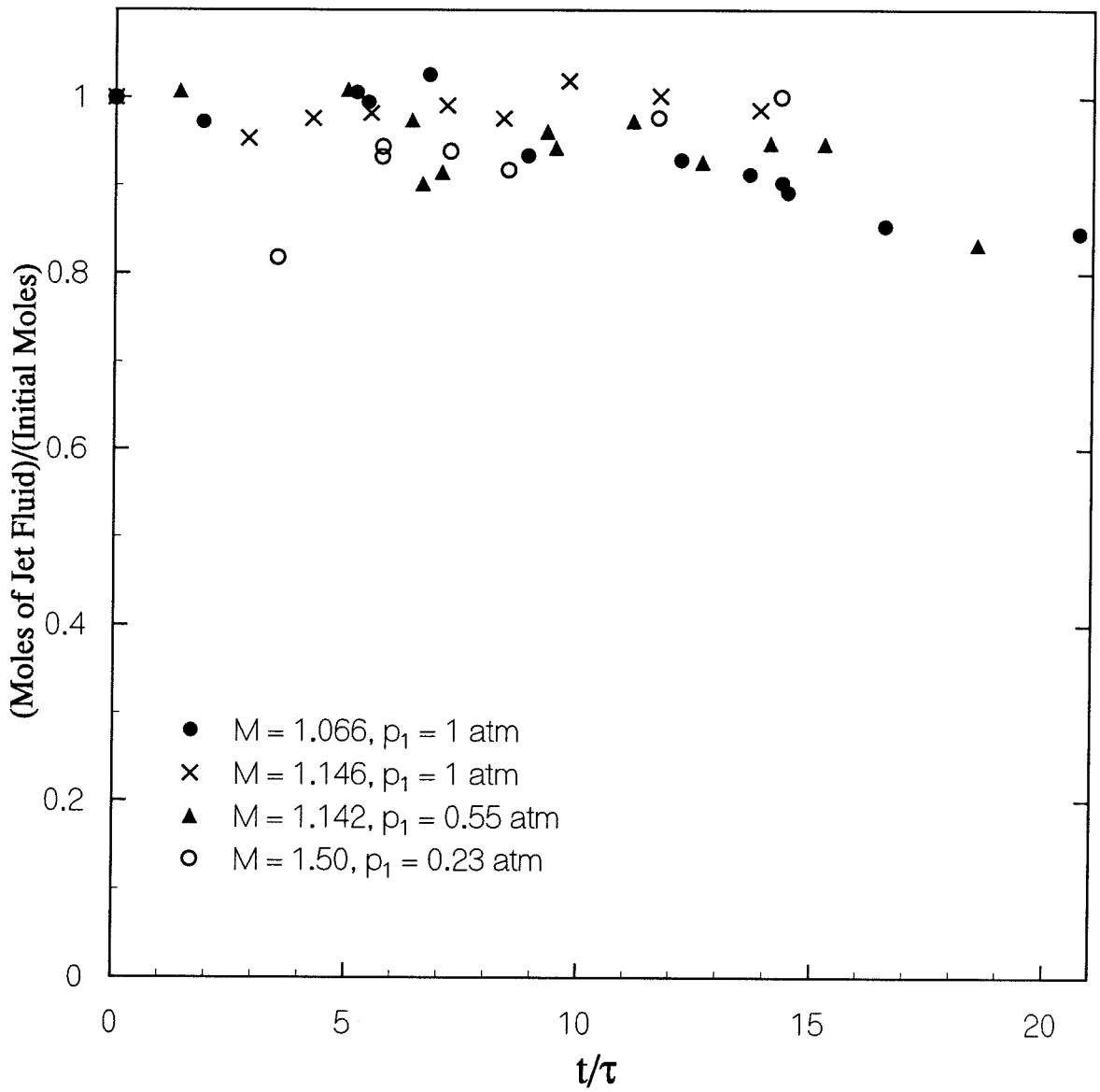

Figure E-1. Total Mass of Jet Fluid.

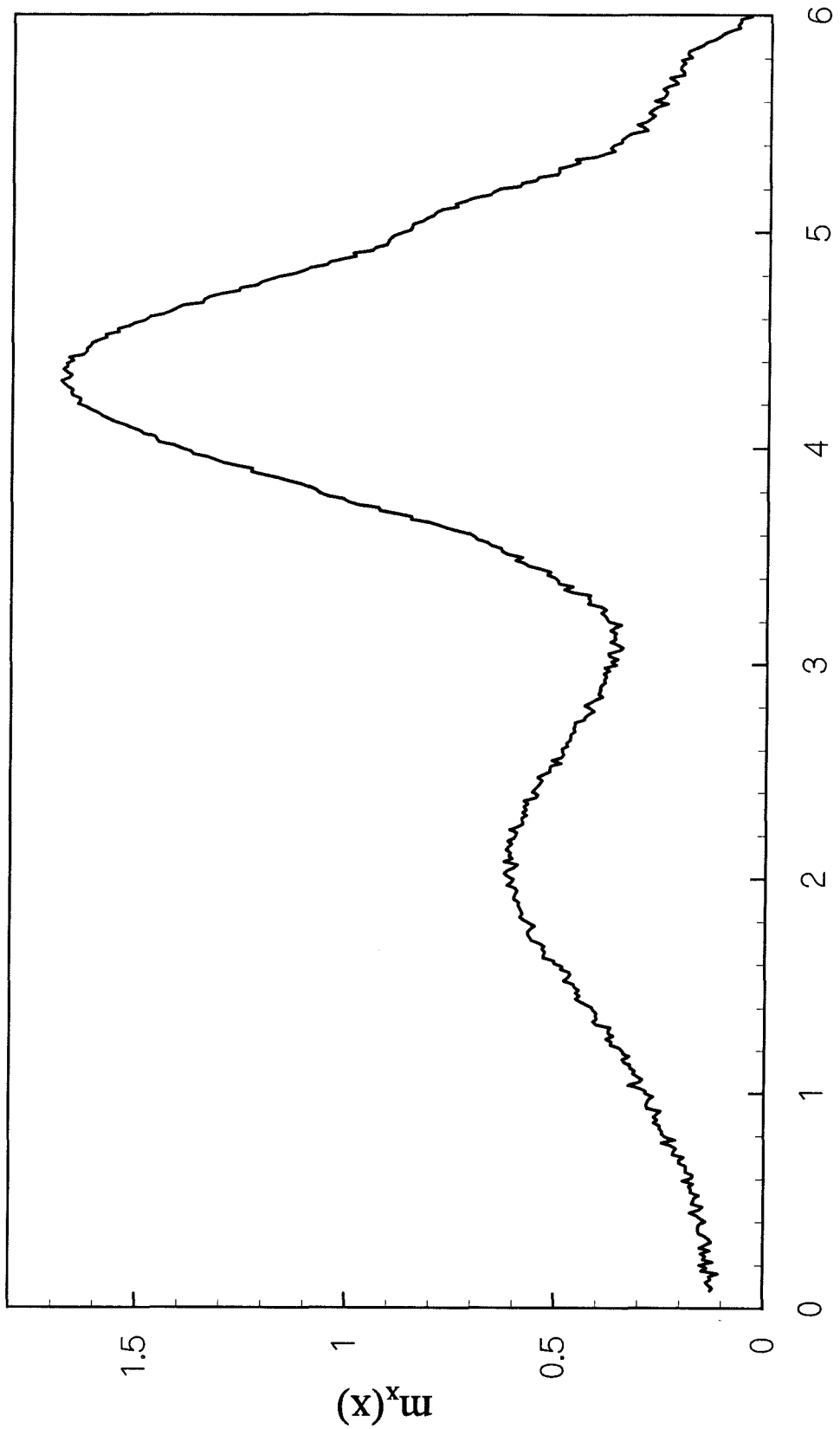

Figure E-2. Distribution of Mass Along the X Axis $t/\tau = 16.5$, $M = 1.066$.

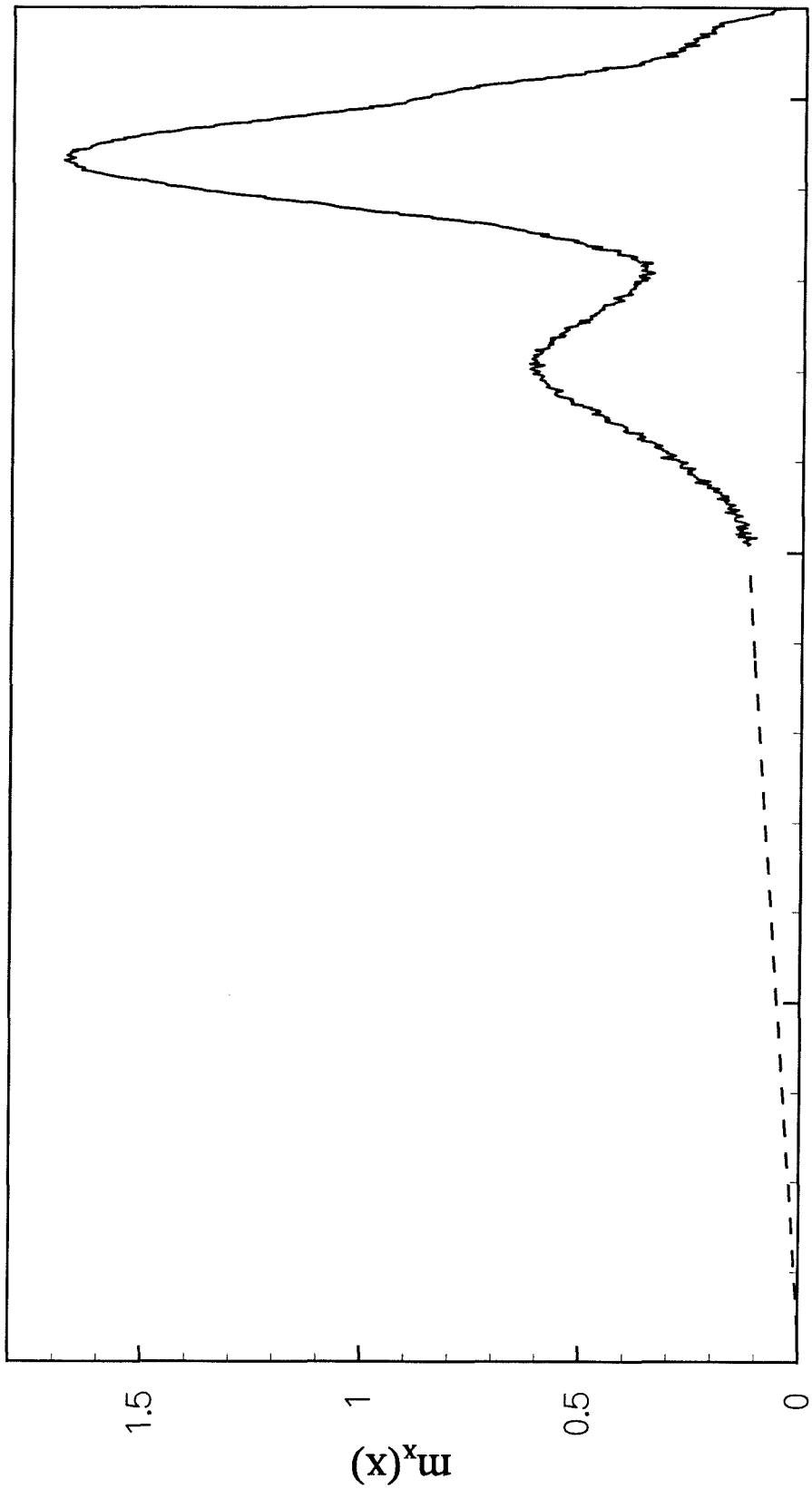

Figure E-3. Distribution of Mass Along the X Axis $t/\tau = 16.5$, M = 1.066 .

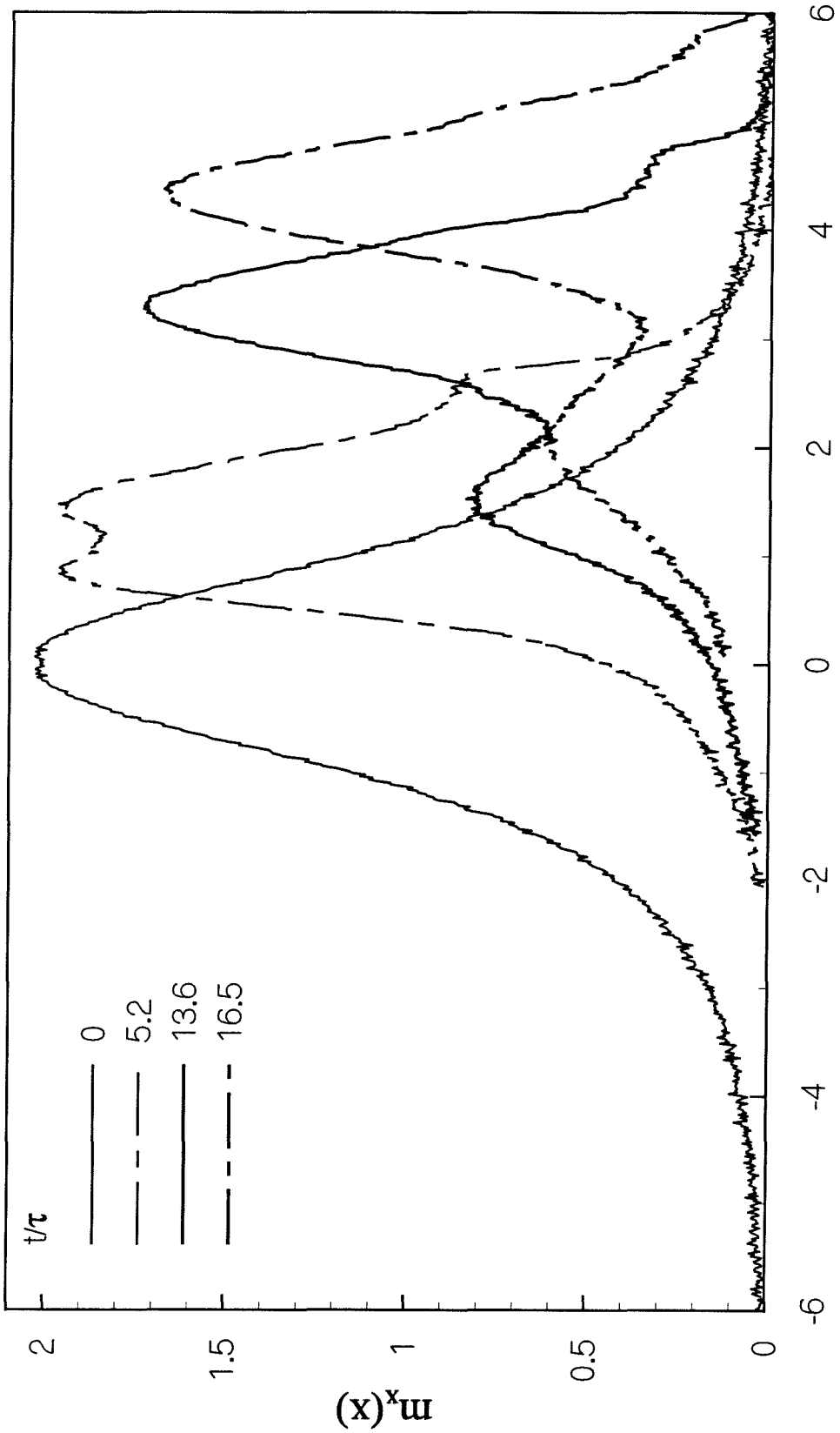

Figure E-4. Distribution of Mass Along the X Axis, M = 1.066 .